

EUROPEAN ORGANISATION FOR NUCLEAR RESEARCH (CERN)



Submitted to: JHEP

CERN-EP-2025-037
26th March 2025

Measurements of the production cross-sections of a Higgs boson in association with a vector boson and decaying into WW^* with the ATLAS detector at $\sqrt{s} = 13$ TeV

The ATLAS Collaboration

Measurements of the total and differential Higgs boson production cross-sections, via WH and ZH associated production using $H \rightarrow WW^* \rightarrow \ell\nu\ell\nu$ and $H \rightarrow WW^* \rightarrow \ell\nu jj$ decays, are presented. The analysis uses proton–proton events delivered by the Large Hadron Collider at a centre-of-mass energy of 13 TeV and recorded by the ATLAS detector between 2015 and 2018. The data correspond to an integrated luminosity of 140 fb^{-1} . The sum of the WH and ZH cross-sections times the $H \rightarrow WW^*$ branching fraction is measured to be $0.44^{+0.10}_{-0.09} \text{ (stat.) } ^{+0.06}_{-0.05} \text{ (syst.) pb}$, in agreement with the Standard Model prediction. Higgs boson production is further characterised through measurements of the differential cross-section as a function of the transverse momentum of the vector boson and in the framework of Simplified Template Cross-Sections.

Contents

1	Introduction	2
2	Analysis overview	3
3	ATLAS detector	6
4	Monte Carlo samples	7
5	Event reconstruction	9
6	Event selection	10
6.1	Opposite-sign 2ℓ channel	11
6.2	Same-sign 2ℓ channel	12
6.3	3ℓ channel	13
6.4	4ℓ channel	15
6.5	STXS categorisation	17
7	Background modelling	20
7.1	Backgrounds with non-prompt leptons	26
8	Systematic uncertainties	27
8.1	Experimental uncertainties	27
8.2	Theoretical uncertainties	28
9	Fit procedure and results	29
9.1	Fit procedure	29
9.2	Results	30
10	Conclusions	40
	Appendix	42
A	Input variables for multivariate discriminants	42
B	Additional plots for the STXS categorisation	44
C	Breakdown of uncertainties contributing to observed results	46

1 Introduction

Higgs boson production with a W or Z boson, respectively denoted by WH and ZH and collectively referred to as VH associated production, provides direct access to the Higgs boson couplings to weak bosons. In the case of VH associated production with a subsequent $H \rightarrow WW^*$ decay, the Higgs boson couples only to vector bosons at both the production and decay vertices, allowing these couplings to be precisely measured

and providing a stringent test of the Standard Model (SM) of particle physics. Statistically significant deviations from their expected values could indicate beyond the SM effects; for example, the presence of additional Higgs bosons [1, 2] or new heavy vector bosons [3, 4].

Measurements are presented of the total and differential WH and ZH production cross-sections in the $H \rightarrow WW^*$ decay channel, using proton–proton (pp) collisions at a centre-of-mass energy of $\sqrt{s} = 13$ TeV. The data correspond to an integrated luminosity of 140 fb^{-1} and were recorded by the ATLAS detector [5] at the Large Hadron Collider (LHC) [6] between 2015 and 2018. Previous measurements were performed by the ATLAS [7] and CMS [8] Collaborations at $\sqrt{s} = 7$ and 8 TeV and more recently by the CMS Collaboration [9] at $\sqrt{s} = 13$ TeV using 137 fb^{-1} of data. The latest result from the ATLAS Collaboration used data from 2015 and 2016 with an integrated luminosity of 36.1 fb^{-1} [10]. In the $H \rightarrow WW^*$ decay channel, measurements of Higgs boson production via gluon–gluon fusion (ggF) and vector-boson fusion (VBF) at $\sqrt{s} = 13$ TeV have also been performed by the ATLAS [11] and CMS [9] Collaborations, and VH production has been studied in other decay modes including $H \rightarrow ZZ^* \rightarrow 4\ell$ [12, 13], $H \rightarrow \gamma\gamma$ [14, 15], $H \rightarrow b\bar{b}$ [16, 17], and $H \rightarrow \tau\tau$ [18, 19].

The analysis is performed using events with two (2ℓ), three (3ℓ), or four (4ℓ) charged leptons (electrons or muons) in the final state, targeting the WH and ZH channels. In the 2ℓ channel, both opposite-sign (OS) and same-sign (SS) lepton pair configurations are considered. Leptonic decays of τ -leptons resulting from the decays of the associated W/Z bosons or the W bosons from the $H \rightarrow WW^*$ decay are considered as signal, while no specific selection is performed for events with hadronically decaying τ -leptons in the final state. Events from VH production with $H \rightarrow \tau\tau$ are considered as background. Additionally, events from ggF and VBF production are also considered as background.

In each channel, multivariate discriminants are used to maximise the sensitivity to the Higgs boson signal. The distributions of these discriminants are combined in a binned maximum-likelihood fit to extract the signal yield and the background normalisations. The maximum-likelihood fit provides results for the WH and the ZH channels separately and for their combination VH . The VH fit is performed assuming the SM prediction for the relative cross-sections of the WH and ZH production processes. Cross-section measurements are also performed in bins of the transverse momentum, p_T , of the associated vector boson, p_T^V , (defined as the “ p_T^V scheme” in the following) and in kinematic fiducial regions defined according to the Simplified Template Cross-Section (STXS) framework [20–22] (defined as the “STXS scheme” in the following).

The outline of the paper is as follows: Section 2 provides an overview of the signal characteristics and the analysis strategy and a description of the STXS framework, Section 3 describes the ATLAS detector, Section 4 describes the data and the simulated event samples, Section 5 describes the event reconstruction, Section 6 details the various selections used to define the signal regions in the analysis, Section 7 discusses how the backgrounds are estimated and includes the definitions of the control regions, and Section 8 provides commentary on the systematic uncertainties. Finally, Section 9 defines the likelihood fit procedure and presents the results of the analysis, which are summarised in Section 10.

2 Analysis overview

Higgs boson production with a W or Z boson, followed by a $H \rightarrow WW^*$ decay, is sought using events with two, three, or four charged leptons in the final state. The analysis is designed to select events

which are kinematically consistent with the WH and ZH , $H \rightarrow WW^*$ processes in order to enhance the signal-to-background ratio. The channels are defined as follows:

- (1) **Opposite-sign 2ℓ channel:** The targeted signal contribution consists of a VH process in which the associated weak boson V decays hadronically and produces two energetic jets, while W bosons from the $H \rightarrow WW^*$ decay produce two oppositely charged leptons and two neutrinos. The leading-order Feynman diagram for this process is shown in Figure 1(a). After requiring two leptons of different flavour, the leading backgrounds for this channel are $t\bar{t}$ and Wt processes. Other major components are $Z \rightarrow \tau\tau$ and WW production with two associated jets. Final states including W +jets and multijets may produce mis-identified leptons, contaminating the signal region. Other background sources include WZ production and other processes involving the Higgs boson, in particular its production through ggF ;
- (2) **Same-sign 2ℓ channel:** The targeted signal contribution consists of a WH process in which the associated W boson decays leptonically, while for the $H \rightarrow WW^*$ decay, the W boson with the same sign as the associated W boson decays leptonically and the other W boson decays hadronically. The final state therefore contains two leptons with the same charge, two neutrinos, and two energetic jets. The leading-order Feynman diagram for this process is shown in Figure 1(b). Significant backgrounds in this channel include WZ , $W+\gamma$, and W +jets production; WW , $Z+\gamma$, Z +jets, and top-quark processes also contribute to this final state;
- (3) **3ℓ channel:** The targeted signal contribution consists of a WH process where all weak bosons decay leptonically producing three charged leptons and three neutrinos in the final state. The leading-order Feynman diagram for this process is shown in Figure 1(c). The most prominent background to this channel is WZ production. Non-resonant WWW production is another significant background with the same final state as the signal. Other important backgrounds are ZZ , $Z+\gamma$, Z +jets, $t\bar{t}$, and Wt production;
- (4) **4ℓ channel:** The targeted signal contribution consists of a ZH process where all weak bosons decay leptonically producing four charged leptons and two neutrinos in the final state. The leading-order Feynman diagram for this process is shown in Figure 1(d). The main backgrounds to this channel are non-resonant ZZ and WWZ production.

The selections defining the channels described above are mutually exclusive due to the requirements on the respective multiplicity and total charge of the leptons. To maximise the analysis sensitivity to the VH , $H \rightarrow WW^*$ process in each of these event topologies, the data samples for each channel — except for the opposite-sign 2ℓ channel — are further subdivided into several signal regions (SRs). Additional kinematic regions, with orthogonal selection criteria and designated as control regions (CRs), are used to determine normalisation factors that are applied to the major backgrounds in each SR.

A multivariate analysis is performed in all analysis channels to increase the sensitivity. The most suitable type of multivariate analysis, its configuration, and the set of input variables are chosen for each channel. Specifically, the setup providing the best separation of signal from background is selected and less complex setups are preferred if they provide the same performance. The 2ℓ and 3ℓ channels use neural networks based on Keras [23] with the TensorFlow [24] backend, and the 4ℓ channel uses boosted decision trees (BDTs) in TMVA [25].

The final results are extracted from a fit that simultaneously considers all SRs and CRs. The final results consist of a set of parameters of interest (POIs) which scale the SM expectations for the signal yields or cross-sections to match the observed data. The 3ℓ and 4ℓ are the most sensitive channels for

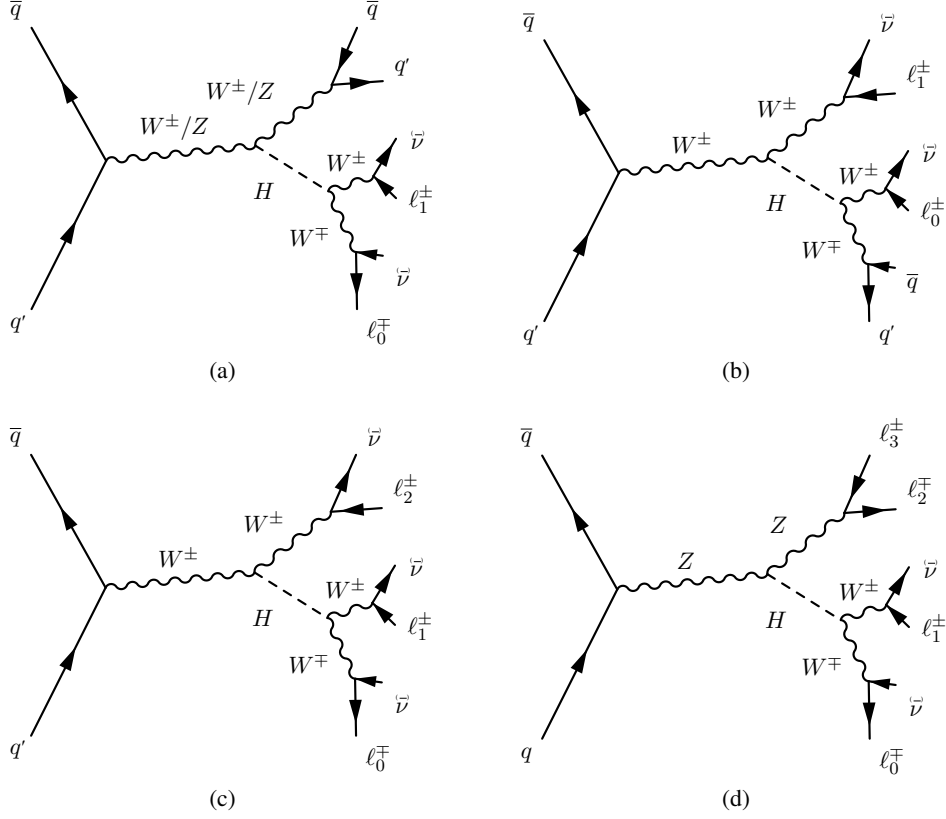


Figure 1: Leading-order Feynman diagrams for the signal topologies considered by the $VH, H \rightarrow WW^*$ measurement. The subscripts on the leptons are defined for the individual channels in Section 6: (a) the opposite-sign 2ℓ channel, (b) the same-sign 2ℓ channel, (c) the 3ℓ channel, and (d) the 4ℓ channel.

the measurements of WH and ZH production, respectively, and for the overall measurement of VH production.

Cross-section measurements of VH are also conducted using the Stage 1.2 scheme of the STXS framework [20–22], which splits the production modes of the Higgs boson into kinematic fiducial regions or “categories” which are theoretically relevant, experimentally accessible, and straightforward to statistically combine. In this framework, the VH STXS category assumes a leptonic decay of the V and is further categorised according to its transverse momentum, p_T^V ; in contrast, the $q\bar{q} \rightarrow V(\rightarrow q\bar{q})H$ (along with VBF) and $gg \rightarrow Z(\rightarrow q\bar{q})H$ (along with ggF) topologies are included in the electroweak (EW) qqH and ggH STXS categories, respectively. In the STXS measurement scheme, WH and ZH are measured independently in fiducial bins of p_T^V and $q\bar{q} \rightarrow V(\rightarrow q\bar{q})H$ is measured as part of EW qqH in a single fiducial bin of dijet invariant mass, m_{jj} . In addition, the limited interference between $q\bar{q} \rightarrow V(\rightarrow q\bar{q})H$ and VBF in the phase space relevant for this analysis motivates the use of the p_T^V measurement scheme, which is inclusive in the decay of the V . In the p_T^V scheme, the sensitivity to low values of p_T^V is primarily enabled by the $V(\rightarrow \text{leptons})H$ measurements, while the sensitivity to high values of p_T^V is primarily enabled by the $V(\rightarrow q\bar{q})H$ measurements. In both schemes, fiducial bins are merged to provide sensitivity for all measured parameters. This leads to measuring four bins of VH in the p_T^V scheme and three bins for each of WH and ZH as well as one bin for EW qqH in the STXS scheme.

3 ATLAS detector

The ATLAS detector [5] at the LHC covers nearly the entire solid angle around the collision point.¹ It consists of an inner tracking detector surrounded by a thin superconducting solenoid, electromagnetic and hadron calorimeters, and a muon spectrometer incorporating three large superconducting air-core toroidal magnets.

The inner-detector system (ID) is immersed in a 2 T axial magnetic field and provides charged-particle tracking in the range of $|\eta| < 2.5$. The high-granularity silicon pixel detector covers the vertex region and typically provides four measurements per track, the first hit normally being in the insertable B-layer (IBL) [26, 27]. It is followed by the silicon microstrip tracker (SCT), which usually provides eight measurements per track. These silicon detectors are complemented by the transition radiation tracker (TRT), which enables radially extended track reconstruction up to $|\eta| = 2.0$. The TRT also provides electron identification information based on the fraction of hits (typically 30 in total) above a higher energy-deposit threshold corresponding to transition radiation.

The calorimeter system covers the pseudorapidity range $|\eta| < 4.9$. In the region $|\eta| < 3.2$, electromagnetic calorimetry (EM) is provided by barrel and endcap high-granularity lead/liquid-argon (LAr) calorimeters, with an additional thin LAr presampler covering $|\eta| < 1.8$ to correct for energy loss in material upstream of the calorimeters. Hadron calorimetry is provided by the steel/scintillator-tile calorimeter, segmented into three barrel structures within $|\eta| = 1.7$, and two copper/LAr hadron endcap calorimeters. The solid angle coverage is completed with forward copper/LAr and tungsten/LAr calorimeter modules optimised for electromagnetic and hadronic energy measurements respectively.

The muon spectrometer (MS) comprises separate trigger and high-precision tracking chambers measuring the deflection of muons in a magnetic field generated by the superconducting air-core toroidal magnets. The field integral of the toroids ranges between 2.0 and 6.0 T m across most of the detector. Three layers of precision chambers, each consisting of layers of monitored drift tubes, covers the region $|\eta| < 2.7$, complemented by cathode-strip chambers in the forward region, where the background is highest. The muon trigger system covers the range $|\eta| < 2.4$ with resistive-plate chambers in the barrel, and thin-gap chambers in the endcap regions.

Events of interest are selected by the first-level trigger system implemented in custom hardware, followed by selections made by algorithms implemented in software in the high-level trigger [28]. The first-level trigger accepts events from the 40 MHz bunch crossings at a rate below 100 kHz, which the high-level trigger reduces further to record events to disk at about 1 kHz. The full ATLAS Run 2 data sample is used for the analysis, consisting of pp collision data produced at $\sqrt{s} = 13$ TeV and recorded between 2015 and 2018. The data are subjected to quality requirements [29], including the removal of events recorded when relevant detector components were not operating correctly. The total integrated luminosity after this cleaning of the data corresponds to 140 fb^{-1} [30].

An extensive software suite [31] is used in the reconstruction and analysis of real and simulated data, in detector operations, and in the trigger and data acquisition systems of the experiment.

¹ ATLAS uses a right-handed coordinate system with its origin at the nominal interaction point (IP) in the centre of the detector and the z -axis along the beam pipe. The x -axis points from the IP to the centre of the LHC ring, and the y -axis points upwards. Cylindrical coordinates (r, ϕ) are used in the transverse plane, ϕ being the azimuthal angle around the z -axis. The pseudorapidity is defined in terms of the polar angle θ as $\eta = -\ln \tan(\theta/2)$. Angular distance is measured in units of $\Delta R \equiv \sqrt{(\Delta\eta)^2 + (\Delta\phi)^2}$.

4 Monte Carlo samples

Monte Carlo (MC) generators are used to model the hard pp scattering matrix element (ME), parton shower (PS) and hadronisation, and underlying event (UE). The generators that are used for modelling signal and background processes are listed in Table 1.

The Higgs boson samples are simulated with the $H \rightarrow WW^*$ decay in the four main production channels: ggF, VBF, VH , and associated production with a top quark pair ($t\bar{t}H$). These samples are simulated using a Higgs boson mass of 125 GeV and then normalised to the cross-sections [21] computed for a mass of 125.09 GeV [32]. The normalisation of all Higgs boson samples accounts for the decay branching ratio calculated with HDECAY [33–35] and PROPHECY4F [36–38]. All samples use the PDF4LHC15 [39] parton distribution function (PDF) set and are interfaced to PYTHIA 8.2 [40] for parton showering and hadronisation, with parameters set according to the AZNLO [41] (for VH , ggF, and VBF) or A14 [42] (for $t\bar{t}H$) set of tuned parameters (tunes). The decays of bottom and charm hadrons are performed using EVTGEN [43].

The WH and ZH events are simulated at next-to-leading order (NLO) in perturbative quantum chromodynamics (QCD) for up to one additional jet using POWHEG BOX v2 MINLO [44–48]. Each sample is normalised to a cross-section calculated at next-to-next-to-leading-order (NNLO) in QCD and at NLO in EW [49–53]. The subdominant $gg \rightarrow ZH$ process is simulated at leading-order (LO) in QCD with POWHEG BOX v2 and normalised to a cross-section calculated at NLO in QCD with next-to-leading logarithmic (NLL) corrections [54, 55].

The ggF events are simulated using POWHEG BOX v2 NNLOPS [56]. The simulation achieves NNLO accuracy for arbitrary inclusive $gg \rightarrow H$ observables by reweighting the Higgs boson rapidity spectrum in HJ-MINLO [57–59] to that of HNNLO [60]. The sample is normalised to a cross-section computed at next-to-next-to-next-to-leading-order (N³LO) in QCD with NLO EW corrections [21, 61–70]. The VBF events are simulated using POWHEG BOX v2 and normalised to a cross-section calculated at NLO in QCD and EW [71, 72], with approximate NNLO in QCD corrections applied [73]. The $t\bar{t}H$ events are simulated using POWHEG BOX v2 [74, 75] at NLO accuracy in QCD. The sample is normalised to a cross-section computed at NLO accuracy in QCD with NLO EW corrections [21].

The main background processes include single boson, diboson, triboson, single top quark, and top quark pair production.

The Z/γ^* (“Z+jets”) processes are simulated using SHERPA 2.2.1 [76] at NLO in QCD for up to two jets and at LO for up to four jets, calculated using the COMIX [77] and OPENLOOPS [78–80] libraries. The single boson samples are normalised to cross-sections computed at NNLO in QCD [81]. The VV and $V+\gamma$ processes are simulated using SHERPA 2.2.2 and SHERPA 2.2.8, respectively, at NLO in QCD for up to one jet and at LO for up to three jets. Throughout the paper, WZ and ZZ are assumed to correspond to $WZ/W\gamma^*$ and $ZZ/Z\gamma^*$, respectively (i.e., including the virtual photon contribution). The on-shell VVV processes are modelled by SHERPA 2.2.2 at NLO in QCD inclusively and at LO for up to two jets. Virtual QCD corrections to the VV , $V+\gamma$, and VVV processes were provided by the OPENLOOPS library [78–80, 82]. The gg -initiated diboson processes are modelled by SHERPA 2.2.2 at LO in QCD for up to one jet and normalised to cross-sections computed at NLO in QCD [83, 84]. For all SHERPA samples, the events are simulated using the NNPDF3.0_{NNLO} [85] PDF set, and the matrix elements are matched with the SHERPA parton shower [77, 86] using the MEPS@NLO prescription [87–90] and the set of tuned parameters developed by the SHERPA authors. EW WW production in association with two jets ($WWqq$) is simulated using MADGRAPH5_AMC@NLO [91] with LO-accurate matrix elements [83] and using the NNPDF3.0_{NLO} [85]

PDF set. The events are interfaced to PYTHIA 8 for parton showering and hadronisation, with parameters set according to the A14 tune.

The top quark pair production is modelled by POWHEG Box v2 at NLO in QCD with the h_{damp} parameter² set to $1.5 \times m_{\text{top}}$ [92]. The events are normalised to a cross-section computed at NNLO in QCD with next-to-next-to-leading logarithmic (NNLL) corrections [93–99]. The Wt process is simulated using POWHEG Box v2 [100] at NLO in QCD using the five-flavour scheme. The diagram removal scheme [101] is used to remove interference and overlap with $t\bar{t}$ production. The $t\bar{t}V$, tZ , and tWZ processes are simulated using MADGRAPH5_AMC@NLO at NLO in QCD. For all top processes, events are simulated using the NNPDF3.0NLO PDF set. EVTGEN is used to model decays of hadrons containing b - or c -quarks, and the events are interfaced to PYTHIA 8 for parton showering and hadronisation, with parameters set according to the A14 tune.

All samples are processed through the GEANT4-based [102] ATLAS detector simulation [103] and the standard ATLAS reconstruction software [104]. The effect of pile-up is modelled by overlaying the hard-scattering event with simulated inelastic pp events simulated with PYTHIA 8.1 [105] using the NNPDF2.3LO [106] PDF set and the A3 [107] tune.

Table 1: MC generators used to model the signal and background processes. Alternative generators or parton shower models — used to estimate systematic uncertainties — are shown in parenthesis. In the last column, the prediction order (in QCD, unless specified otherwise) for the total cross-section is shown.

Process	ME (alternative)	PS/UE (alternative)	Prediction order for total cross-section
$q\bar{q} \rightarrow WH$	POWHEG Box v2 M1NLO	PYTHIA 8 (HERWIG 7 [108, 109])	NNLO QCD + NLO EW [49–53]
$q\bar{q} \rightarrow ZH$	POWHEG Box v2 M1NLO	PYTHIA 8 (HERWIG 7)	NNLO QCD + NLO EW [49–53]
$gg \rightarrow ZH$	POWHEG Box v2	PYTHIA 8 (HERWIG 7)	NLO + NLL [54, 55]
$ggF H$	POWHEG Box v2 NNLOPS	PYTHIA 8	N ³ LO QCD + NLO EW [21, 61–70]
$VBF H$	POWHEG Box v2	PYTHIA 8	NNLO QCD + NLO EW [71–73]
$t\bar{t}H$	POWHEG Box v2	PYTHIA 8	NLO QCD + NLO EW [21]
Z/γ^*	SHERPA 2.2.1 (MADGRAPH5_AMC@NLO)	SHERPA 2.2.1 (PYTHIA 8)	NNLO [81]
$q\bar{q}/g \rightarrow WW$	SHERPA 2.2.2	SHERPA 2.2.2	NLO [78–80]
$WZ/ZZ/V\gamma^*$	SHERPA 2.2.2	SHERPA 2.2.2	NLO [110]
$V+\gamma$	SHERPA 2.2.8	SHERPA 2.2.8	NLO [110]
$gg \rightarrow WW/ZZ$	SHERPA 2.2.2	SHERPA 2.2.2	NLO [83, 84]
VVV	SHERPA 2.2.2 (MADGRAPH5_AMC@NLO)	SHERPA 2.2.2 (PYTHIA 8)	NLO [111]
$qq \rightarrow WWqq$	MADGRAPH5_AMC@NLO	PYTHIA 8	LO
$t\bar{t}$	POWHEG Box v2 (MADGRAPH5_AMC@NLO)	PYTHIA 8 (HERWIG 7)	NNLO + NNLL [93–99]
Wt	POWHEG Box v2	PYTHIA 8	NLO [112, 113]
$t\bar{t}V$	MADGRAPH5_AMC@NLO	PYTHIA 8	NLO [114]
tZ	MADGRAPH5_AMC@NLO	PYTHIA 8	NLO [115]
tWZ	MADGRAPH5_AMC@NLO	PYTHIA 8	NLO [116]

² The h_{damp} parameter is a resummation damping factor and one of the parameters that controls the matching of POWHEG matrix elements to the parton shower and thus effectively regulates the high- p_T radiation against which the $t\bar{t}$ system recoils.

5 Event reconstruction

Candidate signal events are selected using triggers that require a single isolated lepton with minimum p_T thresholds ranging from 24 to 26 GeV for electrons and from 20 to 26 GeV for muons [117, 118], depending on the data-taking period. At least one of the leptons reconstructed offline is required to have triggered the event. Additionally, the lepton is required to have a reconstructed p_T higher than the nominal trigger threshold by at least 1 GeV, which ensures that the p_T is squarely on the plateau of the trigger’s efficiency.

Selected events are required to have at least one primary vertex reconstructed from at least two matched tracks, each with transverse momentum $p_T > 500$ MeV, as described in Ref. [119]. If an event has more than one reconstructed primary vertex, the vertex with the largest track $\sum p_T^2$ is selected for the analysis.

Electrons are reconstructed by matching energy clusters in the electromagnetic calorimeter to well-reconstructed tracks that are extrapolated to the calorimeter [120]. Electron candidates are required to satisfy $|\eta| < 2.47$, excluding the transition region $1.37 < |\eta| < 1.52$ between the barrel and end caps of the LAr calorimeter.

Muons are reconstructed from a global fit to matching tracks from the ID and the MS [121]. They are required to satisfy $|\eta| < 2.5$.

For the purpose of lepton counting, all leptons with $p_T > 10$ GeV and passing a set of identification requirements common to all channels are included. This ensures orthogonality between the channels when divided according to an exact lepton multiplicity and total charge.

To suppress particles mis-identified as leptons, several identification, impact parameter, and isolation criteria are applied to electron and muon candidates, shown in Table 2. For electrons, a likelihood-based identification method [122] is employed. Electron candidates in the 2ℓ and 3ℓ channels must satisfy the “Tight” likelihood working point, while electron candidates in the 4ℓ channel must satisfy the “Medium” likelihood working point. For muons, a cut-based identification method [121] is employed. Muon candidates must satisfy the “Medium” working point. The impact parameter requirements are $|z_0 \sin \theta| < 0.5$ mm and $|d_0|/\sigma_{d_0} < 5$ (3) for electrons (muons).³ Electron candidates must also be unambiguously reconstructed as electrons; they cannot be simultaneously reconstructed as photons.

For 2ℓ and 3ℓ channels, a newly developed multivariate method based on a BDT, the prompt lepton improved veto (PLIV), is employed. PLIV exploits isolation and lifetime information — including the presence of secondary vertices — associated with a track jet matched to the selected lepton candidate. It leads to a substantial improvement in the rejection of mis-identified leptons compared to previously available methods within ATLAS while maintaining high efficiency for selecting prompt leptons. Lepton candidates in the 2ℓ and 3ℓ channels must satisfy the “PLImprovedTight” working point, while electron and muon candidates in the 4ℓ channel must satisfy the cut-based “FCLoose” and “Loose_VarRad” working points, respectively, which rely on tracking and calorimeter isolation variables [120]. To suppress electron charge mis-identification in the same-sign 2ℓ channel and the 3ℓ channel with zero same-flavour, opposite-sign lepton pairs in the final state, another BDT discriminant (“ECIDS”) [122] is used.

³ The transverse impact parameter, d_0 , is defined by the point of closest approach of the track to the beamline in the r - ϕ plane, its uncertainty being σ_{d_0} , while the longitudinal impact parameter, z_0 , is given by the longitudinal distance to the hard-scatter vertex from this same point.

Table 2: The electron and muon definitions used by the analysis. Any selection in brackets, (...), is specific to the 4ℓ channel and is used instead of the preceding selection on that same line of the table; otherwise, the selections are applicable to all channels. *ECIDS is only applied to the same-sign 2ℓ channel and the 3ℓ channel with zero same-flavour, opposite-sign lepton pairs in the final state.

Criteria	Flavour	
	Electrons	Muons
p_T [GeV]	> 10	
$ \eta $	< 1.37 or $\in [1.52, 2.47]$	< 2.5
Identification	Tight (Medium)	Medium
$ z_0 \sin \theta $ [mm]	< 0.5	
$ d_0/\sigma_{d_0} $	< 5	< 3
Unambiguous e/γ	Yes	–
Isolation	PLImprovedTight (FCLoose)	PLImprovedTight (Loose_VarRad)
ECIDS	Yes* (No)	–

Jets are reconstructed using the anti- k_t algorithm with a radius parameter of $R = 0.4$ and particle-flow objects as input [123–125]. The four-momentum of the jets is corrected for the response of the non-compensating calorimeter, signal losses due to noise threshold effects, energy loss in inactive material, and contamination from pile-up (defined as additional pp interactions in the same and neighbouring bunch crossings) [126]. For jets entering the analysis, a kinematic selection of $p_T > 20$ GeV and $|\eta| < 4.5$ is applied. For the purpose of jet counting, only jets with $p_T > 30$ GeV are considered. A jet-vertex-tagger multivariate discriminant selection that reduces contamination from pile-up [127] is applied to jets with $20 < p_T < 60$ GeV and $|\eta| < 2.4$, utilising calorimeter and tracking information to separate hard-scatter jets from pile-up jets. Furthermore, to suppress pile-up jets in the forward region, $|\eta| > 2.5$, jet shapes and topological correlations in pile-up interactions are exploited [128, 129].

Jets with $p_T > 20$ GeV and $|\eta| < 2.5$ containing b -hadrons (b -jets) are identified using a neural-network discriminant, DL1r, based on a number of lower-level taggers which utilise relevant quantities such as the associated track impact parameters and information from secondary vertices. The working point that is adopted has an average 85% b -jet tagging efficiency, as estimated from simulated $t\bar{t}$ events [130, 131].

The missing transverse momentum \vec{p}_T^{miss} , with magnitude E_T^{miss} , is calculated as the negative vector sum of the p_T of all the selected leptons and jets, together with reconstructed tracks that are not associated with these objects but are consistent with originating from the primary vertex [132]. It serves as experimental proxy for the momentum carried by undetected particles. An object-based E_T^{miss} significance [132], $\mathcal{S}_{\text{miss}}$, is used to reject events where the E_T^{miss} arises due to the mis-reconstruction of the physics objects entering the calculation.

6 Event selection

In this section, the criteria used to define the SR in each channel are described. Table 3 summarises the selections for each channel before applying multivariate techniques. In Table 3 and throughout this section, the minimum lepton p_T selections are smaller than the p_T thresholds of the single lepton triggers. While

at least one lepton must have triggered the event and therefore satisfy one of these higher thresholds, all leptons must satisfy minimum p_T selections.

Table 3: Definition of the event selection for each SR in the analysis before applying multivariate techniques. The selections are defined and motivated for all channels in their respective subsections of Section 6. “SFOS” and “DFOS” refer to same- and different-flavour, opposite-sign lepton pairs, respectively. In the context of the 4ℓ channel, leptons 0 and 1, ℓ_0 and ℓ_1 , comprise the Higgs boson candidate — this is described in greater detail in Section 6.4.

Channel	2ℓ		3ℓ		4ℓ	
	OS	SS	Z-dominated	Z-depleted	1-SFOS	2-SFOS
Minimum lepton p_T [GeV]	15	15	15	15	10	10
Number of leptons	2	2	3	3	4	4
Total lepton charge	0	± 2	± 1	± 1	0	0
Number of SFOS pairs	0	–	1 or 2	0	1	2
Number of DFOS pairs	1	–	–	–	–	–
Minimum $\Delta R_{\ell\ell}$	0.1	0.4	0.1	0.1	0.2 ($\ell_0\ell_1$)	
Minimum $m_{\ell\ell}$ [GeV]	10	–	12 (all SFOS)	–	12 (all SFOS) or 10 (all DFOS)	
Number of jets	≥ 2	≥ 1	–	–	–	–
Number of b -tagged jets	0	0	0	0	0	0
$ m_{\ell\ell} - m_Z $ [GeV]	–	> 20 ($e^\pm e^\pm$)	> 25 (all SFOS)	–	–	–
$m_{\ell\ell}$ [GeV]	–	–	–	–	–	< 50 ($\ell_0\ell_1$)
E_T^{miss} [GeV]	–	–	> 30	–	–	–
$ m_{jj} - 85 \text{ GeV} $ [GeV]	< 15	–	–	–	–	–
m_{jj} [GeV]	–	< 500	–	–	–	–
Δy_{jj}	< 1.2	–	–	–	–	–
$ m_{4\ell} - 122.5 \text{ GeV} $ [GeV]	–	–	–	–	–	> 7.5
$\text{ANN}_{\text{DFOS}}^{iVH}$	> 0.2	–	–	–	–	–
$\text{ANN}_{\text{Zdep}}^{iVH}$	–	–	–	< 0.25	–	–

6.1 Opposite-sign 2ℓ channel

The opposite-sign 2ℓ channel requires two different-flavour, opposite-sign (DFOS) leptons from the decay of the Higgs boson, labelled ℓ_0 and ℓ_1 in decreasing order of p_T , and two or more jets from the decay of the associated vector boson, which can be either a W or a Z . The leading and subleading leptons must exceed p_T thresholds of 22 GeV and 15 GeV, respectively, and are required to satisfy the common lepton selections. The invariant mass of the leptons must satisfy $m_{\ell\ell} > 10$ GeV to remove low-mass resonances, and the angular separation between the leptons must satisfy $\Delta R_{\ell\ell} > 0.1$ to remove overlapping leptons. To reject top quark production, events with at least one b -jet are vetoed. To ensure orthogonality with the ATLAS ggF and VBF production measurements [11], the leading dijet system is required to have an invariant mass of $|m_{jj} - 85 \text{ GeV}| < 15$ GeV and a rapidity separation of $\Delta y_{jj} < 1.2$.

An artificial neural network (ANN) is trained to simultaneously classify VH , ggF, VBF, top, Z +jets, and WW processes; ggF and VBF correspond to the dominant Higgs boson backgrounds, and top, Z +jets, and WW correspond to the dominant non-Higgs boson backgrounds. The output consists of six distinct output nodes, $\text{ANN}_{\text{DFOS}}^i$, each describing the likeliness of the input event to stem from process i ($i = VH, \text{ggF}, \text{VBF}, \text{top}, Z\text{-jets}, \text{and } WW$) with the condition that $\sum_i \text{ANN}_{\text{DFOS}}^i = 1$. Different nodes are needed to build dedicated control regions to normalise the relevant background processes, as explained in Section 7. In total, 19 variables are used as input — these are summarised in Table 14 of Appendix A. To construct the

SR, the VH output node of the ANN is required to be greater than 0.2, corresponding to a signal efficiency of 80% and a background rejection of 77%.

Figure 2 shows distributions of $\text{ANN}_{\text{DFOS}}^{VH}$ and a signal-sensitive kinematic variable in the opposite-sign 2ℓ SR, as obtained from the fit procedure described in Section 9.1 (hereafter called a “post-fit” distribution).

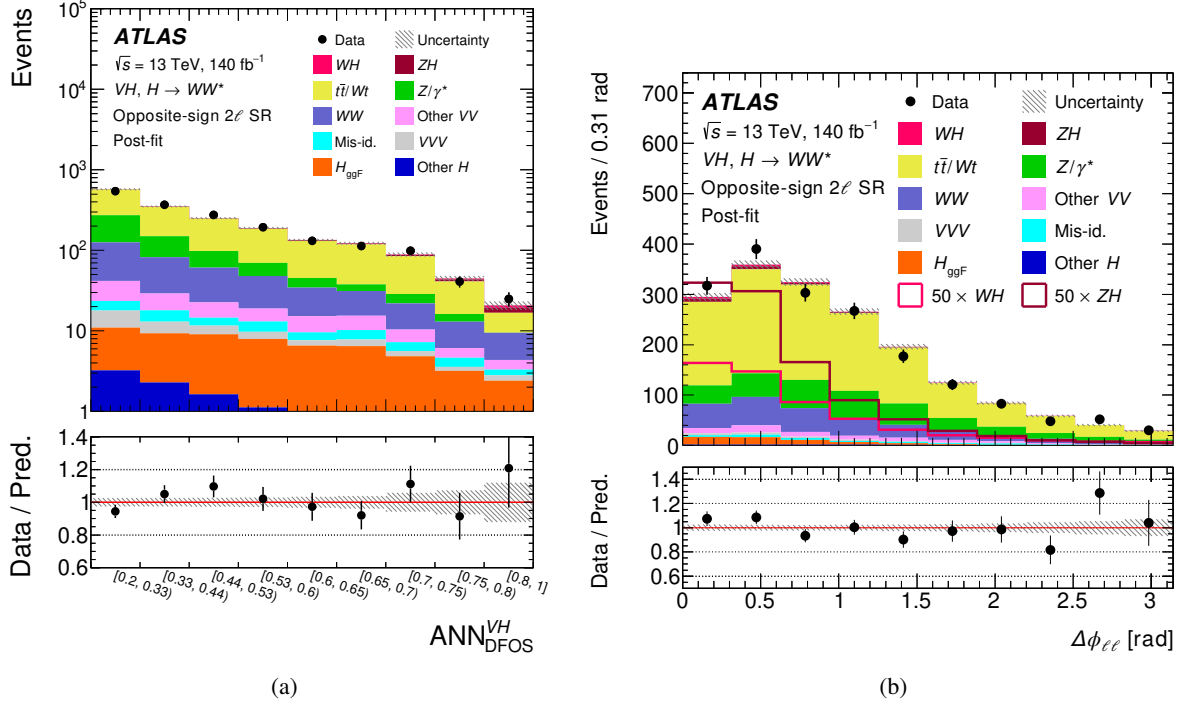


Figure 2: Post-fit distribution of (a) $\text{ANN}_{\text{DFOS}}^{VH}$ and (b) the dilepton azimuthal separation, $\Delta\phi_{\ell\ell}$, in the opposite-sign 2ℓ SR. In (b), the post-fit WH and ZH signal yields are overlaid. The lower panel shows the ratio of the data to the sum of the fitted signal and background. The hatched band shows the total uncertainty. The post-fit results are obtained from the combined 2-POI fit described in Section 9.1. In all subsequent post-fit distributions, “Mis-id.” is the mis-identified lepton background, as described in Section 7.1.

6.2 Same-sign 2ℓ channel

The same-sign 2ℓ channel selects exactly two same-sign isolated leptons with the leading lepton p_T above 22 GeV and subleading lepton p_T above 15 GeV. The leading and subleading leptons are labelled as ℓ_0 and ℓ_1 , respectively. Events with at least one reconstructed jet are selected to maintain a high signal efficiency; the choice to require at least one jet instead of at least two jets is made because a significant fraction of simulated signal events, 57%, have only one reconstructed jet. The invariant mass of the leading dijet system, m_{jj} , is required to be below 500 GeV for events with two or more jets to suppress contributions from the same-sign WW process [133]. Events containing any b -tagged jets are vetoed to reject the top backgrounds. The angular separation between the leptons is required to be $\Delta R_{\ell\ell} > 0.4$ to suppress the $W+\gamma$ events. The events are further split into $\text{SS}2\mu$, $\text{SS}2e$, and SSDF channels according to the lepton flavour. The $\text{SS}2e$ channel requires two electrons and vetoes events where the invariant mass of the electron pair is within ± 20 GeV of the Z pole — this suppresses Z +jets events, where the charge of an electron

is reconstructed incorrectly. The $\text{SS}2\mu$ channel requires two muons, and the SSDF channel requires one electron and one muon. The selections described above constitute the $\text{SS}2\mu$, $\text{SS}2e$, and SSDF SRs.

The WZ process is the dominant background in the same-sign 2ℓ channel. A recurrent neural network (RNN) [134] is trained to distinguish WH from WZ , and the same RNN is used in each of the $\text{SS}2\mu$, $\text{SS}2e$, and SSDF SRs. The RNN has the advantage of being able to learn sequential dependencies for arbitrary-length sequences of objects as input. This feature is used in the analysis where the number of jet variables depend on the jet multiplicity of the events.

The sequences provided to the RNN consist of reconstructed objects placed in order of leptons, E_T^{miss} , and jets (up to a maximum of five jets) with leptons and jets further ordered by p_T . The RNN uses the p_T , η , and ϕ of leptons and jets and the magnitude, E_T^{miss} , and the azimuthal angle, ϕ_{miss} , of the missing transverse momentum. A variable containing the information to distinguish between different particle types (leptons, missing transverse momentum, and jets) is also given as input to the RNN. The geometry of the ATLAS detector — and the physics — has a rotational symmetry in the ϕ direction and a mirror symmetry in the η direction. These symmetries are used to pre-process the input variables: the coordinate system of the sequence is rotated to keep the leading lepton with a ϕ coordinate of 0 and reflected to keep the leading lepton with a positive η coordinate. By doing so, the training data is used in a more efficient way as the RNN does not need to learn these symmetries in the training process.

Figure 3 shows the post-fit distributions of the RNN discriminants and signal-sensitive kinematic variables in the three same-sign 2ℓ SRs. In the $\text{SS}2\mu$ signal region, an RNN shape mis-modelling in WZ events, the largest background in that signal region, was observed. A correction to the RNN shape was evaluated using a validation region enriched in the WZ background and applied to each of the $\text{SS}2\mu$, $\text{SS}2e$, and SSDF signal regions. A detailed description of this correction is given in Section 7.

6.3 3ℓ channel

In the 3ℓ channel, exactly three isolated leptons with $p_T > 15$ GeV are required with a total charge of ± 1 . The lepton with unique charge is labelled ℓ_0 , the lepton closest to ℓ_0 in angular distance ΔR is labelled ℓ_1 , and the remaining lepton is labelled ℓ_2 . This labelling scheme is demonstrated pictorially in the leading-order Feynman diagram, Figure 1(c). In signal events, leptons ℓ_0 and ℓ_1 are most likely to originate from the $H \rightarrow WW^*$ decay with probabilities of 99% and 85%, respectively.

The most prominent background processes in the 3ℓ channel are WZ production and top quark processes with either three prompt leptons (e.g., $t\bar{t}V$) or two prompt leptons and one non-prompt lepton from a b -hadron decay (e.g., $t\bar{t}$).

The analysis of the 3ℓ channel separates events with at least one same-flavour, opposite-sign charge (SFOS) lepton pair from events with zero SFOS lepton pairs, which have different signal-to-background ratios. Due to the presence of background processes with $Z \rightarrow \ell\ell$ decays as a dominant background, the former set of events is hereafter referred to as the Z -dominated channel, while the latter is referred to as the Z -depleted channel.

In the Z -dominated channel, the major background processes are those involving Z bosons. Therefore, the invariant mass, $m_{\ell\ell}$, for each SFOS pair is required to satisfy a Z -veto selection: $|m_{\ell\ell} - m_Z| > 25$ GeV. To suppress background events from heavy-flavour quarkonia, the minimum invariant mass of all SFOS pairs is required to be greater than 12 GeV. Furthermore, the E_T^{miss} is required to be larger than 30 GeV to select final states with neutrinos. To suppress processes containing top quarks, events with at least one

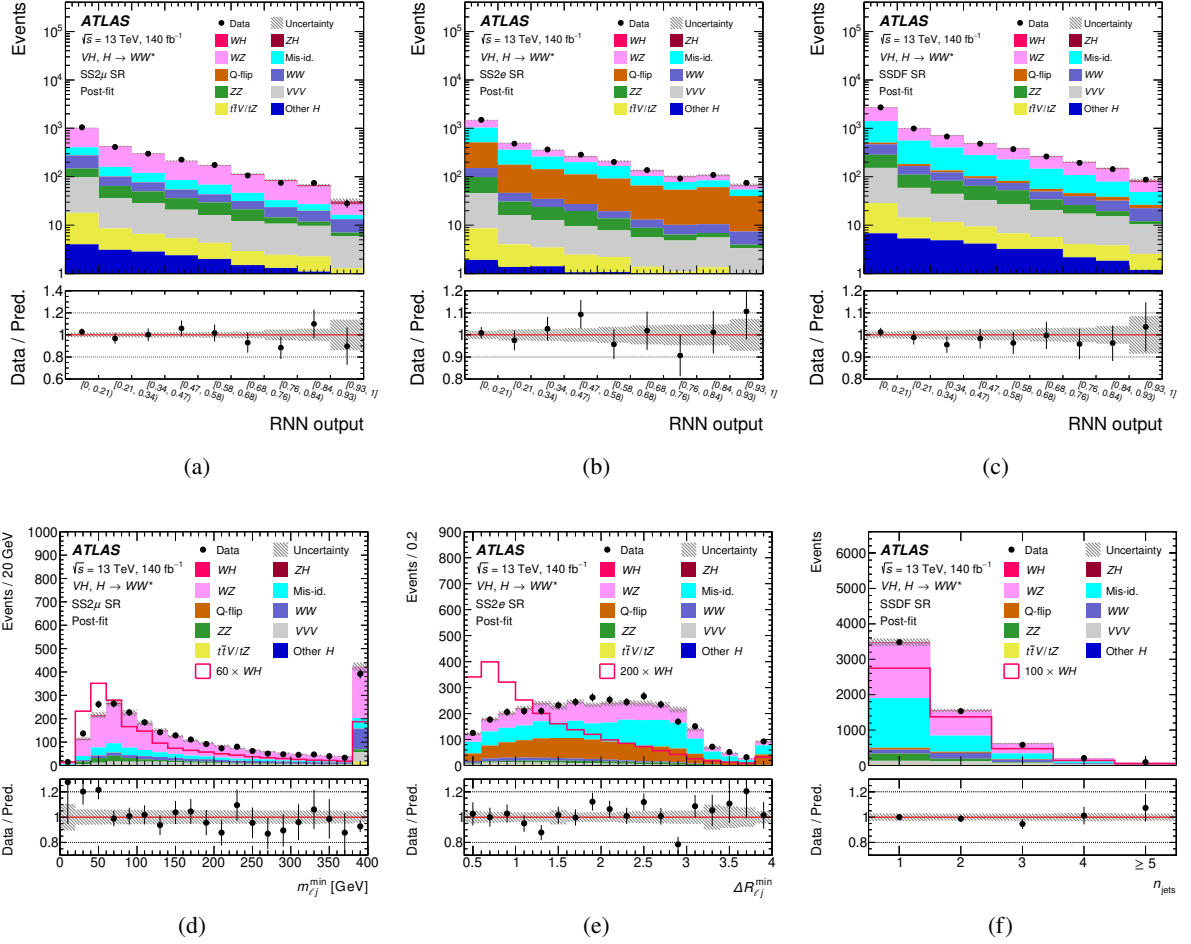


Figure 3: Post-fit distributions of the RNN discriminant in (a) SS2 μ , (b) SS2e, and (c) SSDF SRs and (d) the minimum lepton-jet invariant mass for each lepton in the SS2 μ SR, (e) the ΔR between each lepton and the nearest jet in the SS2e SR, and (f) the number of jets in the SSDF SR. In (d), (e), (f), the post-fit WH signal yield is overlaid. The lower panel shows the ratio of the data to the sum of the fitted signal and background. The hatched band shows the total uncertainty. The last bin includes overflow, where applicable. The post-fit results are obtained from the combined 2-POI fit described in Section 9.1. “Q-flip” is the electron background with mis-identified charge, as described in Section 7.

b -tagged jets are vetoed. To remove overlapping leptons, the angular separation between all lepton pairs must satisfy $\Delta R_{\ell\ell} > 0.1$. These selections constitute the Z -dominated SR.

For both the channels, dedicated ANNs are used to separate signal from background. In the Z -dominated channel, fifteen variables are used as input — these are summarised in Table 15 of Appendix A. The purpose of the single output classifier, $\text{ANN}_{Z\text{dom}}$, is to distinguish between the signal and the dominant WZ background. Accordingly, it is trained against this background process. The output is used as final discriminant in this channel.

In the Z -depleted channel, the three dominant background processes are $t\bar{t}$, WZ , and WWW . To simultaneously separate the WH signal from these backgrounds, a multi-classifier is used providing four distinct output nodes, $\text{ANN}_{Z\text{dep}}^i$, each describing the likeliness of the input event to stem from process i ($i = WH, t\bar{t}, WZ, WWW$) with the condition that $\sum_i \text{ANN}_{Z\text{dep}}^i = 1$. Table 16 of Appendix A summarises the input variables used in the Z -depleted channel.

To suppress processes containing top quarks, events with a high $\text{ANN}_{Z\text{dep}}^{t\bar{t}}$ score — greater than 0.25 — or at least one b -tagged jets are vetoed. Additionally, all lepton pairs must satisfy $\Delta R_{\ell\ell} > 0.1$ to remove overlapping leptons. These selections constitute the Z -depleted SR, whose final discriminant, $\text{ANN}_{Z\text{dep}}^\Delta$, is defined as:

$$\text{ANN}_{Z\text{dep}}^\Delta = \text{ANN}_{Z\text{dep}}^{WH} - \text{ANN}_{Z\text{dep}}^{WZ} - \text{ANN}_{Z\text{dep}}^{WWW}. \quad (1)$$

Figure 4 shows the post-fit distributions of the ANN discriminants and signal-sensitive kinematic variables in both the Z -dominated and Z -depleted SRs.

6.4 4ℓ channel

The ZH channel includes events with four isolated leptons with $p_T > 10$ GeV and total electric charge of zero. Events containing an SFOS lepton pair with $m_{\ell\ell} < 12$ GeV or a DFOS lepton pair with $m_{\ell\ell} < 10$ GeV are rejected to suppress the contamination from heavy-flavour quarkonia. Selected events are classified into channels according to the number of SFOS lepton pairs: 1-SFOS and 2-SFOS. Events with no SFOS lepton pairs are excluded.

The most prominent background process in the 4ℓ channel is ZZ production, with smaller contributions from top quark processes (e.g., $t\bar{t}Z$), processes with mis-identified leptons (e.g., $t\bar{t}W$), and WWZ production.

The reconstruction of the ZH process proceeds through the identification of the leptons from the Z boson, called ℓ_2 and ℓ_3 , as the SFOS lepton pair with invariant mass closest to the mass of the Z boson. The remaining two leptons, labelled ℓ_0 and ℓ_1 , are candidates for originating from the Higgs boson decay. This labelling scheme is demonstrated pictorially in the leading-order Feynman diagram, Figure 1(d). To suppress the $t\bar{t}Z$ process, events containing b -tagged jets are rejected. To reduce the ZZ background process in 2-SFOS events, the invariant mass of ℓ_0 and ℓ_1 , $m_{\ell_0\ell_1}$, is required to be below 50 GeV; to ensure orthogonality with the ATLAS $H \rightarrow ZZ^* \rightarrow 4\ell$ measurement [12], the 4-lepton invariant mass, $m_{4\ell}$, is required to be below 115 GeV or above 130 GeV. Finally, the angular separation between ℓ_0 and ℓ_1 , $\Delta R_{\ell_0\ell_1}$, is required to be larger than 0.2 to remove overlapping leptons.

The selections described above constitute the 1-SFOS and 2-SFOS SRs. For each SR, a discriminant based on a BDT is used to achieve a further separation between the ZH and ZZ processes. Independent BDTs

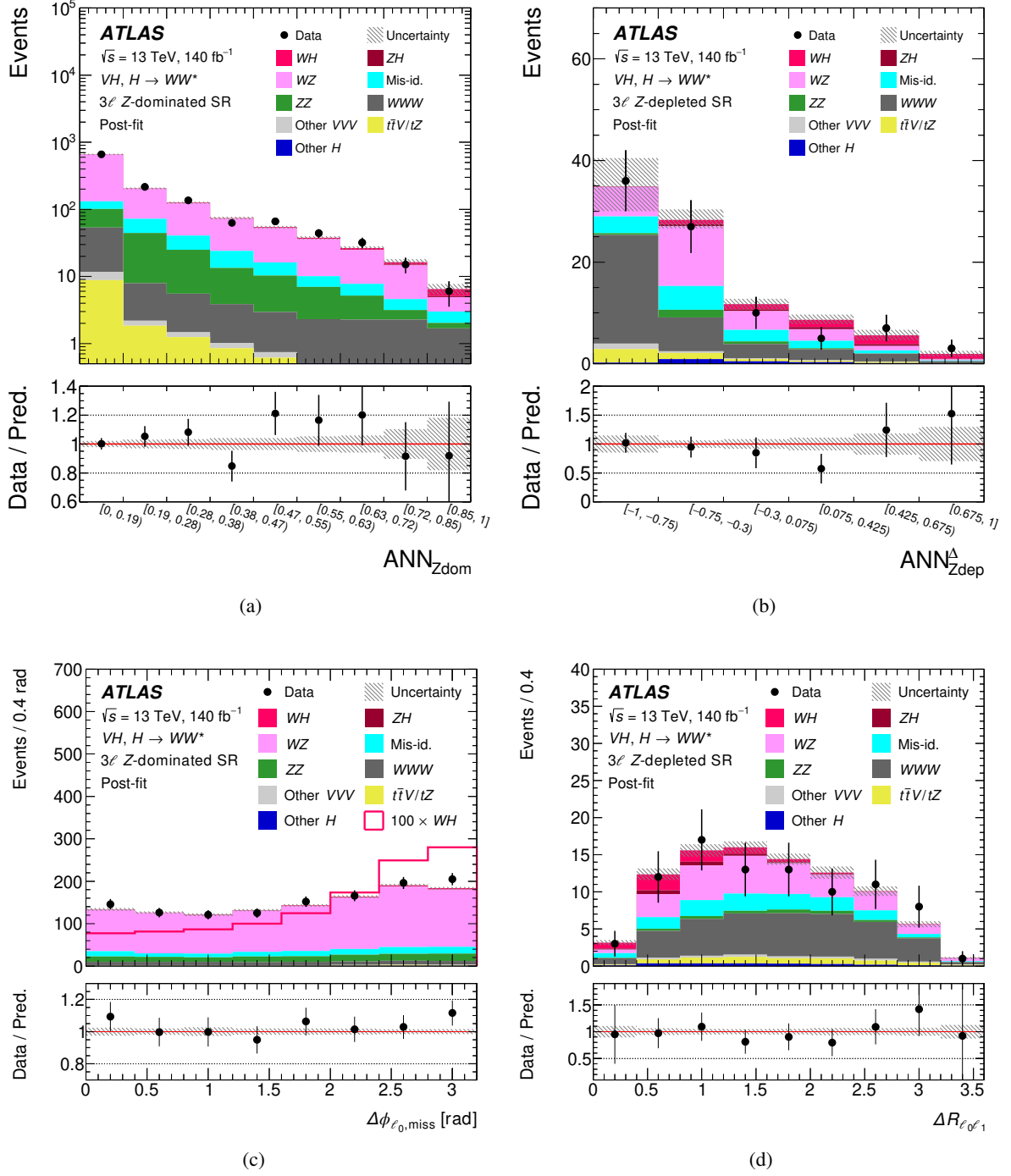


Figure 4: Post-fit distributions of (a) ANN_{Zdom} and (c) the azimuthal separation between lepton 0 and the $E_{\text{T}}^{\text{miss}}$, $\Delta\phi_{\ell_0, \text{miss}}$, in the Z-dominated SR as well as (b) $\text{ANN}_{\text{Zdep}}^\Delta$ and (d) the angular distance between leptons 0 and 1, $\Delta R_{\ell_0 \ell_1}$, in the Z-depleted SR. In (c), the post-fit WH signal yield is overlaid. The lower panel shows the ratio of the data to the sum of the fitted signal and background. The last bin includes overflow, where applicable. The post-fit results are obtained from the combined 2-POI fit described in Section 9.1.

are trained for each SR but sharing a common set of input variables, which are summarised in Table 17 of Appendix A.

Figure 5 shows the post-fit distributions of the BDT discriminants and signal-sensitive kinematic variables in the two 4ℓ SRs.

6.5 STXS categorisation

The Stage 1.2 STXS categorisation scheme for VH production is split by the production mode ($q\bar{q} \rightarrow WH$, $q\bar{q} \rightarrow ZH$, and $gg \rightarrow ZH$), the p_T of the associated vector boson, and the number of jets, as shown in Figure 17 of Appendix B. Based on the expected sensitivity of the measurement, kinematic fiducial regions are merged to ensure each cross-section is measured with adequate precision, yielding a reduced categorisation schemes, p_T^V and STXS. In both the schemes, there is no splitting of events by jet multiplicity. The fiducial regions for each are shown in Table 4.

For the p_T^V scheme, the $q\bar{q} \rightarrow WH$, $q\bar{q} \rightarrow ZH$, and $gg \rightarrow ZH$ categories are merged into a single VH category which is inclusive in the decay of the vector boson and which is defined in the fiducial region $|y_H| < 2.5$ where y_H is the rapidity of the Higgs boson. The $250 \leq p_T^V < 400$ GeV and $p_T^V \geq 400$ GeV categories are merged into a single $p_T^V \geq 250$ GeV category. This yields four measured fiducial cross-sections.

In the STXS scheme, the $q\bar{q} \rightarrow W(\rightarrow \ell\nu)H$ category, written as $\ell\nu H$ for brevity, is measured independently of the $q\bar{q} \rightarrow Z(\rightarrow \ell\ell/\nu\nu)H$ and $gg \rightarrow Z(\rightarrow \ell\ell/\nu\nu)H$ categories, which are merged and written as $\ell\ell H$ for brevity. The $150 \leq p_T^V < 250$ GeV, $250 \leq p_T^V < 400$ GeV, and $p_T^V \geq 400$ GeV categories are merged into a single $p_T^V \geq 150$ GeV category. The EW qqH category with $60 \leq m_{jj} < 120$ GeV is measured using the opposite-sign 2ℓ channel. This yields seven measured fiducial cross-sections.

Table 4: Summary the differential cross-sections measured in the p_T^V and STXS schemes.

p_T^V scheme	STXS scheme
$VH, 0 \leq p_T^V < 75$ GeV	$\ell\nu H$ and $\ell\ell H, 0 \leq p_T^V < 75$ GeV
$VH, 75 \leq p_T^V < 150$ GeV	$\ell\nu H$ and $\ell\ell H, 75 \leq p_T^V < 150$ GeV
$VH, 150 \leq p_T^V < 250$ GeV	$\ell\nu H$ and $\ell\ell H, p_T^V \geq 150$ GeV
$VH, p_T^V \geq 250$ GeV	EW $qqH, 60 \leq m_{jj} < 120$ GeV

For each of the channels considered by the analysis, subregions of the corresponding SRs are defined which target the individual or pairs of the fiducial cross-sections above. The subregions are split using selections on reconstructed proxies of p_T^V ; the boundaries of these selections were scanned and chosen to ensure adequate expected sensitivity for all POIs measured by the corresponding channel. Table 5 summarises the p_T^V proxies and selections for each channel and the relevant p_T^V range for each subregion.

For the opposite-sign 2ℓ channel, the chosen proxy is the dijet transverse momentum, p_T^{jj} . For the same-sign 2ℓ channel, the chosen proxy is the scalar sum of the lepton, jet, and missing transverse momenta, $\sum |p_T|$. The same splitting is shared between the SS2 μ , SS2 e , and SSDF SRs.

For the 3ℓ channel, a regression ANN is used to reconstruct the transverse momentum of the W boson. The regression ANN receives a subset of the input variables used by the multi-classifier of the Z -depleted

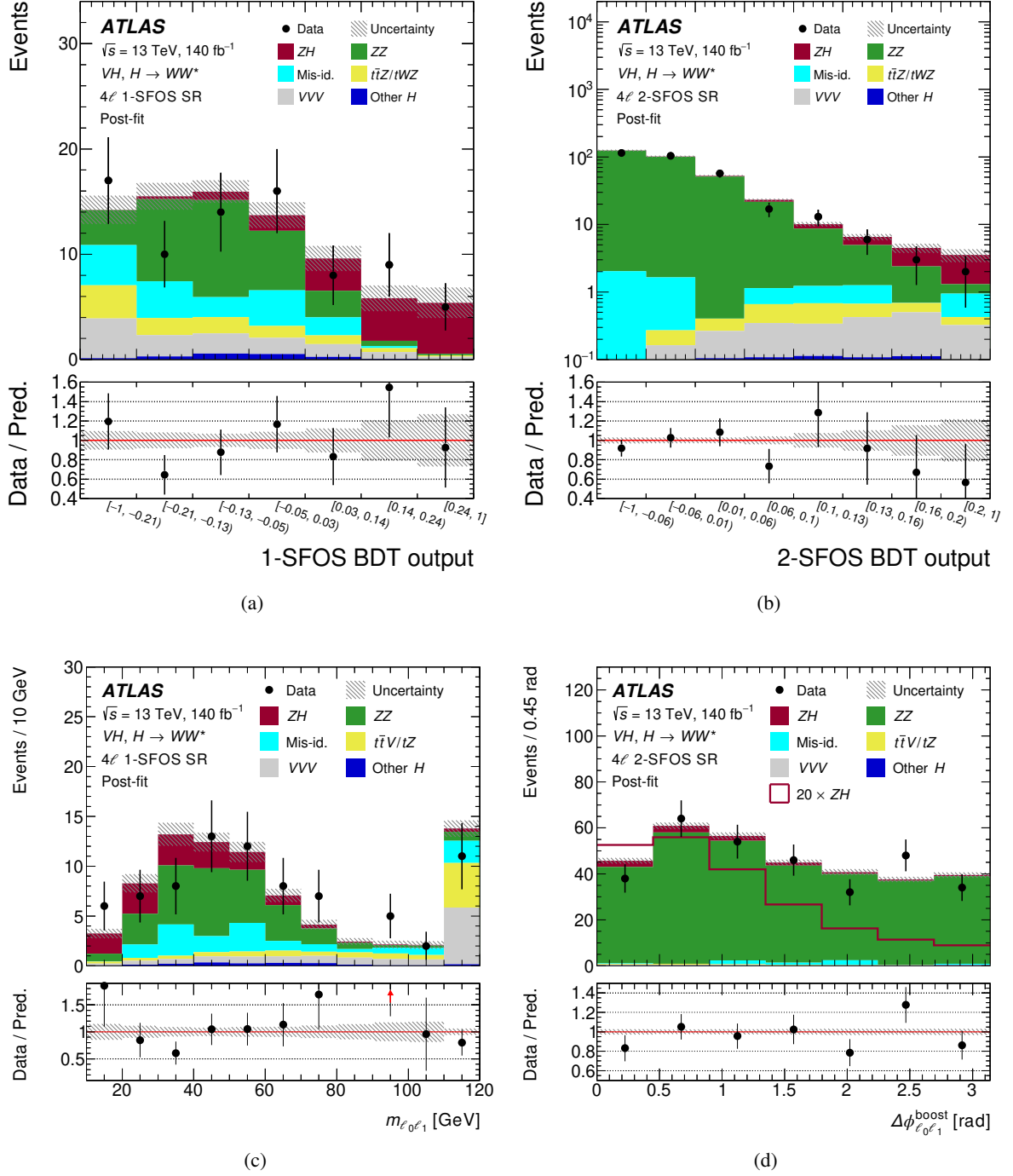


Figure 5: Post-fit distributions of (a) the BDT output and (c) the invariant mass of the Higgs boson candidate, $m_{\ell_0 \ell_1}$, in the 1-SFOS SR and (b) the BDT output and (d) the azimuthal separation between the leptons from the Higgs boson candidate in the rest frame of the Higgs boson, $\Delta\phi_{\ell_0 \ell_1}^{\text{boost}}$, in the 2-SFOS SR. In (d), the post-fit ZH signal yield is overlaid. The lower panel shows the ratio of the data to the sum of the fitted signal and background, and the arrow in (c) indicates the position of a point outside the vertical axis range. The hatched band shows the total uncertainty. The last bin includes overflow, where applicable. The post-fit results are obtained from the combined 2-POI fit described in Section 9.1.

SR — these input variables are summarised in Table 18 of Appendix A. Its output node, p_T^R , is chosen as a proxy for p_T^V and is utilised in both the Z -dominated and Z -depleted SRs.

For the 4ℓ channel, the chosen proxy is the transverse momentum of the Z boson candidate, $p_T^Z := p_T^{\ell_2\ell_3}$. The same splitting is applied to both the 1-SFOS and 2-SFOS SRs.

The performance of the proxies for several channels is shown in Figure 18 of Appendix B.

Table 5: Selections used to define the SRs entering the differential cross-section measurement. For each channel, the p_T^V proxy and the selections applied to it are shown. In the context of the Stage 1.2 STXS framework, the p_T^V range relevant to each SR is also shown. In the case of the same-sign 2ℓ channel, the selections are the same for each of the $SS2\mu$, $SS2e$, and $SSDF$ SRs; in the case of the 4ℓ channel, the selections are the same for each of the 1-SFOS and 2-SFOS SRs.

Channel	p_T^V proxy	Reconstructed SR	Relevant p_T^V range
Opposite-sign 2ℓ	Dijet transverse momentum, p_T^{jj}	$0 \leq p_T^{jj} < 160 \text{ GeV}$ $160 \leq p_T^{jj} < 260 \text{ GeV}$ $p_T^{jj} \geq 260 \text{ GeV}$	$0 \leq p_T^V < 150 \text{ GeV}$ $150 \leq p_T^V < 250 \text{ GeV}$ $p_T^V \geq 250 \text{ GeV}$
Same-sign 2ℓ	Scalar sum of lepton, jet, and missing transverse momenta, $\sum p_T $	$0 \leq \sum p_T < 200 \text{ GeV}$ $200 \leq \sum p_T < 320 \text{ GeV}$ $320 \leq \sum p_T < 460 \text{ GeV}$ $\sum p_T \geq 460 \text{ GeV}$	$0 \leq p_T^V < 75 \text{ GeV}$ $75 \leq p_T^V < 150 \text{ GeV}$ $150 \leq p_T^V < 250 \text{ GeV}$ $p_T^V \geq 250 \text{ GeV}$
3ℓ Z -dominated	Regression ANN for W transverse momentum, p_T^R	$0 \leq p_T^R < 90 \text{ GeV}$ $90 \leq p_T^R < 180 \text{ GeV}$ $p_T^R \geq 180 \text{ GeV}$	$0 \leq p_T^V < 75 \text{ GeV}$ $75 \leq p_T^V < 150 \text{ GeV}$ $p_T^V \geq 150 \text{ GeV}$
3ℓ Z -depleted	Regression ANN for W transverse momentum, p_T^R	$0 \leq p_T^R < 90 \text{ GeV}$ $90 \leq p_T^R < 180 \text{ GeV}$ $180 \leq p_T^R < 270 \text{ GeV}$ $p_T^R \geq 270 \text{ GeV}$	$0 \leq p_T^V < 75 \text{ GeV}$ $75 \leq p_T^V < 150 \text{ GeV}$ $150 \leq p_T^V < 250 \text{ GeV}$ $p_T^V \geq 250 \text{ GeV}$
4ℓ	Z boson transverse momentum, p_T^Z	$0 \leq p_T^Z < 75 \text{ GeV}$ $75 \leq p_T^Z < 150 \text{ GeV}$ $150 \leq p_T^Z < 250 \text{ GeV}$ $p_T^Z \geq 250 \text{ GeV}$	$0 \leq p_T^V < 75 \text{ GeV}$ $75 \leq p_T^V < 150 \text{ GeV}$ $150 \leq p_T^V < 250 \text{ GeV}$ $p_T^V \geq 250 \text{ GeV}$

Each channel uses the trained multivariate discriminant from the inclusive SR in each of its subregions; retraining of the discriminant was tested for the 3ℓ channel without producing appreciable improvements in sensitivity. The binning of the discriminant in each subregion is necessarily different from that of the inclusive SR, owing to smaller sample sizes. These distributions are provided as input to the combined fit. In the case of the STXS scheme, the opposite-sign 2ℓ SR is still split according to p_T^V ; however, only a single fiducial cross-section of $EW \text{ } qqH$ is measured.

Figure 6 shows the relative contributions of the reduced categories in all reconstructed SRs. In each case, the reduced categories provide the largest contributions in the corresponding SRs which aim to select

them.

Post-fit distributions for a subset of the SRs are shown in Figures 7 and 8 for the $2\ell/3\ell$ and 4ℓ channels, respectively.

7 Background modelling

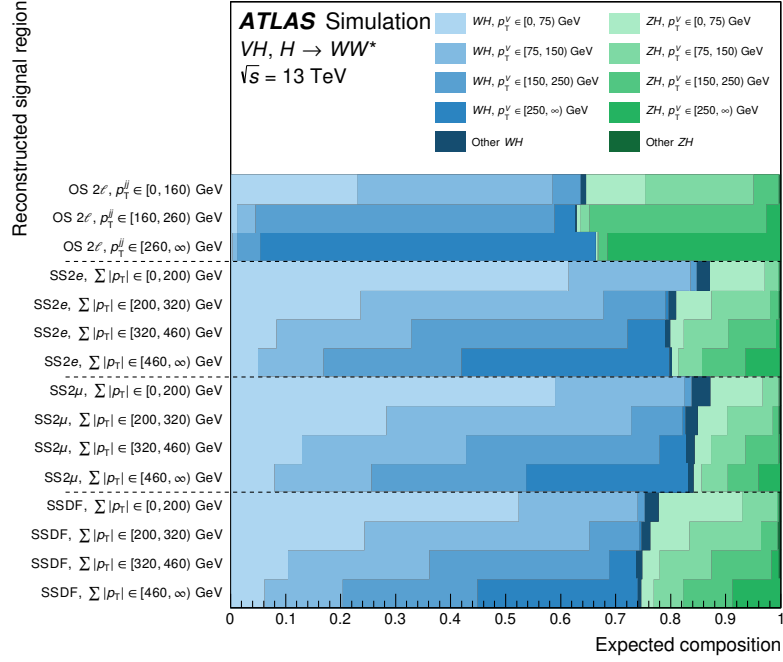
The background contamination in the SRs results from various physics processes, each modelled by pure data-driven prediction, pure MC prediction, or MC prediction normalised to data either using dedicated CRs or using only the SRs. The first method — pure data-driven prediction — is used to estimate the backgrounds with mis-identified leptons and electrons with mis-identified charge. In this estimate, rates and differential distributions (“shapes”) are extracted from data exploiting the method described in Section 7.1. In the second method, the rates and shapes are extracted from simulation and normalised to the predicted cross-sections. In the third method, the rates are fit to data using the CRs — which are orthogonal to the SRs — in addition to the SRs themselves, while the shapes are extracted from simulation. Table 6 summarises the method adopted for each background process in each signal region. The same methods are adopted for the STXS measurement with no change of the CR definitions.

Table 6: Summary of background modelling for each channel. “Normalised in the fit” are the background processes which are normalised in the fit but which do not have dedicated control regions; instead, their normalisation is determined by the signal discriminant. Data-driven background processes have at least one reconstructed mis-identified lepton.

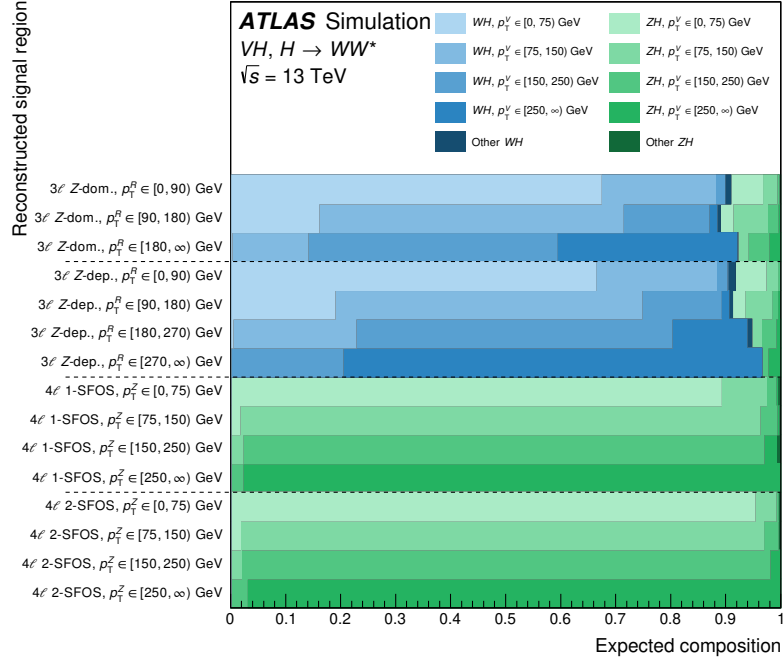
Channel	Pure MC	Normalised in the fit	Control region	Data-driven
Opposite-sign 2ℓ	WZ, ZZ, VVV, H (non- VH)	–	$t\bar{t}/Wt, Z+\text{jets}, WW$	$W+\gamma, W+\text{jets}$
Same-sign 2ℓ	$WW, ZZ, VVV, t\bar{t}V/tZ$	WZ	–	$V+\gamma, V+\text{jets}$
3ℓ	ZZ, VVV (non- WWW), $t\bar{t}V/tZ, H$ (non- VH)	WWW	WZ	$Z+\gamma, Z+\text{jets}, t\bar{t}/Wt, WW$
4ℓ	$VVV, t\bar{t}V/tWZ, H$ (non- VH)	–	ZZ	$WZ, t\bar{t}W/tZ, Z+\text{jets}, t\bar{t}/Wt$

In the opposite-sign 2ℓ channel, different CRs are defined to normalise the top, $Z+\text{jets}$, and WW background processes. The VH output node of the ANN is required to be less than 0.2 to define a region orthogonal to the SR, while dedicated selections on each of the ANN background nodes — $\text{ANN}_{\text{DFOS}}^{\text{top}}$, $\text{ANN}_{\text{DFOS}}^{Z+\text{jets}}$, and $\text{ANN}_{\text{DFOS}}^{WW}$ — are used to define three CRs. The top CR is used to normalise both the $t\bar{t}$ and Wt background processes. The purities for the top, $Z+\text{jets}$, and WW CRs are 72%, 77%, and 58%, respectively. In this section, a CR purity is defined as the number of events targeted by that CR relative to the total number of events, each calculated within that CR.

In the same-sign 2ℓ channel, the WZ background in the SR is normalised using a free fit parameter. The $t\bar{t}$ and $Z+\text{jets}$ background processes contribute when the charge of one lepton is wrongly assigned. An electron with a hard bremsstrahlung or a mis-measured track curvature has a large charge mis-identification probability, which is measured in data using a control sample of electrons from Z boson decays. In this sample, the WZ background is obtained from MC and the mis-identified lepton background is obtained from the data-driven procedure described in Section 7.1. The charge mis-identification probability is parametrised as a function of electron p_T with six bins and $|\eta|$ with six bins. The bins were chosen in accordance with the size of the event sample and the geometry of the detector. The charge mis-identification probability varies from $\mathcal{O}(10^{-5})$ for the electrons with $15 < p_T < 60 \text{ GeV}$ and $|\eta| < 0.6$ to $\mathcal{O}(10^{-1})$ for electrons with $p_T > 300 \text{ GeV}$ and $|\eta| > 2.3$. The measured charge mis-identification probabilities



(a)



(b)

Figure 6: Relative SM signal composition in terms of the reduced categories for each reconstructed SR of the (a) 2ℓ and (b) $3\ell/4\ell$ channels. The categorisation follows the p_T^V scheme; however, the WH and ZH templates are resolved to show their relative fraction in each SR. “Other WH/ZH ” includes forward Higgs bosons (i.e., Higgs bosons produced with rapidity $|y| > 2.5$) and — for the 3ℓ channels only — Higgs boson processes not included in the categorisation.

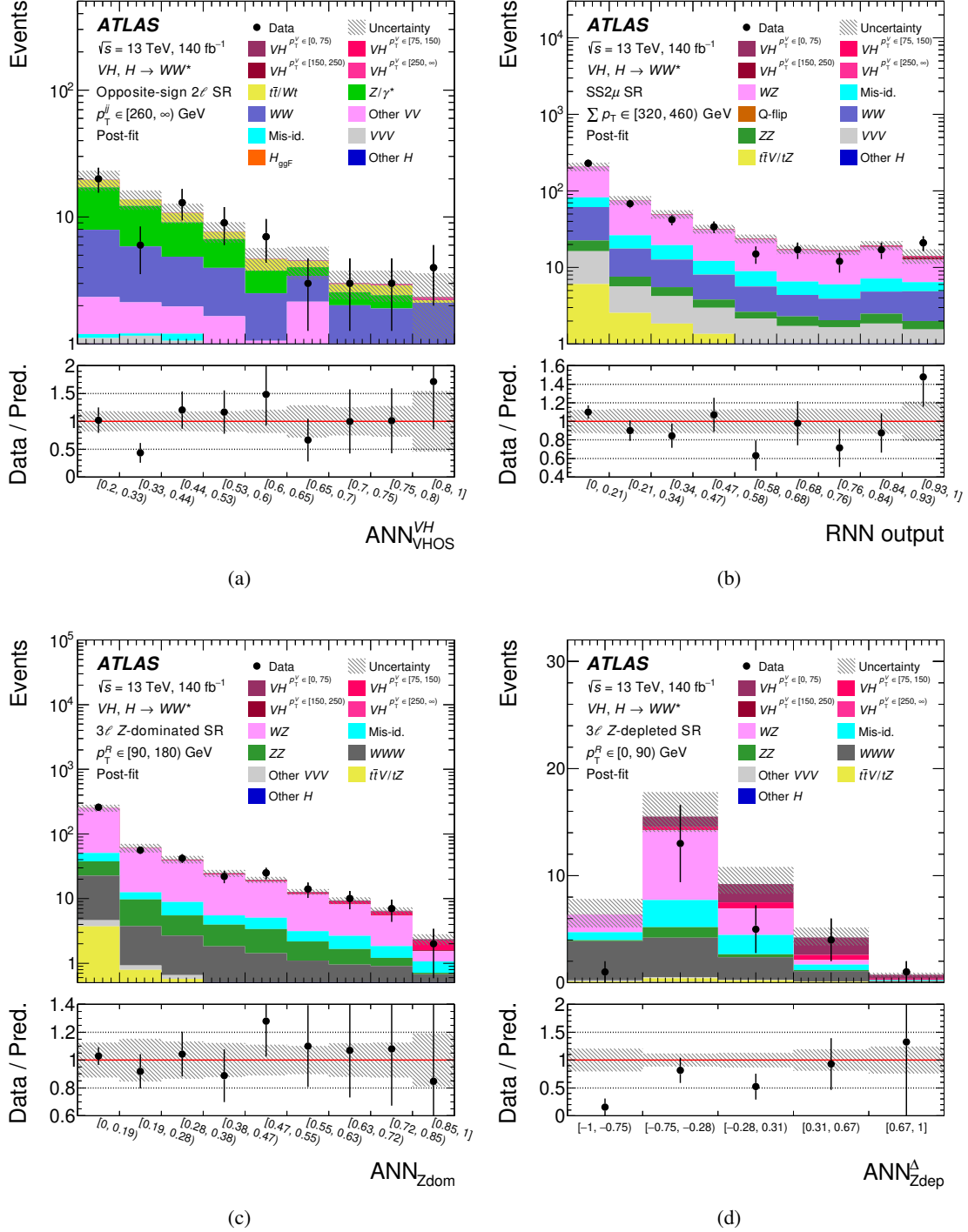


Figure 7: Post-fit ANN/RNN discriminants in a subset of the SRs considered by the analysis: (a) opposite-sign 2ℓ SR in the $p_T^{jj} \geq 260$ GeV subregion, (b) $SS2\mu$ SR in the $230 \leq \sum |p_T| < 460$ GeV subregion, (c) 3ℓ Z-dominated SR in the $90 \leq p_T^R < 180$ GeV subregion, and (d) 3ℓ Z-depleted SR in the $0 \leq p_T^R < 90$ GeV subregion. The lower panel shows the ratio of the data to the sum of the fitted signal and background. The hatched band shows the total uncertainty. The post-fit results are obtained from the combined fit for the p_T^V scheme, described in Section 9.1.

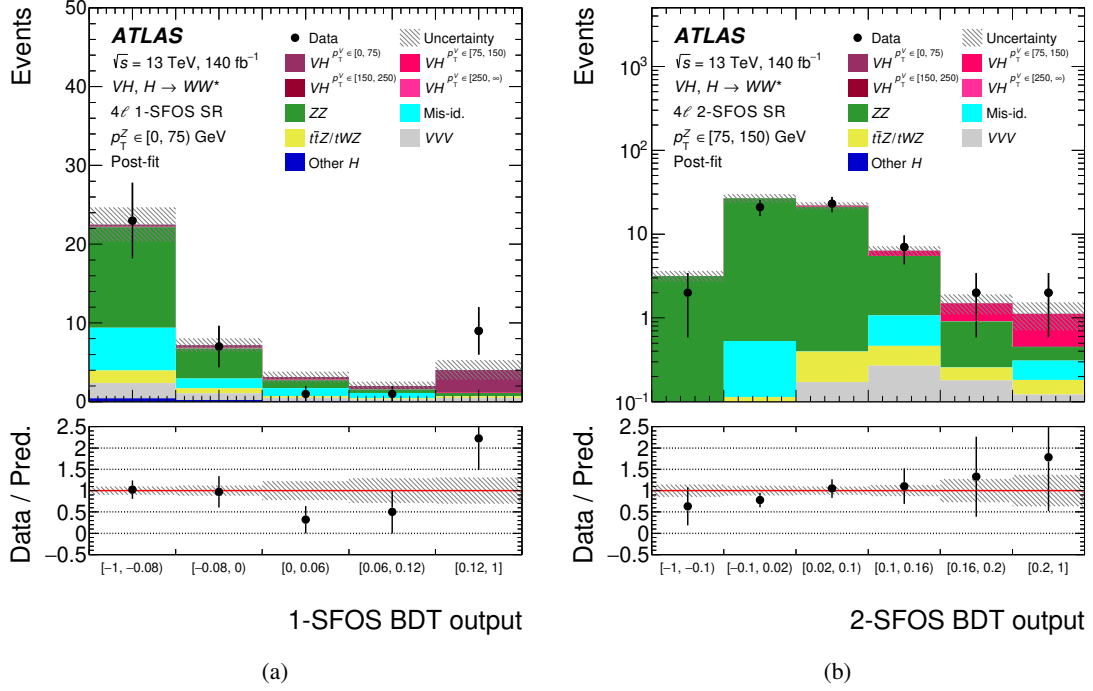


Figure 8: Post-fit BDT discriminants in a subset of the SRs considered by the analysis: (a) 4ℓ 1-SFOS SR in the $0 \leq p_T^Z < 75$ GeV subregion and (b) 4ℓ 2-SFOS SR in the $75 \leq p_T^Z < 150$ GeV subregion. The lower panel shows the ratio of the data to the sum of the fitted signal and background. The hatched band shows the total uncertainty. The post-fit results are obtained from the combined fit for the p_T^V scheme, described in Section 9.1.

are applied to a sample of opposite-sign leptons that satisfies the requirements of same-sign 2ℓ SRs, resulting in an estimate of the charge mis-identification background in each SR. The fraction of the charge mis-identification background is 26% in the SS2 e SR and 1.6% in the SSDF SR. The muon charge mis-identification probability is negligible in the p_T range relevant to this analysis.

The quality of the WZ modelling of the RNN for the same-sign 2ℓ channel was evaluated in a WZ -enriched validation region, defined using the selections common to each of the SS2 μ , SS2 e , and SSDF SRs but inclusive in the flavours of the leading isolated leptons. This validation region also requires an additional reconstructed lepton with $p_T > 15$ GeV and meeting looser quality criteria than those applied to the two leading isolated leptons. These looser leptons are reconstructed imperfectly and are similar to those missed in WZ events in which only two leptons are reconstructed. As a consequence, the RNN distribution in this region is sensitive to the quality of simulating events with real leptons from WZ . This validation region is also depleted in signal, with relative signal fractions of $< 1\%$ inclusively and $< 2\%$ in the signal-sensitive bin. A shape mis-modelling of the RNN shape for WZ events is observed, amounting to 30% less data than predicted in the bins of higher value of the RNN output. The source of this mis-modelling was found to be particularly enhanced at small values of the ΔR distribution between a lepton and its nearest jet. As the signal events tend to be at low values of this variable, the high-score regions of the RNN also exhibit this mis-modelling. A dedicated correction to the RNN shape in the WZ background is derived by fitting an exponential function to the ratio of data — with the non- WZ background subtracted — to the WZ background. The correction is then applied to the WZ background in each of the SS2 μ , SS2 e , and SSDF signal regions, with a 100% systematic uncertainty assigned to the correction and decorrelated among the

signal regions. This uncertainty reduces the expected sensitivity of the same-sign 2ℓ channel by $\sim 20\%$ with respect to what is obtained neglecting it. Good modelling is observed for events with three reconstructed leptons that are required to meet stringent quality criteria — as shown in Figure 10. Consequently, no additional correction or uncertainty is needed for the 3ℓ channels.

In the 3ℓ channel, WZ CRs are defined by requiring at least one SFOS lepton pair and by inverting the Z -veto selection with respect to the Z -dominated SR. The WZ background normalisation depends on the jet multiplicity of the events, so the CR is split into two regions containing events with no reconstructed jets and events with at least one reconstructed jet, respectively. The purity of the regions without jets is 93% and the purity of the region with one or more jets is 88%.

Motivated by an excess in the measurement of the $WWW + WH$ rate reported in Ref. [135], the WWW background is normalised in the fit procedure through a floating parameter and without a dedicated CR. The WWW process is the largest background in the 3ℓ Z -depleted channel followed by WZ production, and thus the value of the WWW normalisation factor is entirely determined by this channel. The measured normalisation factor, $2.2^{+0.7}_{-0.6}$, is consistent with the measured signal strength, 1.61 ± 0.25 , from the ATLAS WWW analysis [135].

In the 4ℓ channel, a dedicated CR is used to estimate the normalisation factor of the ZZ process. It is defined in the 2-SFOS channel after the b -jet veto by adding a set of requirements on the invariant mass of each of the lepton pairs. To select on-shell Z boson leptonic decays, $m_{\ell_2\ell_3}$ is required to be within ± 10 GeV of the Z boson mass. The invariant mass $m_{\ell_0\ell_1}$ must be above 50 GeV. The purity of this region is about 97%.

Figures 9, 10, and 11 show distributions of the multivariate discriminants, described in Section 6, in the relevant CRs. Good modelling is observed in the CRs for all of the distributions shown.

The background processes which are not normalised in the fit procedure or not measured via data-driven methods are estimated via pure MC prediction and normalised to their theoretical cross-sections.

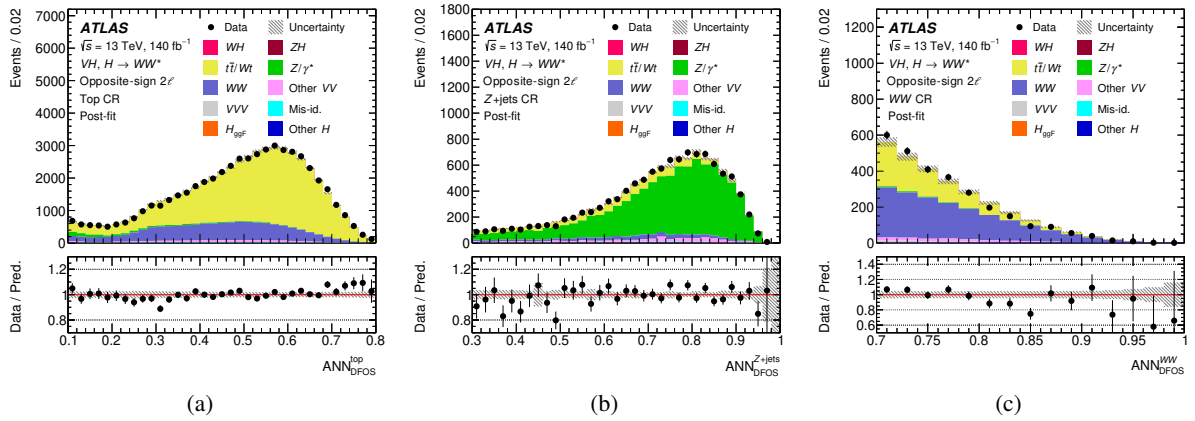


Figure 9: Post-fit distributions of (a) ANN_{VHOS}^{top} in the top CR, (b) ANN_{VHOS}^{Z+jets} in the $Z+jets$ CR, and (c) ANN_{VHOS}^{WW} in the WW CR of the opposite-sign 2ℓ channel. The lower panel shows the ratio of the data to the sum of the fitted signal and background. The hatched band shows the total uncertainty. The last bin includes overflow, where applicable. The post-fit results are obtained from the combined 2-POI fit described in Section 9.1.

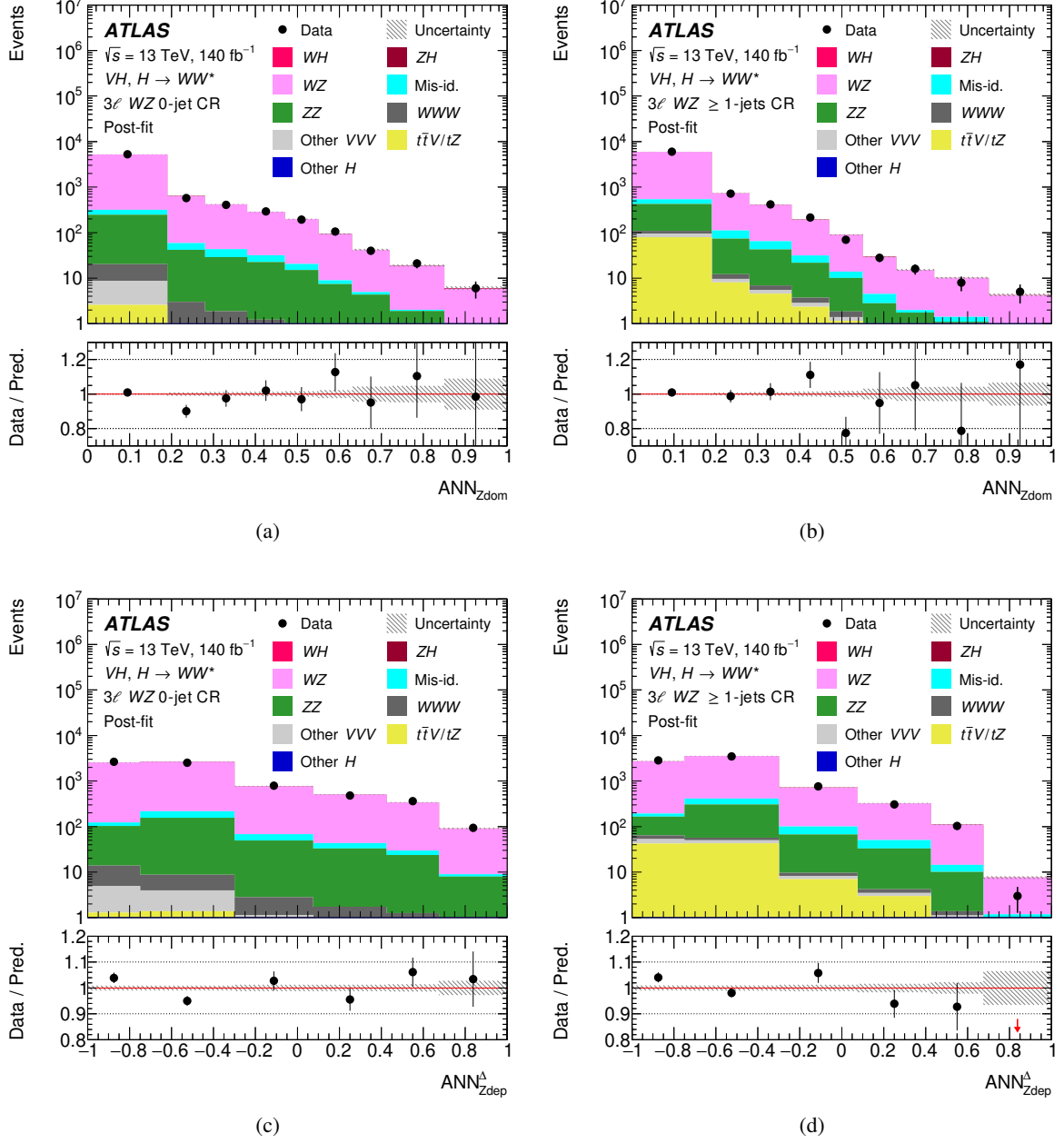


Figure 10: Post-fit distributions of ANN_{Zdom} in the (a) WZ CR with no jets and (b) WZ CR with at least one jet and of $\text{ANN}_{\text{Zdep}}^{\Delta}$ in the (c) WZ CR with no jets and (d) WZ CR with at least one jet. The binning of each distribution matches that used in the corresponding SR where that distribution is relevant. The lower panel shows the ratio of the data to the sum of the fitted signal and background, and the arrow in (d) indicates the position of a point outside the vertical axis range. The hatched band shows the total uncertainty. The post-fit results are obtained from the combined 2-POI fit described in Section 9.1.

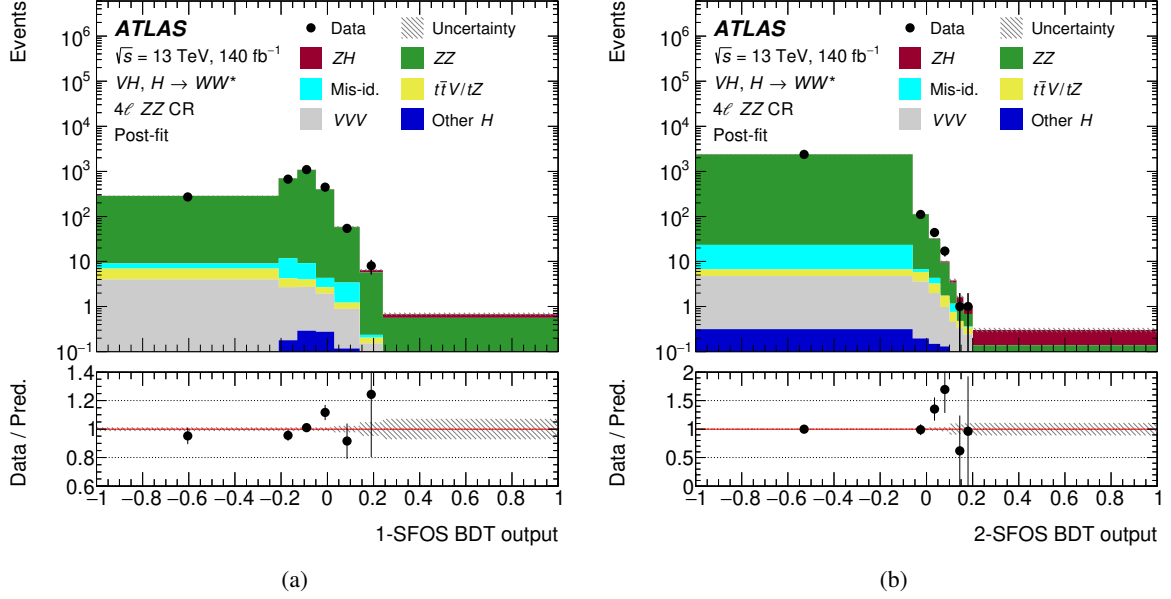


Figure 11: Post-fit distributions of the (a) 1-SFOS BDT output and (b) 2-SFOS BDT output in the ZZ CR. The binning of each distribution matches that used in the corresponding SR where that distribution is relevant. The lower panel shows the ratio of the data to the sum of the fitted signal and background. The hatched band shows the total uncertainty. The post-fit results are obtained from the combined 2-POI fit described in Section 9.1.

7.1 Backgrounds with non-prompt leptons

Non-prompt electrons can originate from the decays of heavy-flavour hadrons, mis-identification of hadronic jets, and photon conversions in the detector material, with an admixture depending on the lepton quality requirements and event categories. Non-prompt muons only originate from decays of heavy-flavour hadrons. The physical processes which contribute non-prompt leptons in each channel are summarised in Table 6.

All backgrounds with non-prompt leptons are estimated by weighting events from dedicated control samples with extrapolation factors. Except for requiring one of the lepton candidates to be an anti-identified (“anti-ID”) lepton, these control samples satisfy all of the nominal selections given in Table 2. An anti-ID lepton fails to meet the full identification criteria used to select identified (“ID”) leptons but satisfies a looser set of criteria. The extrapolation factors are defined as the ratios between the numbers of events with non-prompt lepton candidates being ID and anti-ID. Using the control samples, a maximum-likelihood fit measures the extrapolation factors such that the total number of weighted events matches the number of observed data events with only ID leptons after subtracting the expected contribution from processes with only prompt leptons.

The non-prompt electron background in 2ℓ and 3ℓ channels is estimated from simulation with data-driven corrections. The corresponding extrapolation factors are measured separately for three sources — heavy-flavour jets, light-flavour jets, and γ conversions — using three sets of samples enriched in $t\bar{t}$, Z +jets, and $Z+\gamma$ events, respectively. The simulated events with a non-prompt anti-ID electron are counted according to the source of the non-prompt electron and weighted by extrapolation factors. This yields three sets of extrapolation factors which are simultaneously measured using a maximum-likelihood fit. In contrast, the

non-prompt muon background in 2ℓ and 3ℓ channels is estimated by using a fully data-driven technique. From a sample enriched in $t\bar{t}$, the number of events with a non-prompt muon is calculated from the observed data after subtracting the expected contribution from processes with only prompt muons. The corresponding extrapolation factors are then obtained from a maximum-likelihood fit. The non-prompt electron and muon extrapolation factors are both measured in bins of lepton p_T .

The measurement of the non-prompt electron and muon extrapolation factors for the 4ℓ channel follows a similar procedure to the measurement of the non-prompt muon extrapolation factors for the 2ℓ and 3ℓ channels. The differences between the 2ℓ and 3ℓ channels are due to the looser lepton selection and the lower sample size available in the control samples. The extrapolation factors are measured in a sample enriched in Z +jets events and are inclusive in lepton p_T . Processes with two non-prompt leptons are accounted for in the extrapolation by applying a correction term evaluated in a sample where two of the lepton candidates are anti-ID.

8 Systematic uncertainties

The experimental and theoretical sources of systematic uncertainties are evaluated using MC samples and their effects are included in the statistical analysis. The impact of each uncertainty is estimated per analysis region and per bin. A list of the systematic uncertainty sources with corresponding impact on the measurement is shown in Section 9.2.

The theoretical and experimental uncertainties are varied in a correlated way for all MC processes across all signal and control region bins, which considers the normalisation extrapolation from control to signal regions.

8.1 Experimental uncertainties

Experimental uncertainties associated with leptons originate from the reconstruction, identification, and isolation efficiencies [120, 121] and from the scale and resolution of the energy or momentum [136, 137]. For jets, uncertainties arise from the jet energy scale and resolution [126], the performance of the pile-up jet tagger [127, 129], and the b -jet identification [131]. Furthermore, uncertainties due to the trigger selection [117, 118] and the soft term in the reconstruction of the E_T^{miss} [132] are estimated. The uncertainty in the modelling of pile-up for simulated samples is estimated by varying the reweighting to the profile in data within its uncertainties. The uncertainty in the integrated luminosity is 0.83% [30], which is measured using the LUCID-2 detector [138]. The luminosity uncertainty is applied to the signal and background processes which are normalised to theoretical predictions.

For the data-driven estimate of the backgrounds attributed to mis-identified leptons and electrons with mis-identified charge, uncertainties are considered for the availability of data and MC statistics, variations on the theoretical predictions of the prompt lepton backgrounds, variations in the analysis selections, and the self-consistency of the method.

The largest sources of experimental uncertainties are the following: jet energy scale and resolution uncertainties for the opposite-sign 2ℓ channel; uncertainties relating to the RNN shape for WZ , the estimate of the mis-identified lepton background, and the estimate of the electron background with mis-identified

charge for the same-sign 2ℓ channel; and uncertainties relating to the estimate of the mis-identified lepton background and the isolation of leptons for the 3ℓ and 4ℓ channels.

8.2 Theoretical uncertainties

The impact of the theoretical sources of uncertainty is evaluated by reweighting MC events or by using alternative MC samples, which are detailed in Table 1. Uncertainties computed as differences between two samples are symmetrised. Uncertainties in background processes with negligible contributions in the signal regions are not considered. All uncertainties are computed using detector-level events unless specified otherwise.

For all processes, the uncertainty in missing higher-order corrections is computed as the maximum variation of the envelope resulting from simultaneous variations of the renormalisation and factorisation scales by factors of 0.5 and 2. The uncertainty in the central value of the PDF set is evaluated by comparing the nominal weight to alternative weights, the latter encapsulating the experimental and model-related uncertainties entering the PDF fit. The uncertainty in the central value of the strong coupling constant, $\alpha_s = 0.1180 \pm 0.0015$, is evaluated by varying it up and down by its uncertainty and recalculating the event weight for each case. The midpoint between these varied weights is symmetrised and assigned as the corresponding uncertainty in the nominal weight.

The uncertainty in the PS modelling for the Higgs boson processes is assigned as the difference between the nominal sample showered with PYTHIA 8 and an alternative sample showered with HERWIG 7. For the VH signal process, this uncertainty is computed using particle-level events with selections similar to those on detector-level and the same multivariate discriminants.

The merging of the NLO and LO matrix elements for the VV processes, which are modelled by SHERPA 2.2.2, is performed using the MEPS@NLO prescription [90]. A jet merging uncertainty (“CKKW”) is assigned by varying the nominal threshold (20 GeV) separating the ME and the PS up (30 GeV) and down (15 GeV). Similarly, a PS resummation uncertainty (“QSF”) is assigned by varying the resummation scale up and down by factors of 2 and 0.5, respectively. The uncertainty due to the choice of the PS momentum recoil scheme (“CSSKIN”) is computed by comparing the nominal sample, which uses the recoil scheme described in Ref. [86], to an alternative sample, which uses the recoil scheme described in Ref. [139]. In a manner analogous to the PS modelling uncertainty in VH , the CKKW, QSF, and CSSKIN uncertainties in VV are all computed using particle-level events.

The uncertainty in the ME and PS modelling for the VVV and Z +jets processes are assigned as the difference between the nominal SHERPA samples and alternative samples generated with MADGRAPH5_AMC@NLO and showered with PYTHIA 8.

The uncertainty in the hadronisation and fragmentation modelling for the $t\bar{t}$ sample is assigned as the difference between the nominal sample showered with PYTHIA 8 and an alternative sample showered with HERWIG 7. The uncertainty in the choice of generator and matching algorithm is assigned as the difference between the nominal sample generated with POWHEG and an alternative sample generated with MADGRAPH5_AMC@NLO. Uncertainties in the modelling of initial- and final-state radiation are assigned by varying scale, resummation, and showering parameters.

In the total cross-section measurement, signal modelling uncertainties are computed separately for the WH and ZH processes and decorrelated in the fit. The MC weights are varied using the inclusive samples and the uncertainties are computed in each signal and control region. In the differential cross-section

measurement, signal modelling uncertainties are computed for each fiducial bin of the corresponding scheme, using the binning defined in the STXS Stage 1.2 convention and without applying any merging. For the missing higher-order QCD corrections, the uncertainty model described in Ref. [140] is used, resulting in a set of uncertainties in the total cross-section correlated across fiducial bins and a set of migration uncertainties across the fiducial bin boundaries. Seven independent QCD uncertainty components are considered. One component affects the total production cross-section, while the other six are pure migration uncertainties. Four of these components are designed to model uncertainties across p_T^V boundaries (75, 150, 250, and 400 GeV) while the other two affect jet bin migrations across the $n_{\text{jets}} = 1$ and 2 boundaries. The uncertainties affect both the analysis acceptance, defined as the fraction of events in a fiducial region passing the analysis selection, and the predicted cross-section per fiducial region.

The largest sources of theoretical uncertainties are the following: uncertainties in the hadronisation/fragmentation modelling of $t\bar{t}$ production and on the ME/PS modelling of Z +jets production for the opposite-sign 2ℓ channel; uncertainties in the PS modelling of WZ production for the same-sign 2ℓ channel; uncertainties in the choice of PS recoil scheme for WZ production and on the ME/PS modelling of WWW production for the 3ℓ channel; and uncertainties in the missing higher-order corrections to ZH production and on the $H \rightarrow WW^*$ branching ratio for the 4ℓ channel.

9 Fit procedure and results

9.1 Fit procedure

A binned likelihood function is constructed as a product of Poisson probability terms over the bins of the different SRs defined in Section 6. The binned likelihood function is parameterised in terms of a signal strength, μ , defined as the ratio of the observed signal yield to that predicted by the SM. The signal strength constitutes the POI of the measurement. Additionally, a Poisson probability term is added for each CR and used to fit the normalisation of its corresponding background process in the combined measurement via a floating normalisation factor. Systematic uncertainties enter as nuisance parameters in the likelihood function — primarily in the form of Gaussian distributed constraints — and their correlations are taken into account. The final results are obtained using the profile likelihood method [141].

For the cross-section measurement of WH and ZH production, two fit scenarios are considered: a combined 1-POI fit, where the WH and ZH yields are simultaneously scaled by a single POI, μ_{VH} , and a combined 2-POI fit, where the WH and ZH yields are independently scaled by two POIs, μ_{WH} and μ_{ZH} , respectively. In the case of the 1-POI fit, the SM expectation is assumed for the cross-section ratio of the WH and ZH production processes.

Table 7 summarises the regions entering the combined fit. A similar prescription is followed for the differential measurement, where the SRs in the table are split according to Table 5 and the four (p_T^V scheme) or seven (STXS scheme) fiducial cross-sections of interest are independently scaled by an equal number of POIs. The cross-sections for non- VH Higgs boson processes are fixed to their SM expectations in the combined fit.

For both the total and differential cross-section measurements, the pure normalisation components of the signal theory uncertainties are factorised from the pure acceptance components — only the latter components enter the cross-section fit.

Table 7: Summary of SRs — including the chosen SR discriminants — and CRs in each channel entering the combined total cross-section fit. The SR discriminants enter the combined fit as histograms, and the corresponding figures showing the post-fit histograms are referred in parentheses after each SR discriminant; the CRs enter the combined fit as counters.

Channel	SR	SR discriminant	Relevant CR(s)
Opposite-sign 2ℓ	–	ANN_{DFOS} (2(a))	Top, Z+jets, WW
Same-sign 2ℓ	$SS2\mu$	RNN output (3(a))	–
	$SS2e$	RNN output (3(b))	
	$SSDF$	RNN output (3(c))	
3ℓ	Z-dominated	ANN_{Zdom} (4(a))	WZ 0-jet, $WZ \geq 1$ -jets
	Z-depleted	$\text{ANN}_{\text{Zdep}}^{\Delta}$ (4(b))	
4ℓ	1-SFOS	1-SFOS BDT output (5(a))	ZZ
	2-SFOS	2-SFOS BDT output (5(b))	

9.2 Results

9.2.1 Total cross-section results

The post-fit MC and data yields in each SR are shown in Table 8. The observed data yields agree, in both the rate and shape, within uncertainties with the expected yields from MC in all SRs.

Table 9 shows the expected and observed values of the signal strengths for the single-channel, combined 1-POI, and combined 2-POI fits, and Table 10 shows the observed values of the normalisation factors for the combined 2-POI fit. Figure 12 shows the observed values of the total WH , ZH , and VH cross-sections times the $H \rightarrow WW^*$ branching ratio, normalised to the SM predictions, and Figure 13 shows the observed profile likelihood for the combined and single-channel results. Figure 14 shows the two-dimensional likelihood contours of the observed values of $\sigma_{ZH} \times \mathcal{B}_{H \rightarrow WW^*}$ vs. $\sigma_{WH} \times \mathcal{B}_{H \rightarrow WW^*}$ compared with the SM predictions.

For the combined 1-POI fit, the VH signal strength is measured to be:

$$\mu_{VH} = 0.92_{-0.20}^{+0.21} (\text{stat.})_{-0.12}^{+0.13} (\text{syst.}),$$

corresponding to a 4.5σ significance over the background-only hypothesis and consistent with the SM expectation with a p -value of 73%. The total VH cross-section times the $H \rightarrow WW^*$ branching ratio is measured to be:

$$\sigma_{VH} \times \mathcal{B}_{H \rightarrow WW^*} = 0.44_{-0.09}^{+0.10} (\text{stat.})_{-0.05}^{+0.06} (\text{syst.}) \text{ pb},$$

in agreement with the SM expectation of 0.48 ± 0.01 pb [21].

For the combined 2-POI fit, the WH and ZH signal strengths are measured to be:

$$\begin{aligned} \mu_{WH} &= 0.48_{-0.25}^{+0.26} (\text{stat.})_{-0.16}^{+0.18} (\text{syst.}), \\ \mu_{ZH} &= 1.6_{-0.4}^{+0.5} (\text{stat.}) \pm 0.2 (\text{syst.}). \end{aligned} \tag{2}$$

Table 8: Post-fit signal, background, and observed data yields in each SR as measured by the 2-POI fit. The Z+jets and top processes for a given channel correspond to those with only prompt leptons, as described in Section 7. The uncertainties correspond to the total of all statistical and systematic sources. The quadrature sum of the individual sources may differ from the total uncertainty due to correlations.

Process	OS 2ℓ				SS 2ℓ				SSDF			
	SS 2μ				SS $2e$							
WH	11	\pm	7	33	\pm	21	12	\pm	8	48	\pm	31
ZH	20	\pm	6	7.2	\pm	2.2	4.1	\pm	1.2	14	\pm	4
Other Higgs	61	\pm	14	19.0	\pm	2.2	9.3	\pm	1.1	33	\pm	4
WW	260	\pm	50	260	\pm	40	109	\pm	15	380	\pm	50
WZ	41.5	\pm	3.1	1420	\pm	150	850	\pm	90	2630	\pm	270
ZZ	7.8	\pm	0.7	144	\pm	17	101	\pm	8	309	\pm	28
$Z+\gamma$	10	\pm	7	—			—			—		
VVV	19	\pm	6	190	\pm	50	86	\pm	24	290	\pm	80
Z +jets	302	\pm	27	—			—			—		
Top	1020	\pm	70	33.0	\pm	2.7	16.2	\pm	1.3	54	\pm	5
Mis-identified leptons	25	\pm	6	320	\pm	130	1090	\pm	100	2080	\pm	260
Charge-flip electrons			—	—			930	\pm	70	109	\pm	8
Total	1780	\pm	40	2420	\pm	50	3200	\pm	50	5950	\pm	70
Observed			1788			2438			3233			5906

Process	3ℓ				4ℓ							
	Z-dominated		Z-depleted		1-SFOS		2-SFOS					
WH	12	\pm	7	6	\pm	4	—	—				
ZH	4.4	\pm	1.3	1.7	\pm	0.5	15	\pm	4	10.7	\pm	3.2
Other Higgs	1.80	\pm	0.17	2.83	\pm	0.31	1.88	\pm	0.22	0.68	\pm	0.08
WZ	877	\pm	20	24.6	\pm	1.6	—			—		
ZZ	130	\pm	17	2.63	\pm	0.28	29.2	\pm	1.5	306	\pm	9
WWW	64	\pm	16	35	\pm	9	—			—		
WWZ	3.81	\pm	0.09	1.64	\pm	0.05	10.9	\pm	1.0	1.58	\pm	0.14
WZZ	0.310	\pm	0.008	< 0.1			0.447	\pm	0.034	< 0.1		
Top	14.5	\pm	1.3	4.8	\pm	0.4	8.8	\pm	0.9	1.45	\pm	0.14
Mis-identified leptons	98	\pm	14	12.5	\pm	2.9	14.5	\pm	3.2	5.5	\pm	1.2
Total	1205	\pm	23	92	\pm	8	80	\pm	5	326	\pm	9
Observed			1237			88			79			316

The observed values of μ_{WH} and μ_{ZH} are compatible at a level of 2.0σ , and they are consistent with the SM expectations with a p -value of 13%. The observed ZH result exceeds the SM prediction due to an excess in the 4ℓ 1-SFOS SR. The observed μ_{WH} is smaller than the SM prediction due to deficits in the 3ℓ Z -depleted SR and the same-sign 2ℓ channel. The total WH and ZH cross-sections times the $H \rightarrow WW^*$ branching ratio are measured to be:

$$\begin{aligned}\sigma_{WH} \times \mathcal{B}_{H \rightarrow WW^*} &= 0.14^{+0.08}_{-0.07} \text{ (stat.)} \pm 0.05 \text{ (syst.) pb}, \\ \sigma_{ZH} \times \mathcal{B}_{H \rightarrow WW^*} &= 0.31^{+0.09}_{-0.08} \text{ (stat.)} \pm 0.03 \text{ (syst.) pb},\end{aligned}\tag{3}$$

while the SM expectations are 0.294 ± 0.009 pb (WH) and $0.190^{+0.009}_{-0.008}$ pb (ZH), respectively [21].

Table 9: The observed values of the signal strengths and the corresponding statistical significances, Z_0 , for the single-channel fits and the combined 1- and 2-POI fits. For each fit, both the expected and observed results are shown. The uncertainties correspond to the total of all statistical and systematic sources. The statistical significances are quoted in units of standard deviations above the background-only hypothesis.

Channel	POI / Z_0	Expected	Observed
Opposite-sign 2ℓ	μ_{VH}	1.0 ± 1.0	$1.9^{+1.1}_{-1.0}$
	Z_0	1.0	1.9
Same-sign 2ℓ	μ_{WH}	1.0 ± 0.5	0.1 ± 0.5
	Z_0	1.8	0.2
3ℓ	μ_{WH}	1.0 ± 0.4	0.6 ± 0.4
	Z_0	2.8	1.8
4ℓ	μ_{ZH}	$1.0^{+0.5}_{-0.4}$	1.6 ± 0.5
	Z_0	3.1	4.4
Combined 1-POI	μ_{VH}	$1.00^{+0.26}_{-0.24}$	$0.92^{+0.25}_{-0.23}$
	Z_0	4.8	4.5
Combined 2-POI	μ_{WH}	$1.00^{+0.35}_{-0.33}$	$0.48^{+0.32}_{-0.30}$
	μ_{ZH}	$1.0^{+0.5}_{-0.4}$	1.6 ± 0.5
	Z_0^{WH}	3.3	1.6
	Z_0^{ZH}	3.1	4.5

Table 10: The observed values of the background normalisation factors for the combined 2-POI fit. The uncertainties correspond to the total of all statistical and systematic sources.

Channel	Background	Normalisation factor
Opposite-sign 2ℓ	Top	$1.0^{+0.3}_{-0.2}$
	Z+jets	$0.86^{+0.15}_{-0.14}$
	WW	$0.9^{+0.3}_{-0.2}$
Same-sign 2ℓ	WZ	$0.90^{+0.17}_{-0.16}$
3ℓ	WZ 0-jet	1.03 ± 0.06
	WZ ≥ 1 -jets	$0.88^{+0.16}_{-0.15}$
	WWW	$2.2^{+0.7}_{-0.6}$
4ℓ	ZZ	0.98 ± 0.07

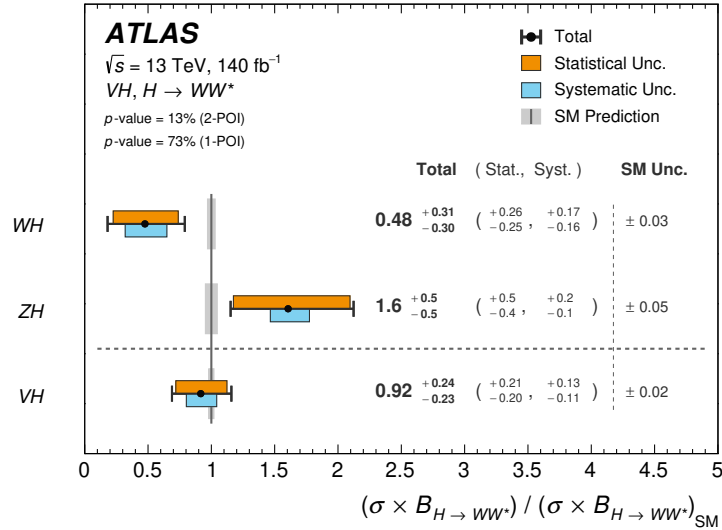


Figure 12: Best-fit values of the total WH , ZH , and VH cross-sections times the $H \rightarrow WW^*$ branching ratio. The WH/ZH and VH results are obtained from the combined 2- and 1-POI fits, respectively. Each measurement is normalised to its SM prediction. The black error bars, orange boxes, and blue boxes show the total, statistical, and systematic uncertainties in the measurements, respectively. The grey bands represent the theory uncertainty of the corresponding Higgs boson production mode.

Table 19 of Appendix C shows the relative impact of the different sources of uncertainty in the observed values of the total cross-sections. For all fit scenarios, the observed results are dominated by statistical uncertainties in data. For the WH measurement, the RNN shape uncertainty for WZ (23%) and the WZ 0-jet (11%) and VVV (12%) background uncertainties are the dominant systematic uncertainties; for the ZH measurement, muon experimental uncertainties (4.1%) are the dominant systematic uncertainties.

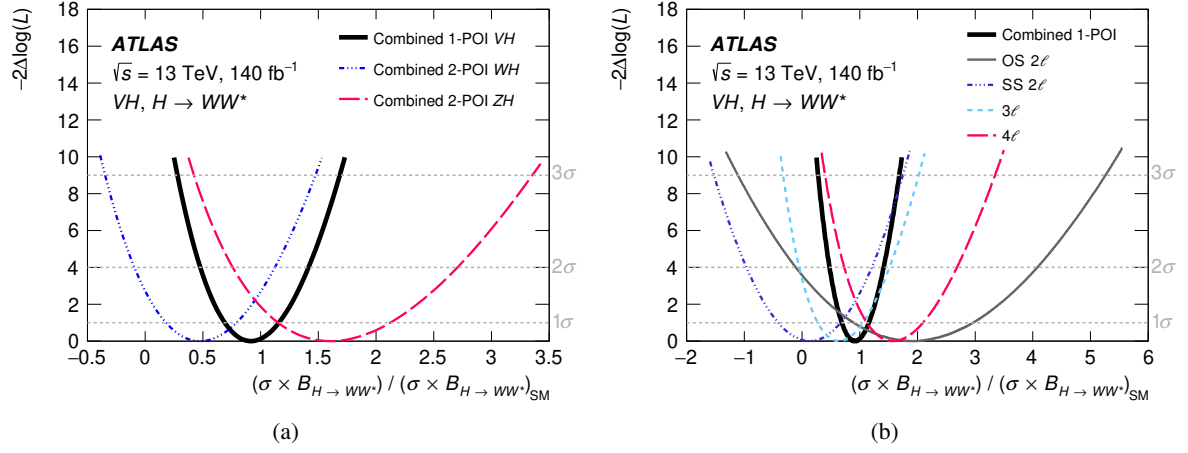


Figure 13: Observed profile likelihood as a function of $\sigma \times \mathcal{B}_{H \rightarrow WW^*}$ normalised by the SM expectation for (a) the VH and WH/ZH measurements from the combined 1- and 2-POI fits, respectively, and (b) the single-channel measurements.

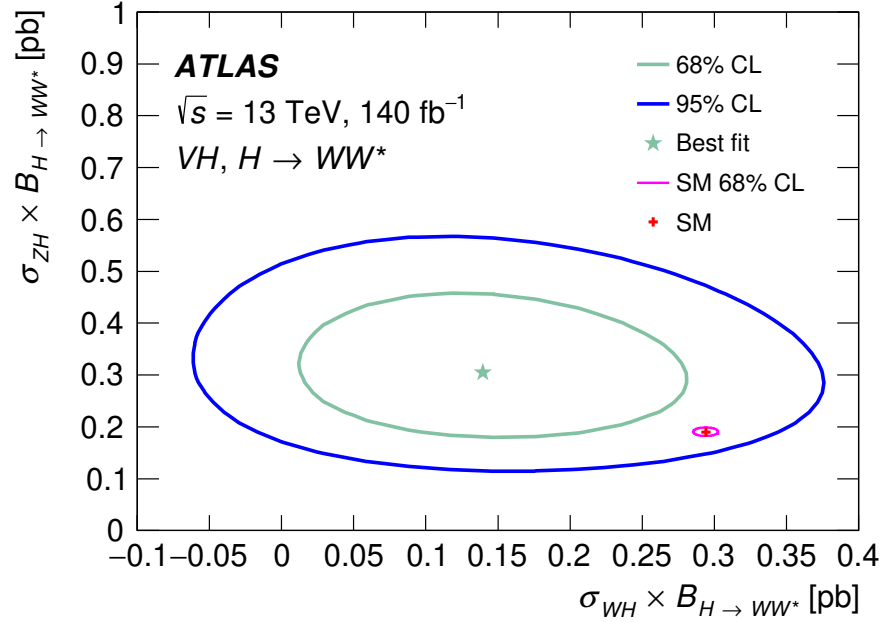


Figure 14: Two-dimensional likelihood contours of the observed values of $\sigma_{ZH} \times \mathcal{B}_{H \rightarrow WW^*}$ vs. $\sigma_{WH} \times \mathcal{B}_{H \rightarrow WW^*}$ at the 68% and 95% confidence levels (CLs) compared with the predictions from the SM. The 68% confidence level on the SM predictions for the ZH and WH cross-sections times branching fraction is indicated by the magenta ellipse.

9.2.2 Differential cross-section results

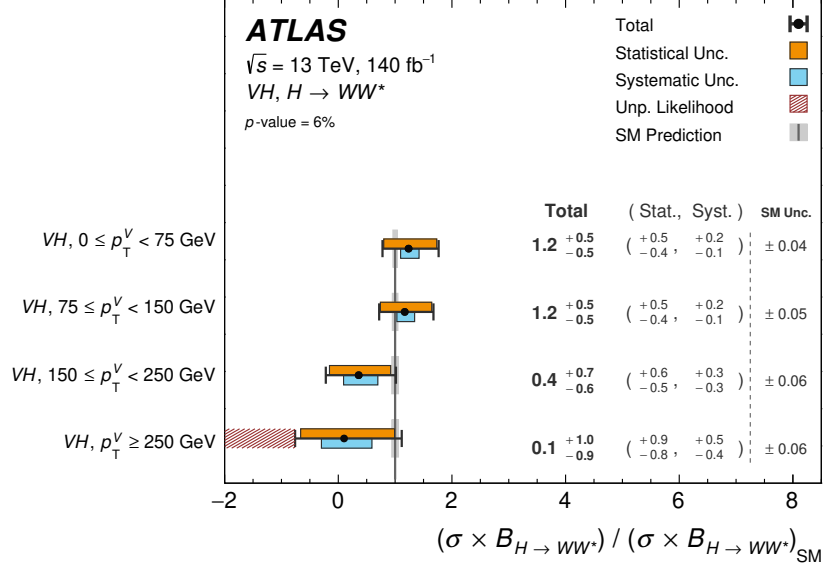
For the differential cross-section measurement, two fits are performed: one for the p_T^V scheme and one for the STXS scheme. The analysis regions are the same for both the fits. The signal samples are split into signal templates following the STXS Stage 1.2 categorisation. The cross-section for each template is scaled by its own POI, $(\sigma \times \mathcal{B}_{H \rightarrow WW^*})/(\sigma \times \mathcal{B}_{H \rightarrow WW^*})_{\text{SM}}$. The POIs are correlated (i.e., coherently tuned via a single POI) to provide the results in merged bins of the STXS categorisation; for example, the POIs for different jet multiplicity bins are correlated as are the POIs for the $250 \leq p_T^V < 400$ GeV and $p_T^V \geq 400$ GeV bins.

For the p_T^V scheme, the POIs for the WH and ZH production modes are correlated to provide combined VH production mode POIs; for the $V \rightarrow q\bar{q}$ signal template fit, the signal is split into four p_T^V bins and the POIs are correlated with those of the $V \rightarrow \ell\ell/\nu\nu$ channels.

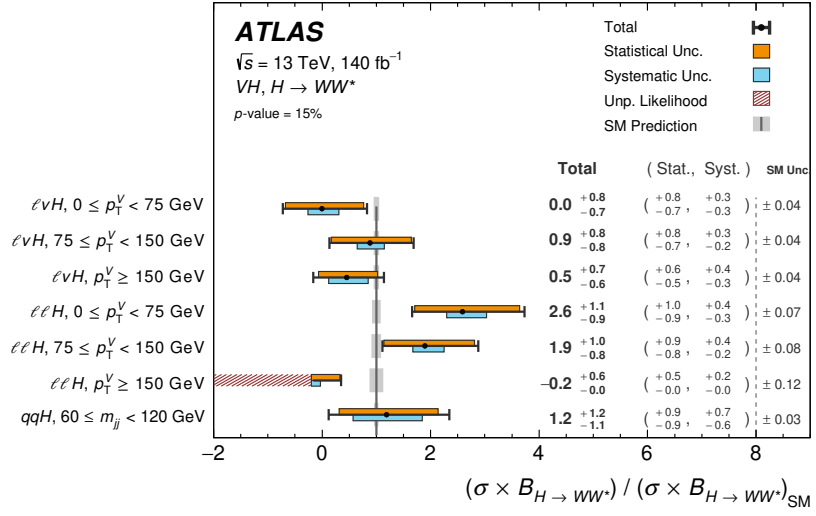
The fitted POIs and normalisation factors for the p_T^V and STXS schemes are summarised in Tables 11 and 12, respectively. The POIs are plotted in Figure 15.

Table 11: Observed fit results for the p_T^V scheme. A lower limit on the POI for the VH , $p_T^V \geq 250$ GeV category was set at -0.76 to prevent the likelihood from reaching an unphysical region with zero observed and zero expected events in any bin of the analysis. The label “LL” indicates that the interval reaches its minimum allowed value. “Stat. unc.” and “Syst. unc.” indicate the statistical and systematic components, respectively, of the total uncertainty in the corresponding POI. For the normalisation factors, only the total uncertainties are quoted. A 95% confidence level upper limit on the POI for the VH , $p_T^V \geq 250$ GeV category was computed and found to be 2.1. In the limit computation, the other POIs were left free to float.

Fit results for the p_T^V scheme					
Normalisation factors		$(\sigma_{\text{category}} \times \mathcal{B}_{H \rightarrow WW^*})/(\sigma_{\text{category}} \times \mathcal{B}_{H \rightarrow WW^*})_{\text{SM}}$			
Parameter	Fit result	Category	Fit result	Stat. unc.	Syst. unc.
Top	$0.9^{+0.3}_{-0.2}$	$VH, 0 \leq p_T^V < 75$ GeV	1.2 ± 0.5	$+0.5$ -0.4	$+0.2$ -0.1
Z+jets	$0.86^{+0.12}_{-0.11}$	$VH, 75 \leq p_T^V < 150$ GeV	1.2 ± 0.5	$+0.5$ -0.4	$+0.2$ -0.1
WW	$0.9^{+0.3}_{-0.2}$	$VH, 150 \leq p_T^V < 250$ GeV	$0.4^{+0.7}_{-0.6}$	$+0.6$ -0.5	± 0.3
WZ (SS 2ℓ)	$1.12^{+0.17}_{-0.15}$	$VH, p_T^V \geq 250$ GeV	$0.1^{+1.0}_{-0.9} \text{ (LL)}$	$+0.9$ -0.8	$+0.5$ -0.4
WZ 0-jet	1.00 ± 0.06				
WZ ≥ 1 -jets	$0.89^{+0.16}_{-0.15}$				
WWW	$2.0^{+0.6}_{-0.5}$				
ZZ	1.00 ± 0.03				



(a)



(b)

Figure 15: Observed fit results for (a) the p_T^V measurement and (b) the STXS Stage 1.2 measurement. The hatched band indicated with “Unp. Likelihood” shows the region of the parameter space where the likelihood becomes unphysical.

Table 12: Observed fit results for the STXS scheme. A lower limit on the POI for the $\ell\ell H, p_T^V \geq 150$ GeV category was set at -0.2 to prevent the likelihood from reaching an unphysical region with zero observed and zero expected events in any bin of the analysis. The label “LL” indicates that the interval reaches its minimum allowed value. “Stat. unc.” and “Syst. unc.” indicate the statistical and systematic components, respectively, of the total uncertainty in the corresponding POI. For the normalisation factors, only the total uncertainties are quoted. A 95% confidence level upper limit on the POI for the $\ell\ell H, p_T^V \geq 150$ GeV category was computed and found to be 1.6. In the limit computation, the other POIs were left free to float.

Fit results for the STXS scheme					
Normalisation factors		$(\sigma_{\text{STXS category}} \times \mathcal{B}_{H \rightarrow WW^*}) / (\sigma_{\text{STXS category}} \times \mathcal{B}_{H \rightarrow WW^*})_{\text{SM}}$			
Parameter	Fit result	STXS category	Fit result	Stat. unc.	Syst. unc.
Top	$0.9^{+0.3}_{-0.2}$	$\ell\nu H, 0 \leq p_T^V < 75$ GeV	$0.0^{+0.8}_{-0.7}$	$+0.8$ -0.7	± 0.3
Z+jets	$0.85^{+0.12}_{-0.11}$	$\ell\nu H, 75 \leq p_T^V < 150$ GeV	0.9 ± 0.8	$+0.8$ -0.7	$+0.3$ -0.2
WW	$0.9^{+0.3}_{-0.2}$	$\ell\nu H, p_T^V \geq 150$ GeV	$0.5^{+0.7}_{-0.6}$	$+0.6$ -0.5	$+0.4$ -0.3
WZ (SS 2ℓ)	$1.14^{+0.17}_{-0.15}$	$\ell\ell H, 0 \leq p_T^V < 75$ GeV	$2.6^{+1.1}_{-0.9}$	$+1.0$ -0.9	$+0.4$ -0.3
WZ 0-jet	1.00 ± 0.06	$\ell\ell H, 75 \leq p_T^V < 150$ GeV	$1.9^{+1.0}_{-0.8}$	$+0.9$ -0.8	$+0.4$ -0.2
WZ ≥ 1 -jets	$0.88^{+0.16}_{-0.15}$	$\ell\ell H, p_T^V \geq 150$ GeV	$-0.2^{+0.6}_{-0.0 \text{ (LL)}}$	$+0.5$ -0.0 (LL)	$+0.2$ -0.0 (LL)
WWW	$2.2^{+0.7}_{-0.6}$	$qqH, 60 \leq m_{jj} < 120$ GeV	$1.2^{+1.2}_{-1.1}$	± 0.9	$+0.7$ -0.6
ZZ	0.99 ± 0.03				

Due to deficits in data in several bins of the analysis — in particular the SS 2μ region — some of observed POIs are close to zero. Moreover, the expected total yield becomes negative for large negative values of the POIs; therefore, a constraint was imposed on the POI for the $VH, p_T^V \geq 250$ GeV category in the p_T^V scheme and on the POI for the $\ell\ell H, p_T^V \geq 150$ GeV category in the STXS scheme. In both the cases, the lower limit of the 68% confidence interval cannot be reached before the likelihood becomes ill-defined due to negative expected yields in some bins. The value at which this happens was specified in Tables 11 and 12. Given that this indicates a very low expected signal yield, a test of the validity of the asymptotic approximation was performed on such parameters. A small degree of over-coverage (71% with respect to 68%) of the confidence interval was observed for the POI for the $\ell\ell H, p_T^V \geq 150$ GeV category. The confidence interval is defined as in Ref. [141].

There are also some notable differences in the normalisation factors obtained from the total and differential cross-section measurements. For the opposite-sign 2ℓ channel, the top normalisation factor in the differential cross-section measurement is smaller than that obtained in the total cross-section measurement. The nuisance parameter which tunes the $t\bar{t}$ parton-shower modelling uncertainty is sensitive to the p_T^V modelling; therefore, it can be pulled differently in the two measurements. In the case of the differential cross-section measurement, the best-fit value of this nuisance parameter increases the $t\bar{t}$ yield in the $t\bar{t}$ CR. To compensate for such an increase, the top normalisation factor decreases. For the same-sign 2ℓ channel, the WZ normalisation factor in the differential cross-section measurement is larger than that obtained in the total cross-section measurement. The WZ normalisation factor is driven by the background-like bins of the signal regions in the same-sign 2ℓ channel. As those signal regions are split differently in the two measurement scenarios, the resulting WZ normalisation factors are also different.

The POIs were converted to fiducial cross-sections by multiplying the POIs by the cross-sections used to normalise the signal templates in each bin of the p_T^V and STXS schemes. The resulting values are shown in

Table 13.

Table 13: Observed cross-sections times the $H \rightarrow WW^*$ branching ratio for the p_T^V and STXS schemes. “Stat. unc.” and “Syst. unc.” indicate the statistical and systematic components, respectively, of the total uncertainty on the corresponding POI. “SM” indicates the SM expectation.

$\sigma \times \mathcal{B}_{H \rightarrow WW^*}$ [fb]									
p_T^V scheme ($ y_H < 2.5$)					STXS scheme				
p_T^V interval [GeV]	Value	Stat. unc.	Syst. unc.	SM	STXS category [p_T^V and m_{jj} in GeV]	Value	Stat. unc.	Syst. unc.	SM
VH ($0 \leq p_T^V < 75$)	270	$^{+110}_{-100}$	$^{+40}_{-30}$	220 ± 40	$\ell\nu H$ ($0 \leq p_T^V < 75$)	0	$^{+40}_{-30}$	± 10	46.3 ± 1.8
VH ($75 \leq p_T^V < 150$)	180	$^{+70}_{-60}$	$^{+30}_{-20}$	151 ± 34	$\ell\nu H$ ($75 \leq p_T^V < 150$)	26	$^{+22}_{-21}$	$^{+8}_{-7}$	28.9 ± 1.2
VH ($150 \leq p_T^V < 250$)	18	$^{+28}_{-26}$	$^{+17}_{-13}$	50 ± 15	$\ell\nu H$ ($p_T^V \geq 150$)	5	± 6	± 4	11.5 ± 0.5
VH ($p_T^V \geq 250$)	1	$^{+12}_{-11}$	$^{+7}_{-6}$	14 ± 4	$\ell\ell H$ ($0 \leq p_T^V < 75$)	62	$^{+25}_{-21}$	$^{+11}_{-7}$	24.1 ± 1.7
					$\ell\ell H$ ($75 \leq p_T^V < 150$)	35	$^{+17}_{-14}$	$^{+7}_{-4}$	18.7 ± 1.5
					$\ell\ell H$ ($p_T^V \geq 150$)	-2	$^{+5}_{-0}$	$^{+1}_{-0}$	8.7 ± 1.0
					qqH ($60 \leq m_{jj} < 120$)	110	$^{+90}_{-80}$	± 60	91.8 ± 3.3

The differential cross-section as a function of p_T^V is shown in Figure 16.

Finally, Tables 20 and 21 of Appendix C show the fractional contributions from statistical and systematic sources to the total uncertainties reported in p_T^V and STXS schemes, respectively. As for the total cross-section measurement, the differential results are dominated by statistical uncertainties in data.

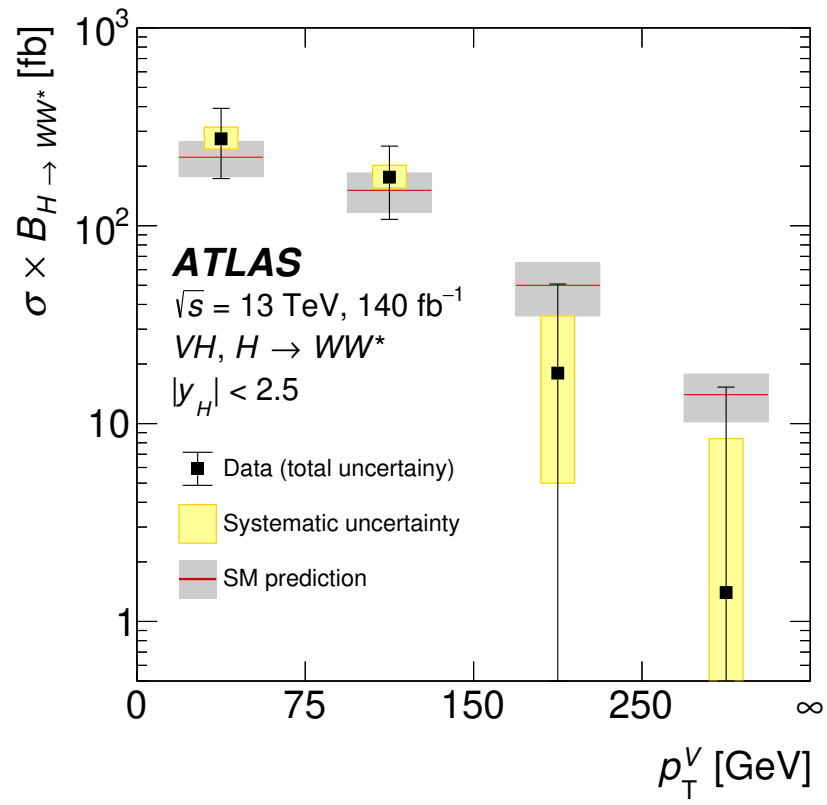


Figure 16: Differential VH production cross-section as a function of the p_T of the associated vector boson. The theoretical expectation is also shown.

10 Conclusions

A measurement of the total Higgs boson production cross-sections via associated WH and ZH production using $H \rightarrow WW^* \rightarrow \ell\nu\ell\nu$ and $H \rightarrow WW^* \rightarrow \ell\nu jj$ decays is presented. Results for combined WH and ZH production are also presented. The analysis uses proton–proton events delivered by the Large Hadron Collider at a centre-of-mass energy of 13 TeV and recorded by the ATLAS detector between 2015 and 2018. The data correspond to an integrated luminosity of 140 fb^{-1} . The VH signal strength is measured to be $0.92^{+0.21}_{-0.20} \text{ (stat.)}^{+0.13}_{-0.12} \text{ (syst.)}$, corresponding to a 4.5σ significance over the background-only hypothesis. The products of the $H \rightarrow WW^*$ branching fraction times the WH and ZH cross-sections are measured to be $0.14^{+0.08}_{-0.07} \text{ (stat.)} \pm 0.05 \text{ (syst.) pb}$ and $0.31^{+0.09}_{-0.08} \text{ (stat.)} \pm 0.03 \text{ (syst.) pb}$, respectively, in agreement with the Standard Model predictions. Differential cross-sections have also been measured, $\sigma_{VH} \times \mathcal{B}_{H \rightarrow WW^*}$ as a function of the p_T of the associated vector boson and Simplified Template Cross-Sections for VH and $EW \text{ } qqH$ production. The results obtained are in agreement with their Standard Model expectations.

Acknowledgements

We thank CERN for the very successful operation of the LHC and its injectors, as well as the support staff at CERN and at our institutions worldwide without whom ATLAS could not be operated efficiently.

The crucial computing support from all WLCG partners is acknowledged gratefully, in particular from CERN, the ATLAS Tier-1 facilities at TRIUMF/SFU (Canada), NDGF (Denmark, Norway, Sweden), CC-IN2P3 (France), KIT/GridKA (Germany), INFN-CNAF (Italy), NL-T1 (Netherlands), PIC (Spain), RAL (UK) and BNL (USA), the Tier-2 facilities worldwide and large non-WLCG resource providers. Major contributors of computing resources are listed in Ref. [142].

We gratefully acknowledge the support of ANPCyT, Argentina; YerPhI, Armenia; ARC, Australia; BMWFW and FWF, Austria; ANAS, Azerbaijan; CNPq and FAPESP, Brazil; NSERC, NRC and CFI, Canada; CERN; ANID, Chile; CAS, MOST and NSFC, China; Minciencias, Colombia; MEYS CR, Czech Republic; DNRF and DNSRC, Denmark; IN2P3-CNRS and CEA-DRF/IRFU, France; SRNSFG, Georgia; BMBF, HGF and MPG, Germany; GSRI, Greece; RGC and Hong Kong SAR, China; ISF and Benoziyo Center, Israel; INFN, Italy; MEXT and JSPS, Japan; CNRST, Morocco; NWO, Netherlands; RCN, Norway; MNiSW, Poland; FCT, Portugal; MNE/IFA, Romania; MSTDI, Serbia; MSSR, Slovakia; ARIS and MVZI, Slovenia; DSI/NRF, South Africa; MICIU/AEI, Spain; SRC and Wallenberg Foundation, Sweden; SERI, SNSF and Cantons of Bern and Geneva, Switzerland; NSTC, Taipei; TENMAK, Türkiye; STFC/UKRI, United Kingdom; DOE and NSF, United States of America.

Individual groups and members have received support from BCKDF, CANARIE, CRC and DRAC, Canada; CERN-CZ, FORTE and PRIMUS, Czech Republic; COST, ERC, ERDF, Horizon 2020, ICSC-NextGenerationEU and Marie Skłodowska-Curie Actions, European Union; Investissements d’Avenir Labex, Investissements d’Avenir Idex and ANR, France; DFG and AvH Foundation, Germany; Herakleitos, Thales and Aristeia programmes co-financed by EU-ESF and the Greek NSRF, Greece; BSF-NSF and MINERVA, Israel; NCN and NAWA, Poland; La Caixa Banking Foundation, CERCA Programme Generalitat de Catalunya and PROMETEO and GenT Programmes Generalitat Valenciana, Spain; Göran Gustafssons Stiftelse, Sweden; The Royal Society and Leverhulme Trust, United Kingdom.

In addition, individual members wish to acknowledge support from Armenia: Yerevan Physics Institute (FAPERJ); CERN: European Organization for Nuclear Research (CERN PJAS); Chile: Agencia

Nacional de Investigación y Desarrollo (FONDECYT 1230812, FONDECYT 1230987, FONDECYT 1240864); China: Chinese Ministry of Science and Technology (MOST-2023YFA1605700, MOST-2023YFA1609300), National Natural Science Foundation of China (NSFC - 12175119, NSFC 12275265, NSFC-12075060); Czech Republic: Czech Science Foundation (GACR - 24-11373S), Ministry of Education Youth and Sports (ERC-CZ-LL2327, FORTE CZ.02.01.01/00/22_008/0004632), PRIMUS Research Programme (PRIMUS/21/SCI/017); EU: H2020 European Research Council (ERC - 101002463); European Union: European Research Council (ERC - 948254, ERC 101089007), Horizon 2020 Framework Programme (MUCCA - CHIST-ERA-19-XAI-00), European Union, Future Artificial Intelligence Research (FAIR-NextGenerationEU PE00000013), Italian Center for High Performance Computing, Big Data and Quantum Computing (ICSC, NextGenerationEU); France: Agence Nationale de la Recherche (ANR-20-CE31-0013, ANR-21-CE31-0013, ANR-21-CE31-0022, ANR-22-EDIR-0002), Investissements d'Avenir Labex (ANR-11-LABX-0012); Germany: Baden-Württemberg Stiftung (BW Stiftung-Postdoc Eliteprogramme), Deutsche Forschungsgemeinschaft (DFG - 469666862, DFG - CR 312/5-2); Italy: Istituto Nazionale di Fisica Nucleare (ICSC, NextGenerationEU), Ministero dell'Università e della Ricerca (NextGenEU PRIN20223N7F8K M4C2.1.1); Japan: Japan Society for the Promotion of Science (JSPS KAKENHI JP22H01227, JSPS KAKENHI JP22H04944, JSPS KAKENHI JP22KK0227, JSPS KAKENHI JP23KK0245); Netherlands: Netherlands Organisation for Scientific Research (NWO Veni 2020 - VI.Veni.202.179); Norway: Research Council of Norway (RCN-314472); Poland: Ministry of Science and Higher Education (IDUB AGH, POB8, D4 no 9722), Polish National Agency for Academic Exchange (PPN/PPO/2020/1/00002/U/00001), Polish National Science Centre (NCN 2021/42/E/ST2/00350, NCN OPUS nr 2022/47/B/ST2/03059, NCN UMO-2019/34/E/ST2/00393, NCN & H2020 MSCA 945339, UMO-2020/37/B/ST2/01043, UMO-2021/40/C/ST2/00187, UMO-2022/47/O/ST2/00148, UMO-2023/49/B/ST2/04085, UMO-2023/51/B/ST2/00920); Slovenia: Slovenian Research Agency (ARIS grant J1-3010); Spain: Generalitat Valenciana (Artemisa, FEDER, IDIFEDER/2018/048), Ministry of Science and Innovation (MCIN & NextGenEU PCI2022-135018-2, MICIN & FEDER PID2021-125273NB, RYC2019-028510-I, RYC2020-030254-I, RYC2021-031273-I, RYC2022-038164-I); Sweden: Carl Trygger Foundation (Carl Trygger Foundation CTS 22:2312), Swedish Research Council (Swedish Research Council 2023-04654, VR 2018-00482, VR 2021-03651, VR 2022-03845, VR 2022-04683, VR 2023-03403), Knut and Alice Wallenberg Foundation (KAW 2018.0458, KAW 2019.0447, KAW 2022.0358); Switzerland: Swiss National Science Foundation (SNSF - PCEFP2_194658); United Kingdom: Leverhulme Trust (Leverhulme Trust RPG-2020-004), Royal Society (NIF-R1-231091); United States of America: U.S. Department of Energy (ECA DE-AC02-76SF00515), Neubauer Family Foundation.

Appendix

A Input variables for multivariate discriminants

This appendix describes the input variables for each of the multivariate discriminants utilised by this measurement.

Opposite-sign 2ℓ channel: The input variables for the ANN utilised by the opposite-sign 2ℓ channel — see Section 6.1 — are shown in Table 14. The transverse mass of the $H \rightarrow WW^*$ system, m_T :

$$m_T = \sqrt{2p_T^{\ell\ell} E_T^{\text{miss}} (1 - \cos \Delta\phi_{\ell\ell, \text{miss}})}, \quad (4)$$

where $p_T^{\ell\ell}$ is the transverse momentum of the dilepton system and $\Delta\phi_{\ell\ell, \text{miss}}$ is the azimuthal separation between the dilepton system and the E_T^{miss} .

Table 14: Summary of input variables for the ANN in the opposite-sign 2ℓ channel.

Variable(s)	Description
$p_T^{\ell_0}, p_T^{\ell_1}$	Leading and subleading lepton transverse momentum
$m_{\ell\ell}$	Dilepton invariant mass
$\Delta\phi_{\ell\ell}$	Dilepton azimuthal separation
$\Delta Y_{\ell\ell}$	Dilepton rapidity separation
m_T	Transverse mass (Eq. 4)
$p_T^{j_0}, p_T^{j_1}$	Leading and subleading jet transverse momentum
m_{jj}	Dijet invariant mass
$\Delta\phi_{jj}$	Dijet azimuthal separation
Δy_{jj}	Dijet rapidity separation
$m_{\ell_0 j_0}, m_{\ell_0 j_1}, m_{\ell_1 j_0}, m_{\ell_1 j_1}$	All lepton-jet invariant mass combinations
$m_{\tau\tau}$	Invariant mass of the τ -lepton pair using the collinear approximation [143], assuming the electrons and muons result from τ -lepton decays
E_T^{miss}	Missing transverse momentum
S_{miss}	Object-based E_T^{miss} significance
H_T	Transverse momentum sum of all hard objects

3ℓ channel: The input variables for the ANN utilised by the 3ℓ Z-dominated channel — see Section 6.3 — are shown in Table 15. The transverse mass (Eq. 4) of the W boson, m_T^W . It is constructed from the E_T^{miss} and the lepton not belonging to the SFOS pair with an invariant mass closest to the mass of the Z boson, either ℓ_1 or ℓ_2 .

Table 15: Summary of input variables for the ANN in the 3ℓ Z-dominated channel.

Variable(s)	Description
$p_T^{\ell_0}$	Transverse momentum of ℓ_0
$\left \sum_{i=0}^2 \vec{p}_T^{\ell_i} \right $	Magnitude of the vectorial sum of the lepton transverse momenta
$\Delta\eta_{\ell_0\ell_1}, \Delta\eta_{\ell_1\ell_2}$	Pseudorapidity separation between ℓ_0 and ℓ_1 and between ℓ_1 and ℓ_2
$\Delta\phi_{\ell_0\ell_2}$	Azimuthal separation between ℓ_0 and ℓ_2
$\Delta R_{\ell_0\ell_1}, \Delta R_{\ell_0\ell_2}$	Angular separation between ℓ_0 and ℓ_1 and between ℓ_0 and ℓ_2
$m_{\ell_0\ell_1}, m_{\ell_0\ell_2}, m_{\ell_1\ell_2}$	Dilepton invariant mass for each combination of leptons
E_T^{miss}	Missing transverse momentum
$\Delta\phi_{\ell_0,\text{miss}}, \Delta\phi_{\ell_1,\text{miss}}, \Delta\phi_{\ell_2,\text{miss}}$	Azimuthal separation between each lepton and the E_T^{miss}
m_T^W	Transverse mass of the W boson (Eq. 4)

The input variables for the ANN utilised by the 3ℓ Z-depleted channel are shown in Table 16. An input deserving additional explanation is the compatibility of the event with the WZ hypothesis, F_α . Given the reconstructed charged lepton momenta and the \vec{p}_T^{miss} , the event kinematics can be calculated under the WZ with $Z \rightarrow \tau\tau$ hypothesis and using the collinear approximation for the τ -lepton decays with one remaining unknown — for example, the ratio of one τ -lepton's energy to the energy of the lepton from the same τ -lepton's decay. This unknown is varied, and the number of physical kinematic solutions is taken as a measure of the compatibility with the WZ hypothesis.

Table 16: Summary of input variables for the ANN in the 3ℓ Z-depleted channel.

Variable(s)	Description
$p_T^{\ell_0}, p_T^{\ell_1}, p_T^{\ell_2}$	Transverse momentum for each lepton
$\Delta\eta_{\ell_0\ell_1}, \Delta\eta_{\ell_0\ell_2}, \Delta\eta_{\ell_1\ell_2}$	Dilepton pseudorapidity separation for each combination of leptons
$\Delta R_{\ell_0\ell_1}, \Delta R_{\ell_0\ell_2}, \Delta R_{\ell_1\ell_2}$	Dilepton angular separation for each combination of leptons
$m_{\ell_0\ell_1}, m_{\ell_0\ell_2}, m_{\ell_1\ell_2}$	Dilepton invariant mass for each combination of leptons
$m_T^{\ell_0\ell_1}, m_T^{\ell_0\ell_2}, m_T^{\ell_1\ell_2}$	Dilepton transverse mass for each combination of leptons
$\left \sum_{i=0}^2 \vec{p}_T^{\ell_i} \right $	Magnitude of the vectorial sum of the lepton transverse momenta
$m_{\ell\ell\ell}$	Trilepton invariant mass
n_{jets}	Number of jets
$n_{b\text{-jets}}$	Number of b -tagged jets
$p_T^{j_0}$	Transverse momentum of the leading jet
E_T^{miss}	Missing transverse momentum
$\Delta\phi_{\ell_0,\text{miss}}, \Delta\phi_{\ell_1,\text{miss}}, \Delta\phi_{\ell_2,\text{miss}}$	Azimuthal separation between each lepton and the E_T^{miss}
$S_{\text{miss}} / E_T^{\text{miss}}$	Ratio of the E_T^{miss} significance to the E_T^{miss}
F_α	Compatibility of the event with the WZ hypothesis

4 ℓ channel: The input variables for the BDTs utilised by the 4 ℓ channel — see Section 6.4 — are shown in Table 17. The azimuthal separation between the leptons from the Higgs boson candidate in the frame where the Higgs boson p_T is zero is denoted by $\Delta\phi_{\ell_0\ell_1}^{\text{boost}}$. The Higgs boson transverse momentum is approximated with $\vec{p}_T^H \approx -\vec{p}_T^Z$ or $\vec{p}_T^H \approx -\vec{p}_T^Z - \sum \vec{p}_T^{\text{jet}}$, if at least one jet is in the event.

Table 17: Summary of input variables for the BDTs in the 4 ℓ channel.

Variable(s)	Description
$p_T^{\ell_0}, p_T^{\ell_1}, p_T^{\ell_2}, p_T^{\ell_3}$	Transverse momentum for each lepton
$m_{\ell_0\ell_1}$	Invariant mass of the Higgs boson candidate
$m_{\ell_2\ell_3}$	Invariant mass of the Z candidate
$p_T^{4\ell}$	Transverse momentum of the 4-lepton system
$m_{4\ell}$	Invariant mass of the 4-lepton system
$m_{\tau\tau}$	Invariant mass of the τ -lepton pair using the collinear approximation [143], assuming the electrons and muons result from τ -lepton decays
n_{jets}	Number of jets
E_T^{miss}	Missing transverse momentum
$\Delta\phi_{\ell_0\ell_1,\text{miss}}$	Azimuthal separation between the dilepton system composed of ℓ_0 and ℓ_1 and the E_T^{miss}
$\Delta\phi_{\ell_0\ell_1}^{\text{boost}}$	Azimuthal separation between ℓ_0 and ℓ_1 in the Higgs boson candidate's frame

STXS categorisation: Table 18 shows the input variables for the ANN regressing the W boson's p_T . This ANN is utilised by the 3 ℓ channels for their differential measurement — see Section 6.5.

Table 18: Summary of input variables for the regression ANN in the 3 ℓ channel.

Variable(s)	Description
$p_T^{\ell_0}, p_T^{\ell_1}, p_T^{\ell_2}$	Transverse momentum for each lepton
$\Delta R_{\ell_0\ell_1}, \Delta R_{\ell_0\ell_2}, \Delta R_{\ell_1\ell_2}$	Dilepton angular separation for each combination of leptons
$m_{\ell_0\ell_1}, m_{\ell_0\ell_2}, m_{\ell_1\ell_2}$	Dilepton invariant mass for each combination of leptons
$m_T^{\ell_0\ell_1}, m_T^{\ell_0\ell_2}, m_T^{\ell_1\ell_2}$	Dilepton transverse mass for each combination of leptons
$\sum_{i=0}^2 p_T^{\ell_i}$	Scalar sum of the lepton transverse momenta
E_T^{miss}	Missing transverse momentum
$\Delta\phi_{\ell_0,\text{miss}}, \Delta\phi_{\ell_1,\text{miss}}, \Delta\phi_{\ell_2,\text{miss}}$	Azimuthal separation between each lepton and the E_T^{miss}

B Additional plots for the STXS categorisation

This appendix includes additional plots supporting the STXS categorisation scheme described in Section 6.5.

Figure 17 shows the Stage 1.2 STXS categorisation scheme for VH production. Figure 18 shows the correlation between p_T^V and the proxy used for its reconstruction for several channels.

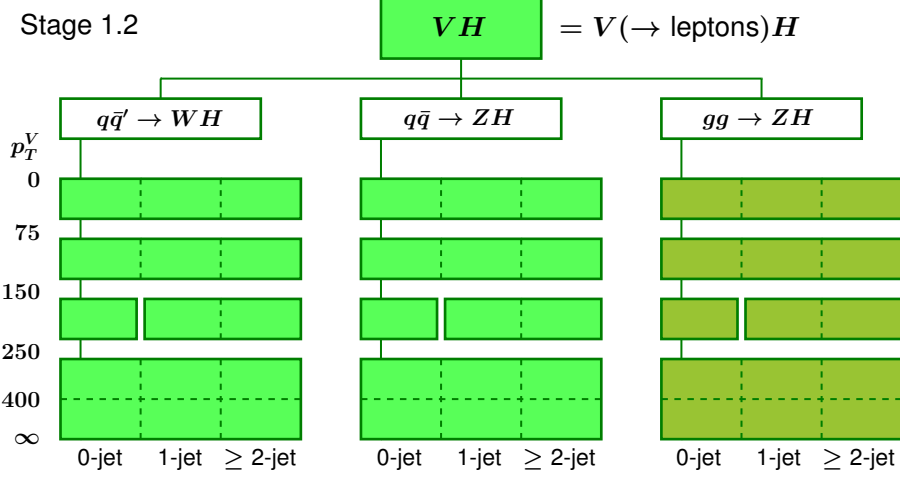


Figure 17: The Stage 1.2 STXS categorisation scheme for VH production [22].

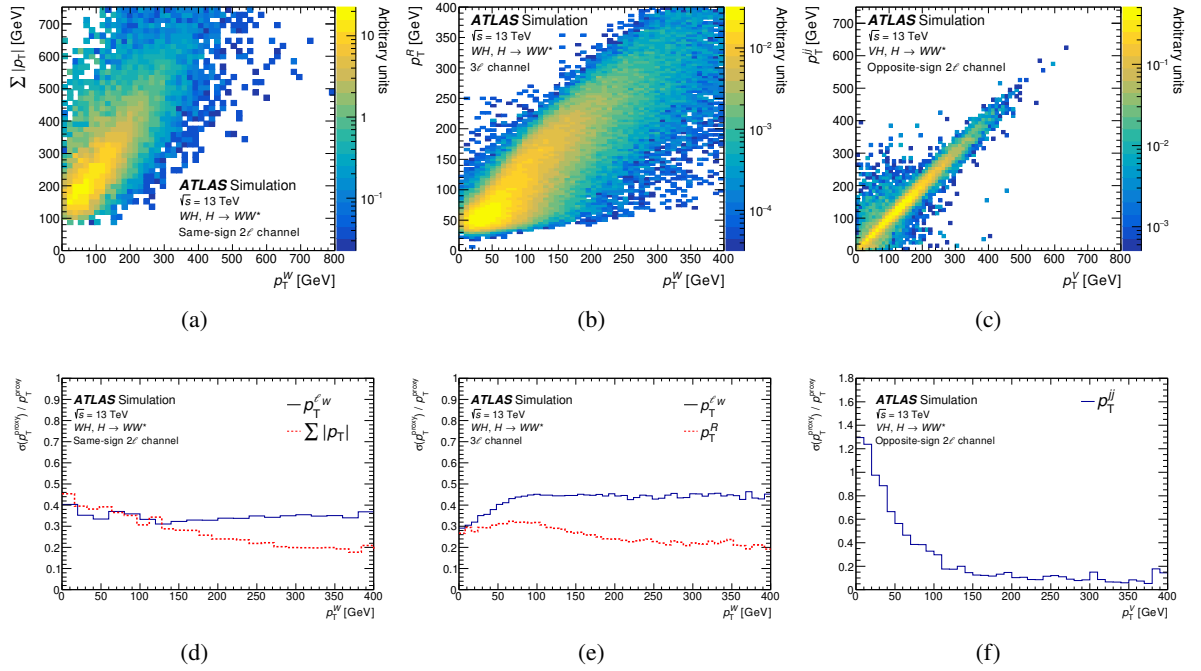


Figure 18: Performance of the p_T^V proxies for several channels: (a), (b), (c) the correlation between the p_T of the associated boson and the proxy and (d), (e), (f) the fractional resolution of the proxy as a function of p_T^V . Shown are (a), (d) the $\Sigma |p_T|$ of all objects in the SS2e channel, (b), (e) the regression neural network output, p_T^R , in the 3ℓ Z-dominated channel, and (c), (f) the dijet p_T , p_T^{jj} , in the opposite-sign 2ℓ channel. The p_T^R resolution is compared with that obtained using as a proxy the p_T of the lepton identified as that from the W boson decay, while the $\Sigma |p_T|$ resolution is compared with that obtained using as a proxy the highest p_T lepton.

C Breakdown of uncertainties contributing to observed results

This appendix includes tables which show the breakdown of uncertainties contributing to the observed results presented in Section 9.2.

Table 19 shows the relative impact of the different sources of uncertainty in the observed values of the total cross-sections, presented in Section 9.2.1.

Tables 20 and 21 show the fractional contributions from statistical and systematic sources to the total uncertainties in the observed values of the differential cross-sections, presented in Section 9.2.2.

Table 19: Breakdown of the average contributions to the total uncertainties (in percentage) in the observed values of the cross-sections for the combined 1-POI ($\sigma_{VH} \times \mathcal{B}_{H \rightarrow WW^*}$) and 2-POI ($\sigma_{WH} \times \mathcal{B}_{H \rightarrow WW^*}$ and $\sigma_{ZH} \times \mathcal{B}_{H \rightarrow WW^*}$) fits. Indentation is used to denote subcategories. The quadrature sum of the individual sources may differ from the total uncertainty due to correlations.

Source	$\frac{\Delta(\sigma_{VH} \times \mathcal{B}_{H \rightarrow WW^*})}{\sigma_{VH} \times \mathcal{B}_{H \rightarrow WW^*}} [\%]$	$\frac{\Delta(\sigma_{WH} \times \mathcal{B}_{H \rightarrow WW^*})}{\sigma_{WH} \times \mathcal{B}_{H \rightarrow WW^*}} [\%]$	$\frac{\Delta(\sigma_{ZH} \times \mathcal{B}_{H \rightarrow WW^*})}{\sigma_{ZH} \times \mathcal{B}_{H \rightarrow WW^*}} [\%]$
Statistical uncertainties in data	22	54	29
Statistical uncertainties in SR data	20	46	28
Statistical uncertainties in CR data	10	29	6.3
Systematic uncertainties	13	35	10
Statistical uncertainties in simulation	6.2	13	5.9
Experimental systematic uncertainties	5.4	12	5.7
Electrons	1.1	1.6	1.6
Muons	2.7	3.0	4.1
Jet energy scale	1.0	3.1	0.5
Jet energy resolution	0.5	2.4	0.6
Flavour tagging	1.0	1.5	0.8
Missing transverse momentum	0.6	0.2	0.9
Pile-up	1.0	1.3	0.8
Luminosity	1.1	1.2	1.1
Mis-identified leptons	3.7	10	2.8
Charge-flip electrons	1.7	5.0	0.0
Theoretical uncertainties	6.9	20	4.2
WH	2.1	2.3	0.1
ZH	0.5	0.3	2.4
Other H	1.2	2.4	0.9
WW	1.2	3.7	0.2
WZ 0-jet	3.2	11	0.2
WZ ≥ 1 -jets	3.2	9.7	0.4
ZZ	1.2	2.1	0.8
VVV	2.7	12	1.0
Top	2.8	5.0	2.4
Z +jets	1.6	2.9	1.5
RNN shape uncertainty for WZ	7.5	23	0.7
Total	26	64	30

Table 20: Breakdown of the average contributions to the total uncertainties in the differential cross-sections measured in the p_T^V scheme. The uncertainties of a single source, Δ_i , are expressed in percentage of the total uncertainty, Δ . Indentation is used to denote subcategories. Also shown is the total relative (non-fractional) uncertainty in the cross-section, $\Delta(\sigma \times \mathcal{B}_{H \rightarrow WW^*})/(\sigma \times \mathcal{B}_{H \rightarrow WW^*})$, in percent. The quadrature sum of the individual sources may differ from the total uncertainty due to correlations.

Source	$\frac{\Delta_i(\sigma_{VH}(X \leq p_T^V < Y) \times \mathcal{B}_{H \rightarrow WW^*})}{\Delta(\sigma_{VH}(X \leq p_T^V < Y) \times \mathcal{B}_{H \rightarrow WW^*})} [\%], [X, Y): X \leq p_T^V < Y \text{ GeV}$			
	VH [0, 75)	VH [75, 150)	VH [150, 250)	VH [250, ∞)
Statistical uncertainties in data	95	95	87	81
Statistical uncertainties in SR data	92	93	87	81
Statistical uncertainties in CR data	22	18	5.9	5.7
Systematic uncertainties	33	32	49	44
Statistical uncertainties in simulation	20	22	24	33
Experimental systematic uncertainties	17	13	13	10
Electrons	3.8	1.6	1.5	1.2
Muons	6.6	3.8	6.6	4.9
Jet energy scale	4.0	2.9	6.5	5.6
Jet energy resolution	7.1	5.7	7.4	5.1
Flavour tagging	1.3	1.4	1.7	1.6
Missing transverse momentum	5.1	1.6	1.2	0.9
Pile-up	4.4	1.2	0.8	0.6
Luminosity	3.1	2.5	1.3	1.1
Mis-identified leptons	9.2	9.0	4.4	3.7
Charge-flip electrons	2.1	2.2	4.0	3.1
Theoretical uncertainties	16	16	21	11
WH	0.6	0.7	1.1	0.6
ZH	0.6	0.7	1.2	0.6
STXS bin migration	2.1	4.2	3.2	1.7
Other H	0.6	1.3	7.7	7.3
WW	1.2	4.4	12.1	2.2
WZ 0-jet	2.5	5.3	5.0	4.0
WZ ≥ 1 -jets	2.2	3.1	3.6	2.5
ZZ	14	11	6.3	2.0
VVV	4.5	2.8	4.5	2.7
Top	2.3	8.4	4.8	5.0
Z+jets	0.6	3.0	1.8	2.9
RNN shape uncertainty for WZ	1.1	8.0	36	7.7
Total relative uncertainty (non-fractional)	40	41	170	1000

Table 21: Breakdown of the average contributions to the total uncertainties in the differential cross-sections measured in the STXS scheme. The uncertainties of a single source, Δ_i , are expressed in percentage of the total uncertainty, Δ . Indentation is used to denote subcategories. Also shown is the total relative (non-fractional) uncertainty in the cross-section, $\Delta(\sigma \times \mathcal{B}_{H \rightarrow WW^*})/(\sigma \times \mathcal{B}_{H \rightarrow WW^*})$, in percent. The quadrature sum of the individual sources may differ from the total uncertainty due to correlations.

Source	$\frac{\Delta_i (\sigma_{\text{STXS category}} \times \mathcal{B}_{H \rightarrow WW^*})}{\Delta (\sigma_{\text{STXS category}} \times \mathcal{B}_{H \rightarrow WW^*})} [\%], [X, Y]: X \leq (p_T^V \text{ or } m_{jj}) < Y \text{ GeV}$						
	$\ell\nu H [0, 75)$	$\ell\nu H [75, 150)$	$\ell\nu H [150, \infty)$	$\ell\ell H [0, 75)$	$\ell\ell H [75, 150)$	$\ell\ell H [150, \infty)$	$qqH [60, 120)$
Statistical uncertainties in data	93	95	83	94	95	96	82
Statistical uncertainties in SR data	90	94	83	92	94	95	82
Statistical uncertainties in CR data	23	15	8.1	14	12	7.6	5.7
Systematic uncertainties	36	32	56	35	32	30	57
Statistical uncertainties in simulation	22	24	18	31	28	20	28
Experimental systematic uncertainties	23	18	11	8.7	8.3	20	23
Electrons	2.6	1.2	1.6	3.6	2.0	0.9	2.1
Muons	2.6	1.7	2.0	3.1	2.5	19	2.4
Jet energy scale	4.8	3.7	2.4	1.7	2.2	1.3	20
Jet energy resolution	11	9.4	2.2	1.9	1.0	0.8	10
Flavour tagging	0.9	1.5	2.3	0.8	1.3	1.2	3.5
Missing transverse momentum	3.4	1.9	0.9	4.0	1.7	1.2	1.1
Pile-up	3.2	1.1	0.4	1.4	1.1	0.3	0.8
Luminosity	1.2	0.9	1.3	2.3	2.3	0.9	2.0
Mis-identified leptons	18	13	7.3	4.2	6.2	4.2	7.1
Charge-flip electrons	3.8	4.2	6.3	0.9	0.8	0.1	1.3
Theoretical uncertainties	12	12	19	15	13	111	44
WH	0.5	0.8	0.7	0.9	0.8	<0.1	0.7
ZH	0.3	0.3	0.5	1.0	0.7	0.3	0.7
STXS bin migration	1.6	2.5	2.0	2.5	3.6	4.7	1.0
Other H	0.3	0.3	0.5	0.9	0.8	<0.1	14.2
WW	0.6	3.7	0.7	0.9	0.8	0.1	19
WZ 0-jet	5.7	6.8	11	1.1	0.9	0.4	0.7
$WZ \geq 1$ -jets	3.8	6.2	9.5	1.0	0.8	0.5	1.9
ZZ	3.9	1.8	2.7	14	12	9.6	0.6
VVV	8.4	2.2	10	1.8	0.8	1.1	0.6
Top	2.1	1.3	0.7	1.0	0.8	0.5	32
Z +jets	0.7	0.9	0.5	0.9	0.8	<0.1	4.5
RNN shape uncertainty for WZ	2.2	6.9	49	0.9	0.9	0.9	0.6
Total relative uncertainty (non-fractional)	19 000	88	140	40	47	140	93

References

- [1] T. D. Lee, *A Theory of Spontaneous T Violation*, [Phys. Rev. D **8** \(1973\) 1226](#), ed. by G. Feinberg.
- [2] G. C. Branco et al., *Theory and phenomenology of two-Higgs-doublet models*, [Phys. Rept. **516** \(2012\) 1](#), arXiv: [1106.0034 \[hep-ph\]](#).
- [3] J. de Blas, J. M. Lizana and M. Pérez-Victoria, *Combining searches of Z' and W' bosons*, [JHEP **01** \(2013\) 166](#), arXiv: [1211.2229 \[hep-ph\]](#).
- [4] D. Pappadopulo, A. Thamm, R. Torre and A. Wulzer, *Heavy Vector Triplets: Bridging Theory and Data*, [JHEP **09** \(2014\) 060](#), arXiv: [1402.4431 \[hep-ph\]](#).
- [5] ATLAS Collaboration, *The ATLAS Experiment at the CERN Large Hadron Collider*, [JINST **3** \(2008\) S08003](#).
- [6] L. Evans and P. Bryant, *LHC Machine*, [JINST **3** \(2008\) S08001](#).
- [7] ATLAS Collaboration, *Study of $(W/Z)H$ production and Higgs boson couplings using $H \rightarrow WW^*$ decays with the ATLAS detector*, [JHEP **08** \(2015\) 137](#), arXiv: [1506.06641 \[hep-ex\]](#).
- [8] CMS Collaboration, *Measurement of Higgs boson production and properties in the WW decay channel with leptonic final states*, [JHEP **01** \(2014\) 096](#), arXiv: [1312.1129 \[hep-ex\]](#).
- [9] CMS Collaboration, *Measurements of the Higgs boson production cross section and couplings in the W boson pair decay channel in proton–proton collisions at $\sqrt{s} = 13$ TeV*, [Eur. Phys. J. C **83** \(2023\) 667](#), arXiv: [2206.09466 \[hep-ex\]](#).
- [10] ATLAS Collaboration, *Measurement of the production cross section for a Higgs boson in association with a vector boson in the $H \rightarrow WW^* \rightarrow \ell\nu\ell\nu$ channel in pp collisions at $\sqrt{s} = 13$ TeV with the ATLAS detector*, [Phys. Lett. B **798** \(2019\) 134949](#), arXiv: [1903.10052 \[hep-ex\]](#).
- [11] ATLAS Collaboration, *Measurements of Higgs boson production by gluon–gluon fusion and vector-boson fusion using $H \rightarrow WW^* \rightarrow e\nu\mu\nu$ decays in pp collisions at $\sqrt{s} = 13$ TeV with the ATLAS detector*, [Phys. Rev. D **108** \(2023\) 032005](#), arXiv: [2207.00338 \[hep-ex\]](#).
- [12] ATLAS Collaboration, *Higgs boson production cross-section measurements and their EFT interpretation in the 4ℓ decay channel at $\sqrt{s} = 13$ TeV with the ATLAS detector*, [Eur. Phys. J. C **80** \(2020\) 957](#), arXiv: [2004.03447 \[hep-ex\]](#),
Erratum: [Eur. Phys. J. C **81** \(2021\) 29](#), Erratum: [Eur. Phys. J. C **81** \(2021\) 398](#).
- [13] CMS Collaboration, *Measurements of production cross sections of the Higgs boson in the four-lepton final state in proton–proton collisions at $\sqrt{s} = 13$ TeV*, [Eur. Phys. J. C **81** \(2021\) 488](#), arXiv: [2103.04956 \[hep-ex\]](#).
- [14] ATLAS Collaboration, *Measurement of the properties of Higgs boson production at $\sqrt{s} = 13$ TeV in the $H \rightarrow \gamma\gamma$ channel using 139fb^{-1} of pp collision data with the ATLAS experiment*, [JHEP **07** \(2023\) 088](#), arXiv: [2207.00348 \[hep-ex\]](#).
- [15] CMS Collaboration, *Measurements of Higgs boson production cross sections and couplings in the diphoton decay channel at $\sqrt{s} = 13$ TeV*, [JHEP **07** \(2021\) 027](#), arXiv: [2103.06956 \[hep-ex\]](#).

- [16] ATLAS Collaboration, *Measurements of WH and ZH production in the $H \rightarrow b\bar{b}$ decay channel in pp collisions at 13 TeV with the ATLAS detector*, *Eur. Phys. J. C* **81** (2021) 178, arXiv: [2007.02873 \[hep-ex\]](#).
- [17] CMS Collaboration, *Observation of Higgs Boson Decay to Bottom Quarks*, *Phys. Rev. Lett.* **121** (2018) 121801, arXiv: [1808.08242 \[hep-ex\]](#).
- [18] ATLAS Collaboration, *Measurements of Higgs boson production cross-sections in the $H \rightarrow \tau^+\tau^-$ decay channel in pp collisions at $\sqrt{s} = 13$ TeV with the ATLAS detector*, *JHEP* **08** (2022) 175, arXiv: [2201.08269 \[hep-ex\]](#).
- [19] CMS Collaboration, *Measurements of Higgs boson production in the decay channel with a pair of τ leptons in proton–proton collisions at $\sqrt{s} = 13$ TeV*, *Eur. Phys. J. C* **83** (2023) 562, arXiv: [2204.12957 \[hep-ex\]](#).
- [20] J. R. Andersen et al., ‘Les Houches 2015: Physics at TeV Colliders Standard Model Working Group Report’, *9th Les Houches Workshop on Physics at TeV Colliders*, 2016, arXiv: [1605.04692 \[hep-ph\]](#).
- [21] D. de Florian et al., *Handbook of LHC Higgs Cross Sections: 4. Deciphering the Nature of the Higgs Sector*, (2017), arXiv: [1610.07922 \[hep-ph\]](#).
- [22] N. Berger et al., *Simplified Template Cross Sections - Stage 1.1*, (2019), arXiv: [1906.02754 \[hep-ph\]](#).
- [23] F. Chollet et al., *Keras*, 2015, URL: <https://keras.io>.
- [24] M. Abadi et al., *TensorFlow: A system for large-scale machine learning*, (2016), arXiv: [1605.08695 \[cs.DC\]](#).
- [25] A. Hoecker et al., *TMVA - Toolkit for Multivariate Data Analysis*, 2009, arXiv: [physics/0703039 \[physics.data-an\]](#).
- [26] ATLAS Collaboration, *ATLAS Insertable B-Layer: Technical Design Report*, ATLAS-TDR-19; CERN-LHCC-2010-013, 2010, URL: <https://cds.cern.ch/record/1291633>, Addendum: ATLAS-TDR-19-ADD-1; CERN-LHCC-2012-009, 2012, URL: <https://cds.cern.ch/record/1451888>.
- [27] B. Abbott et al., *Production and integration of the ATLAS Insertable B-Layer*, *JINST* **13** (2018) T05008, arXiv: [1803.00844 \[physics.ins-det\]](#).
- [28] ATLAS Collaboration, *Performance of the ATLAS trigger system in 2015*, *Eur. Phys. J. C* **77** (2017) 317, arXiv: [1611.09661 \[hep-ex\]](#).
- [29] ATLAS Collaboration, *ATLAS data quality operations and performance for 2015–2018 data-taking*, *JINST* **15** (2020) P04003, arXiv: [1911.04632 \[physics.ins-det\]](#).
- [30] ATLAS Collaboration, *Luminosity determination in pp collisions at $\sqrt{s} = 13$ TeV using the ATLAS detector at the LHC*, *Eur. Phys. J. C* **83** (2023) 982, arXiv: [2212.09379 \[hep-ex\]](#).
- [31] ATLAS Collaboration, *Software and computing for Run 3 of the ATLAS experiment at the LHC*, *Eur. Phys. J. C* **85** (2024) 234, arXiv: [2404.06335 \[hep-ex\]](#).

- [32] ATLAS and CMS Collaborations, *Combined Measurement of the Higgs Boson Mass in pp Collisions at $\sqrt{s} = 7$ and 8 TeV with the ATLAS and CMS Experiments*, *Phys. Rev. Lett.* **114** (2015) 191803, arXiv: [1503.07589 \[hep-ex\]](#).
- [33] A. Djouadi, J. Kalinowski and M. Spira, *HDECAY: a program for Higgs boson decays in the Standard Model and its supersymmetric extension*, *Comput. Phys. Commun.* **108** (1998) 56, arXiv: [hep-ph/9704448](#).
- [34] M. Spira, *QCD Effects in Higgs Physics*, *Fortsch. Phys.* **46** (1998) 203, arXiv: [hep-ph/9705337](#).
- [35] A. Djouadi, M. M. Mühlleitner and M. Spira, *Decays of Supersymmetric Particles: the Program SUSY-HIT (SUSpect-SdecaY-Hdecay-InTerface)*, *Acta Phys. Polon. B* **38** (2007) 635, arXiv: [hep-ph/0609292](#).
- [36] A. Bredenstein, A. Denner, S. Dittmaier and M. M. Weber, *Radiative corrections to the semileptonic and hadronic Higgs-boson decays $H \rightarrow WW/ZZ \rightarrow 4$ fermions*, *JHEP* **02** (2007) 080, arXiv: [hep-ph/0611234](#).
- [37] A. Bredenstein, A. Denner, S. Dittmaier and M. M. Weber, *Precise predictions for the Higgs-boson decay $H \rightarrow WW/ZZ \rightarrow 4$ leptons*, *Phys. Rev. D* **74** (2006) 013004, arXiv: [hep-ph/0604011 \[hep-ph\]](#).
- [38] A. Bredenstein, A. Denner, S. Dittmaier and M. M. Weber, *Precision calculations for the Higgs decays $H \rightarrow ZZ/WW \rightarrow 4$ leptons*, *Nucl. Phys. B Proc. Suppl.* **160** (2006) 131, arXiv: [hep-ph/0607060 \[hep-ph\]](#).
- [39] J. Butterworth et al., *PDF4LHC recommendations for LHC Run II*, *J. Phys. G* **43** (2016) 023001, arXiv: [1510.03865 \[hep-ph\]](#).
- [40] T. Sjöstrand et al., *An introduction to PYTHIA 8.2*, *Comput. Phys. Commun.* **191** (2015) 159, arXiv: [1410.3012 \[hep-ph\]](#).
- [41] ATLAS Collaboration, *Measurement of the Z/γ^* boson transverse momentum distribution in pp collisions at $\sqrt{s} = 7$ TeV with the ATLAS detector*, *JHEP* **09** (2014) 145, arXiv: [1406.3660 \[hep-ex\]](#).
- [42] ATLAS Collaboration, *ATLAS Pythia 8 tunes to 7 TeV data*, ATL-PHYS-PUB-2014-021, 2014, URL: <https://cds.cern.ch/record/1966419>.
- [43] D. J. Lange, *The EvtGen particle decay simulation package*, *Nucl. Instrum. Meth. A* **462** (2001) 152.
- [44] P. Nason, *A new method for combining NLO QCD with shower Monte Carlo algorithms*, *JHEP* **11** (2004) 040, arXiv: [hep-ph/0409146](#).
- [45] S. Frixione, P. Nason and C. Oleari, *Matching NLO QCD computations with parton shower simulations: the POWHEG method*, *JHEP* **11** (2007) 070, arXiv: [0709.2092 \[hep-ph\]](#).
- [46] P. Nason and C. Oleari, *NLO Higgs boson production via vector-boson fusion matched with shower in POWHEG*, *JHEP* **02** (2010) 037, arXiv: [0911.5299 \[hep-ph\]](#).
- [47] S. Alioli, P. Nason, C. Oleari and E. Re, *A general framework for implementing NLO calculations in shower Monte Carlo programs: the POWHEG BOX*, *JHEP* **06** (2010) 043, arXiv: [1002.2581 \[hep-ph\]](#).

- [48] G. Luisoni, P. Nason, C. Oleari and F. Tramontano, *HW[±]/HZ + 0 and 1 jet at NLO with the POWHEG BOX interfaced to GoSam and their merging within MiNLO*, **JHEP** **10** (2013) 083, arXiv: [1306.2542 \[hep-ph\]](#).
- [49] M. L. Ciccolini, S. Dittmaier and M. Krämer, *Electroweak radiative corrections to associated WH and ZH production at hadron colliders*, **Phys. Rev. D** **68** (2003) 073003, arXiv: [hep-ph/0306234 \[hep-ph\]](#).
- [50] O. Brein, A. Djouadi and R. Harlander, *NNLO QCD corrections to the Higgs-strahlung processes at hadron colliders*, **Phys. Lett. B** **579** (2004) 149, arXiv: [hep-ph/0307206](#).
- [51] O. Brein, R. V. Harlander, M. Wiesemann and T. Zirke, *Top-quark mediated effects in hadronic Higgs-Strahlung*, **Eur. Phys. J. C** **72** (2012) 1868, arXiv: [1111.0761 \[hep-ph\]](#).
- [52] O. Brein, R. V. Harlander and T. J. E. Zirke, *vh@nnlo – Higgs Strahlung at hadron colliders*, **Comput. Phys. Commun.** **184** (2013) 998, arXiv: [1210.5347 \[hep-ph\]](#).
- [53] A. Denner, S. Dittmaier, S. Kallweit and A. Mück, *HAWK 2.0: A Monte Carlo program for Higgs production in vector-boson fusion and Higgs strahlung at hadron colliders*, **Comput. Phys. Commun.** **195** (2015) 161, arXiv: [1412.5390 \[hep-ph\]](#).
- [54] L. Altenkamp, S. Dittmaier, R. V. Harlander, H. Rzehak and T. J. E. Zirke, *Gluon-induced Higgs-strahlung at next-to-leading order QCD*, **JHEP** **02** (2013) 078, arXiv: [1211.5015 \[hep-ph\]](#).
- [55] R. V. Harlander, A. Kulesza, V. Theeuwes and T. Zirke, *Soft gluon resummation for gluon-induced Higgs Strahlung*, **JHEP** **11** (2014) 082, arXiv: [1410.0217 \[hep-ph\]](#).
- [56] K. Hamilton, P. Nason, E. Re and G. Zanderighi, *NNLOPS simulation of Higgs boson production*, **JHEP** **10** (2013) 222, arXiv: [1309.0017 \[hep-ph\]](#).
- [57] K. Hamilton, P. Nason and G. Zanderighi, *MINLO: multi-scale improved NLO*, **JHEP** **10** (2012) 155, arXiv: [1206.3572 \[hep-ph\]](#).
- [58] J. M. Campbell et al., *NLO Higgs boson production plus one and two jets using the POWHEG BOX, MadGraph4 and MCFM*, **JHEP** **07** (2012) 092, arXiv: [1202.5475 \[hep-ph\]](#).
- [59] K. Hamilton, P. Nason, C. Oleari and G. Zanderighi, *Merging H/W/Z + 0 and 1 jet at NLO with no merging scale: a path to parton shower + NNLO matching*, **JHEP** **05** (2013) 082, arXiv: [1212.4504 \[hep-ph\]](#).
- [60] S. Catani and M. Grazzini, *Next-to-Next-to-Leading-Order Subtraction Formalism in Hadron Collisions and its Application to Higgs-Boson Production at the Large Hadron Collider*, **Phys. Rev. Lett.** **98** (2007) 222002, arXiv: [hep-ph/0703012 \[hep-ph\]](#).
- [61] S. Actis, G. Passarino, C. Sturm and S. Uccirati, *NLO electroweak corrections to Higgs boson production at hadron colliders*, **Phys. Lett. B** **670** (2008) 12, arXiv: [0809.1301 \[hep-ph\]](#).
- [62] S. Actis, G. Passarino, C. Sturm and S. Uccirati, *NNLO computational techniques: The cases $H \rightarrow \gamma\gamma$ and $H \rightarrow gg$* , **Nucl. Phys. B** **811** (2009) 182, arXiv: [0809.3667 \[hep-ph\]](#).

- [63] R. V. Harlander and K. J. Ozeren,
Top mass effects in Higgs production at next-to-next-to-leading order QCD: Virtual corrections,
[*Phys. Lett. B* **679** \(2009\) 467](#), arXiv: [0907.2997 \[hep-ph\]](#).
- [64] R. V. Harlander and K. J. Ozeren,
Finite top mass effects for hadronic Higgs production at next-to-next-to-leading order,
[*JHEP* **11** \(2009\) 088](#), arXiv: [0909.3420 \[hep-ph\]](#).
- [65] A. Pak, M. Rogal and M. Steinhauser,
Finite top quark mass effects in NNLO Higgs boson production at LHC, [*JHEP* **02** \(2010\) 025](#),
arXiv: [0911.4662 \[hep-ph\]](#).
- [66] R. V. Harlander, H. Mantler, S. Marzani and K. J. Ozeren,
Higgs production in gluon fusion at next-to-next-to-leading order QCD for finite top mass,
[*Eur. Phys. J. C* **66** \(2010\) 359](#), arXiv: [0912.2104 \[hep-ph\]](#).
- [67] C. Anastasiou, C. Duhr, F. Dulat, F. Herzog and B. Mistlberger,
Higgs Boson Gluon-Fusion Production in QCD at Three Loops,
[*Phys. Rev. Lett.* **114** \(2015\) 212001](#), arXiv: [1503.06056 \[hep-ph\]](#).
- [68] C. Anastasiou et al.,
High precision determination of the gluon fusion Higgs boson cross-section at the LHC,
[*JHEP* **05** \(2016\) 058](#), arXiv: [1602.00695 \[hep-ph\]](#).
- [69] M. Bonetti, K. Melnikov and L. Tancredi, *Higher order corrections to mixed QCD-EW contributions to Higgs boson production in gluon fusion*, [*Phys. Rev. D* **97** \(2018\) 056017](#),
arXiv: [1801.10403 \[hep-ph\]](#), Erratum: [*Phys. Rev. D* **97** \(2018\) 099906\(E\)](#).
- [70] F. Dulat, A. Lazopoulos and B. Mistlberger, *iHixs 2 – Inclusive Higgs cross sections*,
[*Comput. Phys. Commun.* **233** \(2018\) 243](#), arXiv: [1802.00827 \[hep-ph\]](#).
- [71] M. Ciccolini, A. Denner and S. Dittmaier, *Strong and Electroweak Corrections to the Production of a Higgs Boson + 2 Jets via Weak Interactions at the Large Hadron Collider*,
[*Phys. Rev. Lett.* **99** \(2007\) 161803](#), arXiv: [0707.0381 \[hep-ph\]](#).
- [72] M. Ciccolini, A. Denner and S. Dittmaier,
Electroweak and QCD corrections to Higgs production via vector-boson fusion at the CERN LHC,
[*Phys. Rev. D* **77** \(2008\) 013002](#), arXiv: [0710.4749 \[hep-ph\]](#).
- [73] P. Bolzoni, F. Maltoni, S.-O. Moch and M. Zaro,
Higgs Boson Production via Vector-Boson Fusion at Next-to-Next-to-Leading Order in QCD,
[*Phys. Rev. Lett.* **105** \(2010\) 011801](#), arXiv: [1003.4451 \[hep-ph\]](#).
- [74] S. Frixione, G. Ridolfi and P. Nason,
A positive-weight next-to-leading-order Monte Carlo for heavy flavour hadroproduction,
[*JHEP* **09** \(2007\) 126](#), arXiv: [0707.3088 \[hep-ph\]](#).
- [75] H. B. Hartanto, B. Jäger, L. Reina and D. Wackerroth,
Higgs boson production in association with top quarks in the POWHEG BOX,
[*Phys. Rev. D* **91** \(2015\) 094003](#), arXiv: [1501.04498 \[hep-ph\]](#).
- [76] E. Bothmann et al., *Event generation with Sherpa 2.2*, [*SciPost Phys.* **7** \(2019\) 034](#),
arXiv: [1905.09127 \[hep-ph\]](#).
- [77] T. Gleisberg and S. Höche, *Comix, a new matrix element generator*, [*JHEP* **12** \(2008\) 039](#),
arXiv: [0808.3674 \[hep-ph\]](#).

- [78] F. Cascioli, P. Maierhöfer and S. Pozzorini, *Scattering Amplitudes with Open Loops*, *Phys. Rev. Lett.* **108** (2012) 111601, arXiv: [1111.5206 \[hep-ph\]](#).
- [79] A. Denner, S. Dittmaier and L. Hofer, *COLLIER: A fortran-based complex one-loop library in extended regularizations*, *Comput. Phys. Commun.* **212** (2017) 220, arXiv: [1604.06792 \[hep-ph\]](#).
- [80] F. Buccioni et al., *OpenLoops 2*, *Eur. Phys. J. C* **79** (2019) 866, arXiv: [1907.13071 \[hep-ph\]](#).
- [81] C. Anastasiou, L. Dixon, K. Melnikov and F. Petriello, *High-precision QCD at hadron colliders: Electroweak gauge boson rapidity distributions at next-to-next-to leading order*, *Phys. Rev. D* **69** (2004) 094008, arXiv: [hep-ph/0312266](#).
- [82] F. Buccioni, S. Pozzorini and M. Zoller, *On-the-fly reduction of open loops*, *Eur. Phys. J. C* **78** (2018) 70, arXiv: [1710.11452 \[hep-ph\]](#).
- [83] F. Caola, K. Melnikov, R. Röntsch and L. Tancredi, *QCD corrections to W^+W^- production through gluon fusion*, *Phys. Lett. B* **754** (2016) 275, arXiv: [1511.08617 \[hep-ph\]](#).
- [84] M. Grazzini, S. Kallweit, M. Wiesemann and J. Y. Yook, *ZZ production at the LHC: NLO QCD corrections to the loop-induced gluon fusion channel*, *JHEP* **03** (2019) 070, arXiv: [1811.09593 \[hep-ph\]](#).
- [85] NNPDF Collaboration, R. D. Ball et al., *Parton distributions for the LHC run II*, *JHEP* **04** (2015) 040, arXiv: [1410.8849 \[hep-ph\]](#).
- [86] S. Schumann and F. Krauss, *A parton shower algorithm based on Catani–Seymour dipole factorisation*, *JHEP* **03** (2008) 038, arXiv: [0709.1027 \[hep-ph\]](#).
- [87] S. Catani, F. Krauss, B. R. Webber and R. Kuhn, *QCD Matrix Elements + Parton Showers*, *JHEP* **11** (2001) 063, arXiv: [hep-ph/0109231](#).
- [88] S. Höche, F. Krauss, S. Schumann and F. Siegert, *QCD matrix elements and truncated showers*, *JHEP* **05** (2009) 053, arXiv: [0903.1219 \[hep-ph\]](#).
- [89] S. Höche, F. Krauss, M. Schönherr and F. Siegert, *A critical appraisal of NLO+PS matching methods*, *JHEP* **09** (2012) 049, arXiv: [1111.1220 \[hep-ph\]](#).
- [90] S. Höche, F. Krauss, M. Schönherr and F. Siegert, *QCD matrix elements + parton showers. The NLO case*, *JHEP* **04** (2013) 027, arXiv: [1207.5030 \[hep-ph\]](#).
- [91] J. Alwall et al., *The automated computation of tree-level and next-to-leading order differential cross sections, and their matching to parton shower simulations*, *JHEP* **07** (2014) 079, arXiv: [1405.0301 \[hep-ph\]](#).
- [92] ATLAS Collaboration, *Studies on top-quark Monte Carlo modelling for Top2016*, ATL-PHYS-PUB-2016-020, 2016, URL: <https://cds.cern.ch/record/2216168>.
- [93] M. Beneke, P. Falgari, S. Klein and C. Schwinn, *Hadronic top-quark pair production with NNLL threshold resummation*, *Nucl. Phys. B* **855** (2012) 695, arXiv: [1109.1536 \[hep-ph\]](#).

- [94] M. Cacciari, M. Czakon, M. Mangano, A. Mitov and P. Nason, *Top-pair production at hadron colliders with next-to-next-to-leading logarithmic soft-gluon resummation*, [*Phys. Lett. B* **710** \(2012\) 612](#), arXiv: [1111.5869 \[hep-ph\]](#).
- [95] P. Bärnreuther, M. Czakon and A. Mitov, *Percent-Level-Precision Physics at the Tevatron: Next-to-Next-to-Leading Order QCD Corrections to $q\bar{q} \rightarrow t\bar{t} + X$* , [*Phys. Rev. Lett.* **109** \(2012\) 132001](#), arXiv: [1204.5201 \[hep-ph\]](#).
- [96] M. Czakon and A. Mitov, *NNLO corrections to top-pair production at hadron colliders: the all-fermionic scattering channels*, [*JHEP* **12** \(2012\) 054](#), arXiv: [1207.0236 \[hep-ph\]](#).
- [97] M. Czakon and A. Mitov, *NNLO corrections to top pair production at hadron colliders: the quark-gluon reaction*, [*JHEP* **01** \(2013\) 080](#), arXiv: [1210.6832 \[hep-ph\]](#).
- [98] M. Czakon, P. Fiedler and A. Mitov, *Total Top-Quark Pair-Production Cross Section at Hadron Colliders Through $O(\alpha_S^4)$* , [*Phys. Rev. Lett.* **110** \(2013\) 252004](#), arXiv: [1303.6254 \[hep-ph\]](#).
- [99] M. Czakon and A. Mitov, *Top++: A program for the calculation of the top-pair cross-section at hadron colliders*, [*Comput. Phys. Commun.* **185** \(2014\) 2930](#), arXiv: [1112.5675 \[hep-ph\]](#).
- [100] E. Re, *Single-top Wt-channel production matched with parton showers using the POWHEG method*, [*Eur. Phys. J. C* **71** \(2011\) 1547](#), arXiv: [1009.2450 \[hep-ph\]](#).
- [101] S. Frixione, E. Laenen, P. Motylinski, C. White and B. R. Webber, *Single-top hadroproduction in association with a W boson*, [*JHEP* **07** \(2008\) 029](#), arXiv: [0805.3067 \[hep-ph\]](#).
- [102] S. Agostinelli et al., *GEANT4 – a simulation toolkit*, [*Nucl. Instrum. Meth. A* **506** \(2003\) 250](#).
- [103] ATLAS Collaboration, *The ATLAS Simulation Infrastructure*, [*Eur. Phys. J. C* **70** \(2010\) 823](#), arXiv: [1005.4568 \[physics.ins-det\]](#).
- [104] ATLAS Collaboration, *Software and computing for Run 3 of the ATLAS experiment at the LHC*, (2024), arXiv: [2404.06335 \[hep-ex\]](#).
- [105] T. Sjöstrand, S. Mrenna and P. Skands, *A brief introduction to PYTHIA 8.1*, [*Comput. Phys. Commun.* **178** \(2008\) 852](#), arXiv: [0710.3820 \[hep-ph\]](#).
- [106] NNPDF Collaboration, R. D. Ball et al., *Parton distributions with LHC data*, [*Nucl. Phys. B* **867** \(2013\) 244](#), arXiv: [1207.1303 \[hep-ph\]](#).
- [107] ATLAS Collaboration, *The Pythia 8 A3 tune description of ATLAS minimum bias and inelastic measurements incorporating the Donnachie–Landshoff diffractive model*, ATL-PHYS-PUB-2016-017, 2016, URL: <https://cds.cern.ch/record/2206965>.
- [108] M. Bähr et al., *Herwig++ physics and manual*, [*Eur. Phys. J. C* **58** \(2008\) 639](#), arXiv: [0803.0883 \[hep-ph\]](#).
- [109] J. Bellm et al., *Herwig 7.0/Herwig++ 3.0 release note*, [*Eur. Phys. J. C* **76** \(2016\) 196](#), arXiv: [1512.01178 \[hep-ph\]](#).
- [110] F. Cascioli et al., *Precise Higgs-background predictions: merging NLO QCD and squared quark-loop corrections to four-lepton + 0,1 jet production*, [*JHEP* **01** \(2014\) 046](#), arXiv: [1309.0500 \[hep-ph\]](#).

- [111] T. Binoth, G. Ossola, C. G. Papadopoulos and R. Pittau, *NLO QCD corrections to tri-boson production*, [*JHEP* **06** \(2008\) 082](#), arXiv: [0804.0350 \[hep-ph\]](#).
- [112] N. Kidonakis, *Two-loop soft anomalous dimensions for single top quark associated production with a W^- or H^-* , [*Phys. Rev. D* **82** \(2010\) 054018](#), arXiv: [1005.4451 \[hep-ph\]](#).
- [113] N. Kidonakis, ‘Top Quark Production’, *Proceedings, Helmholtz International Summer School on Physics of Heavy Quarks and Hadrons (HQ 2013)* (JINR, Dubna, Russia, 15th–28th July 2013) 139, arXiv: [1311.0283 \[hep-ph\]](#).
- [114] A. Broggio et al., *Top-quark pair hadroproduction in association with a heavy boson at NLO+NNLL including EW corrections*, [*JHEP* **08** \(2019\) 039](#), arXiv: [1907.04343 \[hep-ph\]](#).
- [115] J. Campbell, R. K. Ellis and R. Röntsch, *Single top production in association with a Z boson at the LHC*, [*Phys. Rev. D* **87** \(2013\) 114006](#), arXiv: [1302.3856 \[hep-ph\]](#).
- [116] F. Maltoni, L. Mantani and K. Mimasu, *Top-quark electroweak interactions at high energy*, [*JHEP* **10** \(2019\) 004](#), arXiv: [1904.05637 \[hep-ph\]](#).
- [117] ATLAS Collaboration, *Performance of electron and photon triggers in ATLAS during LHC Run 2*, [*Eur. Phys. J. C* **80** \(2020\) 47](#), arXiv: [1909.00761 \[hep-ex\]](#).
- [118] ATLAS Collaboration, *Performance of the ATLAS muon triggers in Run 2*, [*JINST* **15** \(2020\) P09015](#), arXiv: [2004.13447 \[physics.ins-det\]](#).
- [119] ATLAS Collaboration, *Vertex Reconstruction Performance of the ATLAS Detector at $\sqrt{s} = 13$ TeV*, ATL-PHYS-PUB-2015-026, 2015, URL: <https://cds.cern.ch/record/2037717>.
- [120] ATLAS Collaboration, *Electron and photon efficiencies in LHC Run 2 with the ATLAS experiment*, [*JHEP* **05** \(2024\) 162](#), arXiv: [2308.13362 \[hep-ex\]](#).
- [121] ATLAS Collaboration, *Muon reconstruction and identification efficiency in ATLAS using the full Run 2 pp collision data set at $\sqrt{s} = 13$ TeV*, [*Eur. Phys. J. C* **81** \(2021\) 578](#), arXiv: [2012.00578 \[hep-ex\]](#).
- [122] ATLAS Collaboration, *Electron and photon performance measurements with the ATLAS detector using the 2015–2017 LHC proton–proton collision data*, [*JINST* **14** \(2019\) P12006](#), arXiv: [1908.00005 \[hep-ex\]](#).
- [123] M. Cacciari, G. P. Salam and G. Soyez, *The anti- k_t jet clustering algorithm*, [*JHEP* **04** \(2008\) 063](#), arXiv: [0802.1189 \[hep-ph\]](#).
- [124] M. Cacciari, G. P. Salam and G. Soyez, *FastJet user manual*, [*Eur. Phys. J. C* **72** \(2012\) 1896](#), arXiv: [1111.6097 \[hep-ph\]](#).
- [125] ATLAS Collaboration, *Jet reconstruction and performance using particle flow with the ATLAS Detector*, [*Eur. Phys. J. C* **77** \(2017\) 466](#), arXiv: [1703.10485 \[hep-ex\]](#).
- [126] ATLAS Collaboration, *Jet energy scale and resolution measured in proton–proton collisions at $\sqrt{s} = 13$ TeV with the ATLAS detector*, [*Eur. Phys. J. C* **81** \(2021\) 689](#), arXiv: [2007.02645 \[hep-ex\]](#).

- [127] ATLAS Collaboration, *Performance of pile-up mitigation techniques for jets in pp collisions at $\sqrt{s} = 8$ TeV using the ATLAS detector*, *Eur. Phys. J. C* **76** (2016) 581, arXiv: [1510.03823 \[hep-ex\]](#).
- [128] ATLAS Collaboration, *Identification and rejection of pile-up jets at high pseudorapidity with the ATLAS detector*, *Eur. Phys. J. C* **77** (2017) 580, arXiv: [1705.02211 \[hep-ex\]](#), Erratum: *Eur. Phys. J. C* **77** (2017) 712.
- [129] ATLAS Collaboration, *Forward jet vertex tagging using the particle flow algorithm*, ATL-PHYS-PUB-2019-026, 2019, URL: <https://cds.cern.ch/record/2683100>.
- [130] ATLAS Collaboration, *ATLAS flavour-tagging algorithms for the LHC Run 2 pp collision dataset*, *Eur. Phys. J. C* **83** (2023) 681, arXiv: [2211.16345 \[physics.data-an\]](#).
- [131] ATLAS Collaboration, *ATLAS b-jet identification performance and efficiency measurement with $t\bar{t}$ events in pp collisions at $\sqrt{s} = 13$ TeV*, *Eur. Phys. J. C* **79** (2019) 970, arXiv: [1907.05120 \[hep-ex\]](#).
- [132] ATLAS Collaboration, *The performance of missing transverse momentum reconstruction and its significance with the ATLAS detector using 140fb^{-1} of $\sqrt{s} = 13$ TeV pp collisions*, (2024), arXiv: [2402.05858 \[hep-ex\]](#).
- [133] ATLAS Collaboration, *Measurement and interpretation of same-sign W boson pair production in association with two jets in pp collisions at $\sqrt{s} = 13$ TeV with the ATLAS detector*, *JHEP* **04** (2024) 026, arXiv: [2312.00420 \[hep-ex\]](#).
- [134] S. Hochreiter and J. Schmidhuber, *Long Short-Term Memory*, *Neural Comput.* **9** (1997) 1735.
- [135] ATLAS Collaboration, *Observation of WWW Production in pp Collisions at $\sqrt{s} = 13$ TeV with the ATLAS Detector*, *Phys. Rev. Lett.* **129** (2022) 061803, arXiv: [2201.13045 \[hep-ex\]](#).
- [136] ATLAS Collaboration, *Electron and photon energy calibration with the ATLAS detector using LHC Run 2 data*, *JINST* **19** (2024) P02009, arXiv: [2309.05471 \[hep-ex\]](#).
- [137] ATLAS Collaboration, *Studies of the muon momentum calibration and performance of the ATLAS detector with pp collisions at $\sqrt{s} = 13$ TeV*, *Eur. Phys. J. C* **83** (2023) 686, arXiv: [2212.07338 \[hep-ex\]](#).
- [138] G. Avoni et al., *The new LUCID-2 detector for luminosity measurement and monitoring in ATLAS*, *JINST* **13** (2018) P07017.
- [139] S. Höche, S. Schumann and F. Siegert, *Hard photon production and matrix-element parton-shower merging*, *Phys. Rev. D* **81** (2010) 034026, arXiv: [0912.3501 \[hep-ph\]](#).
- [140] ATLAS Collaboration, *Evaluation of theoretical uncertainties for simplified template cross section measurements of V-associated production of the Higgs boson*, ATL-PHYS-PUB-2018-035, 2018, URL: <https://cds.cern.ch/record/2649241>.
- [141] G. Cowan, K. Cranmer, E. Gross and O. Vitells, *Asymptotic formulae for likelihood-based tests of new physics*, *Eur. Phys. J. C* **71** (2011) 1554, arXiv: [1007.1727 \[physics.data-an\]](#), Erratum: *Eur. Phys. J. C* **73** (2013) 2501.

- [142] ATLAS Collaboration, *ATLAS Computing Acknowledgements*, ATL-SOFT-PUB-2025-001, 2025, URL: <https://cds.cern.ch/record/2922210>.
- [143] T. Plehn, D. Rainwater and D. Zeppenfeld,
A Method for identifying $H \rightarrow \tau^+\tau^- \rightarrow e^\pm\mu^\mp p_T$ at the CERN LHC,
Phys. Rev. D **61** (2000) 093005, arXiv: [hep-ph/9911385](https://arxiv.org/abs/hep-ph/9911385).

The ATLAS Collaboration

G. Aad ¹⁰⁵, E. Aakvaag ¹⁷, B. Abbott ¹²⁴, S. Abdelhameed ^{120a}, K. Abeling ⁵⁷, N.J. Abicht ⁵¹, S.H. Abidi ³⁰, M. Aboeela ⁴⁶, A. Aboulhorma ^{36e}, H. Abramowicz ¹⁵⁶, H. Abreu ¹⁵⁵, Y. Abulaiti ¹²¹, B.S. Acharya ^{71a,71b,1}, A. Ackermann ^{65a}, C. Adam Bourdarios ⁴, L. Adamczyk ^{88a}, S.V. Addepalli ²⁷, M.J. Addison ¹⁰⁴, J. Adelman ¹¹⁹, A. Adiguzel ^{22c}, T. Adye ¹³⁸, A.A. Affolder ¹⁴⁰, Y. Afik ⁴¹, M.N. Agaras ¹³, J. Agarwala ^{75a,75b}, A. Aggarwal ¹⁰³, C. Agheorghiesei ^{28c}, F. Ahmadov ^{40,aa}, W.S. Ahmed ¹⁰⁷, S. Ahuja ⁹⁸, X. Ai ^{64e}, G. Aielli ^{78a,78b}, A. Aikot ¹⁶⁸, M. Ait Tamlihat ^{36e}, B. Aitbenchikh ^{36a}, M. Akbiyik ¹⁰³, T.P.A. Åkesson ¹⁰¹, A.V. Akimov ¹⁵⁰, D. Akiyama ¹⁷³, N.N. Akolkar ²⁵, S. Aktas ^{22a}, K. Al Houry ⁴³, G.L. Alberghi ^{24b}, J. Albert ¹⁷⁰, P. Albicocco ⁵⁵, G.L. Albouy ⁶², S. Alderweireldt ⁵⁴, Z.L. Alegria ¹²⁵, M. Aleksa ³⁷, I.N. Aleksandrov ⁴⁰, C. Alexa ^{28b}, T. Alexopoulos ¹⁰, F. Alfonsi ^{24b}, M. Algren ⁵⁸, M. Alhroob ¹⁷², B. Ali ¹³⁶, H.M.J. Ali ^{94,t}, S. Ali ³², S.W. Alibocus ⁹⁵, M. Aliev ^{34c}, G. Alimonti ^{73a}, W. Alkakh ⁵⁷, C. Allaire ⁶⁸, B.M.M. Allbrooke ¹⁵¹, J.S. Allen ¹⁰⁴, J.F. Allen ⁵⁴, C.A. Allendes Flores ^{141f}, P.P. Allport ²¹, A. Aloisio ^{74a,74b}, F. Alonso ⁹³, C. Alpigiani ¹⁴³, Z.M.K. Alsolami ⁹⁴, M. Alvarez Estevez ¹⁰², A. Alvarez Fernandez ¹⁰³, M. Alves Cardoso ⁵⁸, M.G. Alviggi ^{74a,74b}, M. Aly ¹⁰⁴, Y. Amaral Coutinho ^{85b}, A. Ambler ¹⁰⁷, C. Amelung ³⁷, M. Amerl ¹⁰⁴, C.G. Ames ¹¹², D. Amidei ¹⁰⁹, B. Amini ⁵⁶, K. Amirie ¹⁵⁹, S.P. Amor Dos Santos ^{134a}, K.R. Amos ¹⁶⁸, D. Amperiadou ¹⁵⁷, S. An ⁸⁶, V. Ananiev ¹²⁹, C. Anastopoulos ¹⁴⁴, T. Andeen ¹¹, J.K. Anders ³⁷, A.C. Anderson ⁶¹, S.Y. Andrean ^{49a,49b}, A. Andreazza ^{73a,73b}, S. Angelidakis ⁹, A. Angerami ⁴³, A.V. Anisenkov ³⁹, A. Annovi ^{76a}, C. Antel ⁵⁸, E. Antipov ¹⁵⁰, M. Antonelli ⁵⁵, F. Anulli ^{77a}, M. Aoki ⁸⁶, T. Aoki ¹⁵⁸, M.A. Aparo ¹⁵¹, L. Aperio Bella ⁵⁰, C. Appelt ¹⁵⁶, A. Apyan ²⁷, S.J. Arbiol Val ⁸⁹, C. Arcangeletti ⁵⁵, A.T.H. Arce ⁵³, J-F. Arguin ¹¹¹, S. Argyropoulos ¹⁵⁷, J.-H. Arling ⁵⁰, O. Arnaez ⁴, H. Arnold ¹⁵⁰, G. Artoni ^{77a,77b}, H. Asada ¹¹⁴, K. Asai ¹²², S. Asai ¹⁵⁸, N.A. Asbah ³⁷, R.A. Ashby Pickering ¹⁷², K. Assamagan ³⁰, R. Astalos ^{29a}, K.S.V. Astrand ¹⁰¹, S. Atashi ¹⁶³, R.J. Atkin ^{34a}, M. Atkinson ¹⁶⁷, H. Atmani ^{36f}, P.A. Atlasiddha ¹³², K. Augsten ¹³⁶, S. Auricchio ^{74a,74b}, A.D. Auriol ²¹, V.A. Austrup ¹⁰⁴, G. Avolio ³⁷, K. Axiotis ⁵⁸, G. Azuelos ^{111,ae}, D. Babal ^{29b}, H. Bachacou ¹³⁹, K. Bachas ^{157,p}, A. Bachiu ³⁵, E. Bachmann ⁵², F. Backman ^{49a,49b}, A. Badea ⁴¹, T.M. Baer ¹⁰⁹, P. Bagnaia ^{77a,77b}, M. Bahmani ¹⁹, D. Bahner ⁵⁶, K. Bai ¹²⁷, J.T. Baines ¹³⁸, L. Baines ⁹⁷, O.K. Baker ¹⁷⁷, E. Bakos ¹⁶, D. Bakshi Gupta ⁸, L.E. Balabram Filho ^{85b}, V. Balakrishnan ¹²⁴, R. Balasubramanian ⁴, E.M. Baldin ³⁹, P. Balek ^{88a}, E. Ballabene ^{24b,24a}, F. Balli ¹³⁹, L.M. Baltes ^{65a}, W.K. Balunas ³³, J. Balz ¹⁰³, I. Bamwidhi ^{120b}, E. Banas ⁸⁹, M. Bandieramonte ¹³³, A. Bandyopadhyay ²⁵, S. Bansal ²⁵, L. Barak ¹⁵⁶, M. Barakat ⁵⁰, E.L. Barberio ¹⁰⁸, D. Barberis ^{59b,59a}, M. Barbero ¹⁰⁵, M.Z. Barel ¹¹⁸, T. Barillari ¹¹³, M.-S. Barisits ³⁷, T. Barklow ¹⁴⁸, P. Baron ¹²⁶, D.A. Baron Moreno ¹⁰⁴, A. Baroncelli ^{64a}, A.J. Barr ¹³⁰, J.D. Barr ⁹⁹, F. Barreiro ¹⁰², J. Barreiro Guimarães da Costa ¹⁴, U. Barron ¹⁵⁶, M.G. Barros Teixeira ^{134a}, S. Barsov ³⁹, F. Bartels ^{65a}, R. Bartoldus ¹⁴⁸, A.E. Barton ⁹⁴, P. Bartos ^{29a}, A. Basan ¹⁰³, M. Baselga ⁵¹, A. Bassalat ^{68,b}, M.J. Basso ^{160a}, S. Bataju ⁴⁶, R. Bate ¹⁶⁹, R.L. Bates ⁶¹, S. Batlamous ¹⁰², B. Batool ¹⁴⁶, M. Battaglia ¹⁴⁰, D. Battulga ¹⁹, M. Bause ^{77a,77b}, M. Bauer ⁸¹, P. Bauer ²⁵, L.T. Bazzano Hurrell ³¹, J.B. Beacham ⁵³, T. Beau ¹³¹, J.Y. Beaucamp ⁹³, P.H. Beauchemin ¹⁶², P. Bechtel ²⁵, H.P. Beck ^{20,o}, K. Becker ¹⁷², A.J. Beddall ⁸⁴, V.A. Bednyakov ⁴⁰, C.P. Bee ¹⁵⁰, L.J. Beemster ¹⁶, T.A. Beermann ³⁷, M. Begalli ^{85d}, M. Begel ³⁰, A. Behera ¹⁵⁰, J.K. Behr ⁵⁰, J.F. Beirer ³⁷, F. Beisiegel ²⁵, M. Belfkir ^{120b}, G. Bella ¹⁵⁶, L. Bellagamba ^{24b}, A. Bellerive ³⁵, P. Bellos ²¹,

K. Beloborodov ^{id39}, D. Benchekroun ^{id36a}, F. Bendebba ^{id36a}, Y. Benhammou ^{id156},
 K.C. Benkendorfer ^{id63}, L. Beresford ^{id50}, M. Beretta ^{id55}, E. Bergeaas Kuutmann ^{id166}, N. Berger ^{id4},
 B. Bergmann ^{id136}, J. Beringer ^{id18a}, G. Bernardi ^{id5}, C. Bernius ^{id148}, F.U. Bernlochner ^{id25},
 F. Bernon ^{id37}, A. Berrocal Guardia ^{id13}, T. Berry ^{id98}, P. Berta ^{id137}, A. Berthold ^{id52}, S. Bethke ^{id113},
 A. Betti ^{id77a,77b}, A.J. Bevan ^{id97}, N.K. Bhalla ^{id56}, S. Bhatta ^{id150}, D.S. Bhattacharya ^{id171},
 P. Bhattacharai ^{id148}, Z.M. Bhatti ^{id121}, K.D. Bhide ^{id56}, V.S. Bhopatkar ^{id125}, R.M. Bianchi ^{id133},
 G. Bianco ^{id24b,24a}, O. Biebel ^{id112}, R. Bielski ^{id127}, M. Biglietti ^{id79a}, C.S. Billingsley ^{id46}, Y. Bimgdi ^{id36f},
 M. Bindi ^{id57}, A. Bingham ^{id176}, A. Bingul ^{id22b}, C. Bini ^{id77a,77b}, G.A. Bird ^{id33}, M. Birman ^{id174},
 M. Biros ^{id137}, S. Biryukov ^{id151}, T. Bisanz ^{id51}, E. Bisceglie ^{id45b,45a}, J.P. Biswal ^{id138}, D. Biswas ^{id146},
 I. Bloch ^{id50}, A. Blue ^{id61}, U. Blumenschein ^{id97}, J. Blumenthal ^{id103}, V.S. Bobrovnikov ^{id39},
 M. Boehler ^{id56}, B. Boehm ^{id171}, D. Bogavac ^{id37}, A.G. Bogdanchikov ^{id39}, L.S. Boggia ^{id131},
 C. Bohm ^{id49a}, V. Boisvert ^{id98}, P. Bokan ^{id37}, T. Bold ^{id88a}, M. Bomben ^{id5}, M. Bona ^{id97},
 M. Boonekamp ^{id139}, C.D. Booth ^{id98}, A.G. Borbély ^{id61}, I.S. Bordulev ^{id39}, G. Borissov ^{id94},
 D. Bortoletto ^{id130}, D. Boscherini ^{id24b}, M. Bosman ^{id13}, J.D. Bossio Sola ^{id37}, K. Bouaouda ^{id36a},
 N. Bouchhar ^{id168}, L. Boudet ^{id4}, J. Boudreau ^{id133}, E.V. Bouhova-Thacker ^{id94}, D. Boumediene ^{id42},
 R. Bouquet ^{id59b,59a}, A. Boveia ^{id123}, J. Boyd ^{id37}, D. Boye ^{id30}, I.R. Boyko ^{id40}, L. Bozianu ^{id58},
 J. Bracinik ^{id21}, N. Brahimi ^{id4}, G. Brandt ^{id176}, O. Brandt ^{id33}, F. Braren ^{id50}, B. Brau ^{id106},
 J.E. Brau ^{id127}, R. Brenner ^{id174}, L. Brenner ^{id118}, R. Brenner ^{id166}, S. Bressler ^{id174}, G. Brianti ^{id80a,80b},
 D. Britton ^{id61}, D. Britzger ^{id113}, I. Brock ^{id25}, R. Brock ^{id110}, G. Brooijmans ^{id43}, A.J. Brooks ^{id70},
 E.M. Brooks ^{id160b}, E. Brost ^{id30}, L.M. Brown ^{id170,160a}, L.E. Bruce ^{id63}, T.L. Bruckler ^{id130},
 P.A. Bruckman de Renstrom ^{id89}, B. Brüers ^{id50}, A. Bruni ^{id24b}, G. Bruni ^{id24b}, M. Bruschi ^{id24b},
 N. Bruscino ^{id77a,77b}, T. Buanes ^{id17}, Q. Buat ^{id143}, D. Buchin ^{id113}, A.G. Buckley ^{id61}, O. Bulekov ^{id39},
 B.A. Bullard ^{id148}, S. Burdin ^{id95}, C.D. Burgard ^{id51}, A.M. Burger ^{id37}, B. Burghgrave ^{id8},
 O. Burlayenko ^{id56}, J. Burleson ^{id167}, J.T.P. Burr ^{id33}, J.C. Burzynski ^{id147}, E.L. Busch ^{id43},
 V. Büscher ^{id103}, P.J. Bussey ^{id61}, J.M. Butler ^{id26}, C.M. Buttar ^{id61}, J.M. Butterworth ^{id99},
 W. Buttinger ^{id138}, C.J. Buxo Vazquez ^{id110}, A.R. Buzykaev ^{id39}, S. Cabrera Urbán ^{id168},
 L. Cadamuro ^{id68}, D. Caforio ^{id60}, H. Cai ^{id133}, Y. Cai ^{id14,115c}, Y. Cai ^{id115a}, V.M.M. Cairo ^{id37},
 O. Cakir ^{id3a}, N. Calace ^{id37}, P. Calafiura ^{id18a}, G. Calderini ^{id131}, P. Calfayan ^{id35}, G. Callea ^{id61},
 L.P. Caloba ^{id85b}, D. Calvet ^{id42}, S. Calvet ^{id42}, M. Calvetti ^{id76a,76b}, R. Camacho Toro ^{id131},
 S. Camarda ^{id37}, D. Camarero Munoz ^{id27}, P. Camarri ^{id78a,78b}, M.T. Camerlingo ^{id74a,74b},
 D. Cameron ^{id37}, C. Camincher ^{id170}, M. Campanelli ^{id99}, A. Camplani ^{id44}, V. Canale ^{id74a,74b},
 A.C. Canbay ^{id3a}, E. Canonero ^{id98}, J. Cantero ^{id168}, Y. Cao ^{id167}, F. Capocasa ^{id27}, M. Capua ^{id45b,45a},
 A. Carbone ^{id73a,73b}, R. Cardarelli ^{id78a}, J.C.J. Cardenas ^{id8}, G. Carducci ^{id45b,45a}, T. Carli ^{id37},
 G. Carlino ^{id74a}, J.I. Carlotto ^{id13}, B.T. Carlson ^{id133,q}, E.M. Carlson ^{id170,160a}, J. Carmignani ^{id95},
 L. Carminati ^{id73a,73b}, A. Carnelli ^{id139}, M. Carnesale ^{id37}, S. Caron ^{id117}, E. Carquin ^{id141f},
 I.B. Carr ^{id108}, S. Carrá ^{id73a}, G. Carratta ^{id24b,24a}, A.M. Carroll ^{id127}, M.P. Casado ^{id13,i}, M. Caspar ^{id50},
 F.L. Castillo ^{id4}, L. Castillo Garcia ^{id13}, V. Castillo Gimenez ^{id168}, N.F. Castro ^{id134a,134e},
 A. Catinaccio ^{id37}, J.R. Catmore ^{id129}, T. Cavaliere ^{id4}, V. Cavaliere ^{id30}, N. Cavalli ^{id24b,24a},
 L.J. Caviedes Betancourt ^{id23b}, Y.C. Cekmecelioglu ^{id50}, E. Celebi ^{id84}, S. Cella ^{id37},
 M.S. Centonze ^{id72a,72b}, V. Cepaitis ^{id58}, K. Cerny ^{id126}, A.S. Cerqueira ^{id85a}, A. Cerri ^{id151},
 L. Cerrito ^{id78a,78b}, F. Cerutti ^{id18a}, B. Cervato ^{id146}, A. Cervelli ^{id24b}, G. Cesarini ^{id55}, S.A. Cetin ^{id84},
 D. Chakraborty ^{id119}, J. Chan ^{id18a}, W.Y. Chan ^{id158}, J.D. Chapman ^{id33}, E. Chapon ^{id139},
 B. Chargeishvili ^{id154b}, D.G. Charlton ^{id21}, M. Chatterjee ^{id20}, C. Chauhan ^{id137}, Y. Che ^{id115a},
 S. Chekanov ^{id6}, S.V. Chekulaev ^{id160a}, G.A. Chelkov ^{id40,a}, A. Chen ^{id109}, B. Chen ^{id156}, B. Chen ^{id170},
 H. Chen ^{id115a}, H. Chen ^{id30}, J. Chen ^{id64c}, J. Chen ^{id147}, M. Chen ^{id130}, S. Chen ^{id90}, S.J. Chen ^{id115a},
 X. Chen ^{id64c}, X. Chen ^{id15,ad}, Y. Chen ^{id64a}, C.L. Cheng ^{id175}, H.C. Cheng ^{id66a}, S. Cheong ^{id148},
 A. Cheplakov ^{id40}, E. Cheremushkina ^{id50}, E. Cherepanova ^{id118}, R. Cherkaoui El Moursli ^{id36e},

E. Cheu ⁷, K. Cheung ⁶⁷, L. Chevalier ¹³⁹, V. Chiarella ⁵⁵, G. Chiarelli ^{76a}, N. Chiedde ¹⁰⁵,
 G. Chiodini ^{72a}, A.S. Chisholm ²¹, A. Chitan ^{28b}, M. Chitishvili ¹⁶⁸, M.V. Chizhov ^{40,r},
 K. Choi ¹¹, Y. Chou ¹⁴³, E.Y.S. Chow ¹¹⁷, K.L. Chu ¹⁷⁴, M.C. Chu ^{66a}, X. Chu ^{14,115c},
 Z. Chubinidze ⁵⁵, J. Chudoba ¹³⁵, J.J. Chwastowski ⁸⁹, D. Cieri ¹¹³, K.M. Ciesla ^{88a},
 V. Cindro ⁹⁶, A. Ciocio ^{18a}, F. Cirotto ^{74a,74b}, Z.H. Citron ¹⁷⁴, M. Citterio ^{73a}, D.A. Ciubotaru ^{28b},
 A. Clark ⁵⁸, P.J. Clark ⁵⁴, N. Clarke Hall ⁹⁹, C. Clarry ¹⁵⁹, J.M. Clavijo Columbie ⁵⁰,
 S.E. Clawson ⁵⁰, C. Clement ^{49a,49b}, Y. Coadou ¹⁰⁵, M. Cobal ^{71a,71c}, A. Coccaro ^{59b},
 R.F. Coelho Barrue ^{134a}, R. Coelho Lopes De Sa ¹⁰⁶, S. Coelli ^{73a}, L.S. Colangeli ¹⁵⁹, B. Cole ⁴³,
 J. Collot ⁶², P. Conde Muiño ^{134a,134g}, M.P. Connell ^{34c}, S.H. Connell ^{34c}, E.I. Conroy ¹³⁰,
 F. Conventi ^{74a,af}, H.G. Cooke ²¹, A.M. Cooper-Sarkar ¹³⁰, F.A. Corchia ^{24b,24a},
 A. Cordeiro Oudot Choi ¹³¹, L.D. Corpe ⁴², M. Corradi ^{77a,77b}, F. Corriveau ^{107,y},
 A. Cortes-Gonzalez ¹⁹, M.J. Costa ¹⁶⁸, F. Costanza ⁴, D. Costanzo ¹⁴⁴, B.M. Cote ¹²³,
 J. Couthures ⁴, G. Cowan ⁹⁸, K. Cranmer ¹⁷⁵, L. Cremer ⁵¹, D. Cremonini ^{24b,24a},
 S. Crépe-Renaudin ⁶², F. Crescioli ¹³¹, M. Cristinziani ¹⁴⁶, M. Cristoforetti ^{80a,80b}, V. Croft ¹¹⁸,
 J.E. Crosby ¹²⁵, G. Crosetti ^{45b,45a}, A. Cueto ¹⁰², H. Cui ⁹⁹, Z. Cui ⁷, W.R. Cunningham ⁶¹,
 F. Curcio ¹⁶⁸, J.R. Curran ⁵⁴, P. Czodrowski ³⁷, M.J. Da Cunha Sargedass De Sousa ^{59b,59a},
 J.V. Da Fonseca Pinto ^{85b}, C. Da Via ¹⁰⁴, W. Dabrowski ^{88a}, T. Dado ³⁷, S. Dahbi ¹⁵³,
 T. Dai ¹⁰⁹, D. Dal Santo ²⁰, C. Dallapiccola ¹⁰⁶, M. Dam ⁴⁴, G. D'amen ³⁰, V. D'Amico ¹¹²,
 J. Damp ¹⁰³, J.R. Dandoy ³⁵, D. Dannheim ³⁷, M. Danninger ¹⁴⁷, V. Dao ¹⁵⁰, G. Darbo ^{59b},
 S.J. Das ³⁰, F. Dattola ⁵⁰, S. D'Auria ^{73a,73b}, A. D'Avanzo ^{74a,74b}, C. David ^{34a}, T. Davidek ¹³⁷,
 I. Dawson ⁹⁷, H.A. Day-hall ¹³⁶, K. De ⁸, R. De Asmundis ^{74a}, N. De Biase ⁵⁰,
 S. De Castro ^{24b,24a}, N. De Groot ¹¹⁷, P. de Jong ¹¹⁸, H. De la Torre ¹¹⁹, A. De Maria ^{115a},
 A. De Salvo ^{77a}, U. De Sanctis ^{78a,78b}, F. De Santis ^{72a,72b}, A. De Santo ¹⁵¹,
 J.B. De Vivie De Regie ⁶², J. Debevc ⁹⁶, D.V. Dedovich ⁴⁰, J. Degens ⁹⁵, A.M. Deiana ⁴⁶,
 F. Del Corso ^{24b,24a}, J. Del Peso ¹⁰², L. Delagrangé ¹³¹, F. Deliot ¹³⁹, C.M. Delitzsch ⁵¹,
 M. Della Pietra ^{74a,74b}, D. Della Volpe ⁵⁸, A. Dell'Acqua ³⁷, L. Dell'Asta ^{73a,73b}, M. Delmastro ⁴,
 C.C. Delogu ¹⁰³, P.A. Delsart ⁶², S. Demers ¹⁷⁷, M. Demichev ⁴⁰, S.P. Denisov ³⁹,
 L. D'Eramo ⁴², D. Derendarz ⁸⁹, F. Derue ¹³¹, P. Dervan ⁹⁵, K. Desch ²⁵, C. Deutsch ²⁵,
 F.A. Di Bello ^{59b,59a}, A. Di Ciaccio ^{78a,78b}, L. Di Ciaccio ⁴, A. Di Domenico ^{77a,77b},
 C. Di Donato ^{74a,74b}, A. Di Girolamo ³⁷, G. Di Gregorio ³⁷, A. Di Luca ^{80a,80b},
 B. Di Micco ^{79a,79b}, R. Di Nardo ^{79a,79b}, K.F. Di Petrillo ⁴¹, M. Diamantopoulou ³⁵, F.A. Dias ¹¹⁸,
 T. Dias Do Vale ¹⁴⁷, M.A. Diaz ^{141a,141b}, F.G. Diaz Capriles ²⁵, A.R. Didenko ⁴⁰, M. Didenko ¹⁶⁸,
 E.B. Diehl ¹⁰⁹, S. Díez Cornell ⁵⁰, C. Díez Pardos ¹⁴⁶, C. Dimitriadi ¹⁶⁶, A. Dimitrievska ²¹,
 J. Dingfelder ²⁵, T. Dingley ¹³⁰, I-M. Dinu ^{28b}, S.J. Dittmeier ^{65b}, F. Dittus ³⁷, M. Divisek ¹³⁷,
 B. Dixit ⁹⁵, F. Djama ¹⁰⁵, T. Djobava ^{154b}, C. Doglioni ^{104,101}, A. Dohnalova ^{29a}, J. Dolejsi ¹³⁷,
 Z. Dolezal ¹³⁷, K. Domijan ^{88a}, K.M. Dona ⁴¹, M. Donadelli ^{85d}, B. Dong ¹¹⁰, J. Donini ⁴²,
 A. D'Onofrio ^{74a,74b}, M. D'Onofrio ⁹⁵, J. Dopke ¹³⁸, A. Doria ^{74a}, N. Dos Santos Fernandes ^{134a},
 P. Dougan ¹⁰⁴, M.T. Dova ⁹³, A.T. Doyle ⁶¹, M.A. Dragnet ¹³⁰, M.P. Drescher ⁵⁷, E. Dreyer ¹⁷⁴,
 I. Drivas-koulouris ¹⁰, M. Drnevich ¹²¹, M. Drozdova ⁵⁸, D. Du ^{64a}, T.A. du Pree ¹¹⁸,
 F. Dubinin ³⁹, M. Dubovsky ^{29a}, E. Duchovni ¹⁷⁴, G. Duckeck ¹¹², O.A. Ducu ^{28b}, D. Duda ⁵⁴,
 A. Dudarev ³⁷, E.R. Duden ²⁷, M. D'uffizi ¹⁰⁴, L. Duflot ⁶⁸, M. Dührssen ³⁷, I. Duminica ^{28g},
 A.E. Dumitriu ^{28b}, M. Dunford ^{65a}, S. Dungs ⁵¹, K. Dunne ^{49a,49b}, A. Duperrin ¹⁰⁵,
 H. Duran Yildiz ^{3a}, M. Düren ⁶⁰, A. Durglishvili ^{154b}, D. Duvnjak ³⁵, B.L. Dwyer ¹¹⁹,
 G.I. Dyckes ^{18a}, M. Dyndal ^{88a}, B.S. Dziedzic ³⁷, Z.O. Earnshaw ¹⁵¹, G.H. Eberwein ¹³⁰,
 B. Eckerova ^{29a}, S. Eggebrecht ⁵⁷, E. Egidio Purcino De Souza ^{85e}, L.F. Ehrke ⁵⁸, G. Eigen ¹⁷,
 K. Einsweiler ^{18a}, T. Ekelof ¹⁶⁶, P.A. Ekman ¹⁰¹, S. El Farkh ^{36b}, Y. El Ghazali ^{64a},
 H. El Jarrari ³⁷, A. El Moussaouy ^{36a}, V. Ellajosyula ¹⁶⁶, M. Ellert ¹⁶⁶, F. Ellinghaus ¹⁷⁶,

N. Ellis ³⁷, J. Elmsheuser ³⁰, M. Elsayy ^{120a}, M. Elsing ³⁷, D. Emeliyanov ¹³⁸, Y. Enari ⁸⁶, I. Ene ^{18a}, S. Epari ¹³, P.A. Erland ⁸⁹, D. Ernani Martins Neto ⁸⁹, M. Errenst ¹⁷⁶, M. Escalier ⁶⁸, C. Escobar ¹⁶⁸, E. Etzion ¹⁵⁶, G. Evans ^{134a,134b}, H. Evans ⁷⁰, L.S. Evans ⁹⁸, A. Ezhilov ³⁹, S. Ezzarqtouni ^{36a}, F. Fabbri ^{24b,24a}, L. Fabbri ^{24b,24a}, G. Facini ⁹⁹, V. Fadeyev ¹⁴⁰, R.M. Fakhrutdinov ³⁹, D. Fakoudis ¹⁰³, S. Falciano ^{77a}, L.F. Falda Ulhoa Coelho ³⁷, F. Fallavollita ¹¹³, G. Falsetti ^{45b,45a}, J. Faltova ¹³⁷, C. Fan ¹⁶⁷, K.Y. Fan ^{66b}, Y. Fan ¹⁴, Y. Fang ^{14,115c}, M. Fanti ^{73a,73b}, M. Faraj ^{71a,71b}, Z. Farazpay ¹⁰⁰, A. Farbin ⁸, A. Farilla ^{79a}, T. Farooque ¹¹⁰, S.M. Farrington ^{138,54}, F. Fassi ^{36e}, D. Fassouliotis ⁹, M. Faucci Giannelli ^{78a,78b}, W.J. Fawcett ³³, L. Fayard ⁶⁸, P. Federic ¹³⁷, P. Federicova ¹³⁵, O.L. Fedin ^{39a}, M. Feickert ¹⁷⁵, L. Feligioni ¹⁰⁵, D.E. Fellers ¹²⁷, C. Feng ^{64b}, Z. Feng ¹¹⁸, M.J. Fenton ¹⁶³, L. Ferencz ⁵⁰, R.A.M. Ferguson ⁹⁴, S.I. Fernandez Luengo ^{141f}, P. Fernandez Martinez ⁶⁹, M.J.V. Fernoux ¹⁰⁵, J. Ferrando ⁹⁴, A. Ferrari ¹⁶⁶, P. Ferrari ^{118,117}, R. Ferrari ^{75a}, D. Ferrere ⁵⁸, C. Ferretti ¹⁰⁹, D. Fiacco ^{77a,77b}, F. Fiedler ¹⁰³, P. Fiedler ¹³⁶, S. Filimonov ³⁹, A. Filipčič ⁹⁶, E.K. Filmer ^{160a}, F. Filthaut ¹¹⁷, M.C.N. Fiolhais ^{134a,134c,c}, L. Fiorini ¹⁶⁸, W.C. Fisher ¹¹⁰, T. Fitschen ¹⁰⁴, P.M. Fitzhugh ¹³⁹, I. Fleck ¹⁴⁶, P. Fleischmann ¹⁰⁹, T. Flick ¹⁷⁶, M. Flores ^{34d,ab}, L.R. Flores Castillo ^{66a}, L. Flores Sanz De Acedo ³⁷, F.M. Follega ^{80a,80b}, N. Fomin ³³, J.H. Foo ¹⁵⁹, A. Formica ¹³⁹, A.C. Forti ¹⁰⁴, E. Fortin ³⁷, A.W. Fortman ^{18a}, M.G. Foti ^{18a}, L. Fountas ^{9j}, D. Fournier ⁶⁸, H. Fox ⁹⁴, P. Francavilla ^{76a,76b}, S. Francescato ⁶³, S. Franchellucci ⁵⁸, M. Franchini ^{24b,24a}, S. Franchino ^{65a}, D. Francis ³⁷, L. Franco ¹¹⁷, V. Franco Lima ³⁷, L. Franconi ⁵⁰, M. Franklin ⁶³, G. Frattari ²⁷, Y.Y. Frid ¹⁵⁶, J. Friend ⁶¹, N. Fritzsche ³⁷, A. Froch ⁵⁶, D. Froidevaux ³⁷, J.A. Frost ¹³⁰, Y. Fu ^{64a}, S. Fuenzalida Garrido ^{141f}, M. Fujimoto ¹⁰⁵, K.Y. Fung ^{66a}, E. Furtado De Simas Filho ^{85e}, M. Furukawa ¹⁵⁸, J. Fuster ¹⁶⁸, A. Gaa ⁵⁷, A. Gabrielli ^{24b,24a}, A. Gabrielli ¹⁵⁹, P. Gadow ³⁷, G. Gagliardi ^{59b,59a}, L.G. Gagnon ^{18a}, S. Gaid ¹⁶⁵, S. Galantzan ¹⁵⁶, J. Gallagher ¹, E.J. Gallas ¹³⁰, B.J. Gallop ¹³⁸, K.K. Gan ¹²³, S. Ganguly ¹⁵⁸, Y. Gao ⁵⁴, F.M. Garay Walls ^{141a,141b}, B. Garcia ³⁰, C. García ¹⁶⁸, A. Garcia Alonso ¹¹⁸, A.G. Garcia Caffaro ¹⁷⁷, J.E. García Navarro ¹⁶⁸, M. Garcia-Sciveres ^{18a}, G.L. Gardner ¹³², R.W. Gardner ⁴¹, N. Garelli ¹⁶², D. Garg ⁸², R.B. Garg ¹⁴⁸, J.M. Gargan ⁵⁴, C.A. Garner ¹⁵⁹, C.M. Garvey ^{34a}, V.K. Gassmann ¹⁶², G. Gaudio ^{75a}, V. Gautam ¹³, P. Gauzzi ^{77a,77b}, J. Gavranovic ⁹⁶, I.L. Gavrilenko ³⁹, A. Gavrilyuk ³⁹, C. Gay ¹⁶⁹, G. Gaycken ¹²⁷, E.N. Gazis ¹⁰, A.A. Geanta ^{28b}, C.M. Gee ¹⁴⁰, A. Gekow ¹²³, C. Gemme ^{59b}, M.H. Genest ⁶², A.D. Gentry ¹¹⁶, S. George ⁹⁸, W.F. George ²¹, T. Gerialis ⁴⁸, P. Gessinger-Befurt ³⁷, M.E. Geyik ¹⁷⁶, M. Ghani ¹⁷², K. Ghorbanian ⁹⁷, A. Ghosal ¹⁴⁶, A. Ghosh ¹⁶³, A. Ghosh ⁷, B. Giacobbe ^{24b}, S. Giagu ^{77a,77b}, T. Giani ¹¹⁸, A. Giannini ^{64a}, S.M. Gibson ⁹⁸, M. Gignac ¹⁴⁰, D.T. Gil ^{88b}, A.K. Gilbert ^{88a}, B.J. Gilbert ⁴³, D. Gillberg ³⁵, G. Gilles ¹¹⁸, L. Ginabat ¹³¹, D.M. Gingrich ^{2,ae}, M.P. Giordani ^{71a,71c}, P.F. Giraud ¹³⁹, G. Giugliarelli ^{71a,71c}, D. Giugni ^{73a}, F. Giuli ^{78a,78b}, I. Gkialas ^{9j}, L.K. Gladilin ³⁹, C. Glasman ¹⁰², G.R. Gledhill ¹²⁷, G. Glemža ⁵⁰, M. Glisic ¹²⁷, I. Gnesi ^{45b}, Y. Go ³⁰, M. Goblirsch-Kolb ³⁷, B. Gocke ⁵¹, D. Godin ¹¹¹, B. Gokturk ^{22a}, S. Goldfarb ¹⁰⁸, T. Golling ⁵⁸, M.G.D. Gololo ^{34g}, D. Golubkov ³⁹, J.P. Gombas ¹¹⁰, A. Gomes ^{134a,134b}, G. Gomes Da Silva ¹⁴⁶, A.J. Gomez Delegido ¹⁶⁸, R. Gonçalves ^{134a}, L. Gonella ²¹, A. Gongadze ^{154c}, F. Gonnella ²¹, J.L. Gonski ¹⁴⁸, R.Y. González Andana ⁵⁴, S. González de la Hoz ¹⁶⁸, R. Gonzalez Lopez ⁹⁵, C. Gonzalez Renteria ^{18a}, M.V. Gonzalez Rodrigues ⁵⁰, R. Gonzalez Suarez ¹⁶⁶, S. Gonzalez-Sevilla ⁵⁸, L. Goossens ³⁷, B. Gorini ³⁷, E. Gorini ^{72a,72b}, A. Gorišek ⁹⁶, T.C. Gosart ¹³², A.T. Goshaw ⁵³, M.I. Gostkin ⁴⁰, S. Goswami ¹²⁵, C.A. Gottardo ³⁷, S.A. Gotz ¹¹², M. Goughri ^{36b}, V. Goumarre ⁵⁰, A.G. Goussiou ¹⁴³, N. Govender ^{34c}, R.P. Grabarczyk ¹³⁰, I. Grabowska-Bold ^{88a}, K. Graham ³⁵, E. Gramstad ¹²⁹,

S. Grancagnolo ^{72a,72b}, C.M. Grant ^{1,139}, P.M. Gravila ^{28f}, F.G. Gravili ^{72a,72b}, H.M. Gray ^{18a}, M. Greco ^{72a,72b}, M.J. Green ¹, C. Grefe ²⁵, A.S. Grefsrud ¹⁷, I.M. Gregor ⁵⁰, K.T. Greif ¹⁶³, P. Grenier ¹⁴⁸, S.G. Grewe ¹¹³, A.A. Grillo ¹⁴⁰, K. Grimm ³², S. Grinstein ^{13,u}, J.-F. Grivaz ⁶⁸, E. Gross ¹⁷⁴, J. Grosse-Knetter ⁵⁷, L. Guan ¹⁰⁹, J.G.R. Guerrero Rojas ¹⁶⁸, G. Guerrieri ³⁷, R. Gugel ¹⁰³, J.A.M. Guhit ¹⁰⁹, A. Guida ¹⁹, E. Guilloton ¹⁷², S. Guindon ³⁷, F. Guo ^{14,115c}, J. Guo ^{64c}, L. Guo ⁵⁰, L. Guo ¹⁴, Y. Guo ¹⁰⁹, A. Gupta ⁵¹, R. Gupta ¹³³, S. Gurbuz ²⁵, S.S. Gurdasani ⁵⁶, G. Gustavino ^{77a,77b}, P. Gutierrez ¹²⁴, L.F. Gutierrez Zagazeta ¹³², M. Gutsche ⁵², C. Gutschow ⁹⁹, C. Gwenlan ¹³⁰, C.B. Gwilliam ⁹⁵, E.S. Haaland ¹²⁹, A. Haas ¹²¹, M. Habedank ⁶¹, C. Haber ^{18a}, H.K. Hadavand ⁸, A. Hadeef ⁵², S. Hadzic ¹¹³, A.I. Hagan ⁹⁴, J.J. Hahn ¹⁴⁶, E.H. Haines ⁹⁹, M. Haleem ¹⁷¹, J. Haley ¹²⁵, G.D. Hallowell ¹⁰⁵, L. Halser ²⁰, K. Hamano ¹⁷⁰, M. Hamer ²⁵, E.J. Hampshire ⁹⁸, J. Han ^{64b}, L. Han ^{115a}, L. Han ^{64a}, S. Han ^{18a}, Y.F. Han ¹⁵⁹, K. Hanagaki ⁸⁶, M. Hance ¹⁴⁰, D.A. Hangal ⁴³, H. Hanif ¹⁴⁷, M.D. Hank ¹³², J.B. Hansen ⁴⁴, P.H. Hansen ⁴⁴, D. Harada ⁵⁸, T. Harenberg ¹⁷⁶, S. Harkusha ¹⁷⁸, M.L. Harris ¹⁰⁶, Y.T. Harris ²⁵, J. Harrison ¹³, N.M. Harrison ¹²³, P.F. Harrison ¹⁷², N.M. Hartman ¹¹³, N.M. Hartmann ¹¹², R.Z. Hasan ^{98,138}, Y. Hasegawa ¹⁴⁵, F. Haslbeck ¹³⁰, S. Hassan ¹⁷, R. Hauser ¹¹⁰, C.M. Hawkes ²¹, R.J. Hawkins ³⁷, Y. Hayashi ¹⁵⁸, D. Hayden ¹¹⁰, C. Hayes ¹⁰⁹, R.L. Hayes ¹¹⁸, C.P. Hays ¹³⁰, J.M. Hays ⁹⁷, H.S. Hayward ⁹⁵, F. He ^{64a}, M. He ^{14,115c}, Y. He ⁵⁰, Y. He ⁹⁹, N.B. Heatley ⁹⁷, V. Hedberg ¹⁰¹, A.L. Heggelund ¹²⁹, N.D. Hehir ^{97,*}, C. Heidegger ⁵⁶, K.K. Heidegger ⁵⁶, J. Heilman ³⁵, S. Heim ⁵⁰, T. Heim ^{18a}, J.G. Heinlein ¹³², J.J. Heinrich ¹²⁷, L. Heinrich ^{113,ac}, J. Hejbal ¹³⁵, A. Held ¹⁷⁵, S. Hellesund ¹⁷, C.M. Helling ¹⁶⁹, S. Hellman ^{49a,49b}, R.C.W. Henderson ⁹⁴, L. Henkelmann ³³, A.M. Henriques Correia ³⁷, H. Herde ¹⁰¹, Y. Hernández Jiménez ¹⁵⁰, L.M. Herrmann ²⁵, T. Herrmann ⁵², G. Herten ⁵⁶, R. Hertenberger ¹¹², L. Hervas ³⁷, M.E. Hesping ¹⁰³, N.P. Hessey ^{160a}, J. Hessler ¹¹³, M. Hidaoui ^{36b}, N. Hidic ¹³⁷, E. Hill ¹⁵⁹, S.J. Hillier ²¹, J.R. Hinds ¹¹⁰, F. Hinterkeuser ²⁵, M. Hirose ¹²⁸, S. Hirose ¹⁶¹, D. Hirschbuehl ¹⁷⁶, T.G. Hitchings ¹⁰⁴, B. Hiti ⁹⁶, J. Hobbs ¹⁵⁰, R. Hobincu ^{28e}, N. Hod ¹⁷⁴, M.C. Hodgkinson ¹⁴⁴, B.H. Hodgkinson ¹³⁰, A. Hoecker ³⁷, D.D. Hofer ¹⁰⁹, J. Hofer ¹⁶⁸, T. Holm ²⁵, M. Holzbock ³⁷, L.B.A.H. Hommels ³³, B.P. Honan ¹⁰⁴, J.J. Hong ⁷⁰, J. Hong ^{64c}, T.M. Hong ¹³³, B.H. Hooberman ¹⁶⁷, W.H. Hopkins ⁶, M.C. Hoppesch ¹⁶⁷, Y. Horii ¹¹⁴, M.E. Horstmann ¹¹³, S. Hou ¹⁵³, M.R. Housenga ¹⁶⁷, A.S. Howard ⁹⁶, J. Howarth ⁶¹, J. Hoya ⁶, M. Hrabovsky ¹²⁶, A. Hrynevich ⁵⁰, T. Hryn'ova ⁴, P.J. Hsu ⁶⁷, S.-C. Hsu ¹⁴³, T. Hsu ⁶⁸, M. Hu ^{18a}, Q. Hu ^{64a}, S. Huang ³³, X. Huang ^{14,115c}, Y. Huang ¹⁴⁴, Y. Huang ¹⁰³, Y. Huang ¹⁴, Z. Huang ¹⁰⁴, Z. Hubacek ¹³⁶, M. Huebner ²⁵, F. Huegging ²⁵, T.B. Huffman ¹³⁰, M. Hufnagel Maranha De Faria ^{85a}, C.A. Hugli ⁵⁰, M. Huhtinen ³⁷, S.K. Huiberts ¹⁷, R. Hulsken ¹⁰⁷, N. Huseynov ^{12,g}, J. Huston ¹¹⁰, J. Huth ⁶³, R. Hyneman ¹⁴⁸, G. Iacobucci ⁵⁸, G. Iakovidis ³⁰, L. Iconomidou-Fayard ⁶⁸, J.P. Iddon ³⁷, P. Iengo ^{74a,74b}, R. Iguchi ¹⁵⁸, Y. Iiyama ¹⁵⁸, T. Iizawa ¹³⁰, Y. Ikegami ⁸⁶, N. Ilic ¹⁵⁹, H. Imam ^{85c}, G. Inacio Goncalves ^{85d}, T. Ingebretsen Carlson ^{49a,49b}, J.M. Inglis ⁹⁷, G. Introzzi ^{75a,75b}, M. Iodice ^{79a}, V. Ippolito ^{77a,77b}, R.K. Irwin ⁹⁵, M. Ishino ¹⁵⁸, W. Islam ¹⁷⁵, C. Issever ¹⁹, S. Istin ^{22a,ai}, H. Ito ¹⁷³, R. Iuppa ^{80a,80b}, A. Ivina ¹⁷⁴, J.M. Izen ⁴⁷, V. Izzo ^{74a}, P. Jacka ¹³⁵, P. Jackson ¹, C.S. Jagfeld ¹¹², G. Jain ^{160a}, P. Jain ⁵⁰, K. Jakobs ⁵⁶, T. Jakoubek ¹⁷⁴, J. Jamieson ⁶¹, W. Jang ¹⁵⁸, M. Javurkova ¹⁰⁶, P. Jawahar ¹⁰⁴, L. Jeanty ¹²⁷, J. Jejelava ^{154a}, P. Jenni ^{56,f}, C.E. Jessiman ³⁵, C. Jia ^{64b}, H. Jia ¹⁶⁹, J. Jia ¹⁵⁰, X. Jia ^{14,115c}, Z. Jia ^{115a}, C. Jiang ⁵⁴, S. Jiggins ⁵⁰, J. Jimenez Pena ¹³, S. Jin ^{115a}, A. Jinaru ^{28b}, O. Jinnouchi ¹⁴², P. Johansson ¹⁴⁴, K.A. Johns ⁷, J.W. Johnson ¹⁴⁰, F.A. Jolly ⁵⁰, D.M. Jones ¹⁵¹, E. Jones ⁵⁰, K.S. Jones ⁸, P. Jones ³³, R.W.L. Jones ⁹⁴, T.J. Jones ⁹⁵, H.L. Joos ^{57,37}, R. Joshi ¹²³, J. Jovicevic ¹⁶, X. Ju ^{18a}, J.J. Junggeburth ³⁷, T. Junkermann ^{65a}, A. Juste Rozas ^{13,u}, M.K. Juzek ⁸⁹,

S. Kabana ^{141e}, A. Kaczmarzka ⁸⁹, M. Kado ¹¹³, H. Kagan ¹²³, M. Kagan ¹⁴⁸, A. Kahn ¹³², C. Kahra ¹⁰³, T. Kaji ¹⁵⁸, E. Kajomovitz ¹⁵⁵, N. Kakati ¹⁷⁴, I. Kalaitzidou ⁵⁶, C.W. Kalderon ³⁰, N.J. Kang ¹⁴⁰, D. Kar ^{34g}, K. Karava ¹³⁰, M.J. Kareem ^{160b}, E. Karentzos ²⁵, O. Karkout ¹¹⁸, S.N. Karpov ⁴⁰, Z.M. Karpova ⁴⁰, V. Kartvelishvili ⁹⁴, A.N. Karyukhin ³⁹, E. Kasimi ¹⁵⁷, J. Katzy ⁵⁰, S. Kaur ³⁵, K. Kawade ¹⁴⁵, M.P. Kawale ¹²⁴, C. Kawamoto ⁹⁰, T. Kawamoto ^{64a}, E.F. Kay ³⁷, F.I. Kaya ¹⁶², S. Kazakos ¹¹⁰, V.F. Kazanin ³⁹, Y. Ke ¹⁵⁰, J.M. Keaveney ^{34a}, R. Keeler ¹⁷⁰, G.V. Kehris ⁶³, J.S. Keller ³⁵, J.J. Kempster ¹⁵¹, O. Kepka ¹³⁵, B.P. Kerridge ¹³⁸, S. Kersten ¹⁷⁶, B.P. Kerševan ⁹⁶, L. Keszeghova ^{29a}, S. Ketabchi Haghighat ¹⁵⁹, R.A. Khan ¹³³, A. Khanov ¹²⁵, A.G. Kharlamov ³⁹, T. Kharlamova ³⁹, E.E. Khoda ¹⁴³, M. Kholodenko ^{134a}, T.J. Khoo ¹⁹, G. Khorialuli ¹⁷¹, J. Khubua ^{154b,*}, Y.A.R. Khwaira ¹³¹, B. Kibirige ^{34g}, D. Kim ⁶, D.W. Kim ^{49a,49b}, Y.K. Kim ⁴¹, N. Kimura ⁹⁹, M.K. Kingston ⁵⁷, A. Kirchhoff ⁵⁷, C. Kirfel ²⁵, F. Kirfel ²⁵, J. Kirk ¹³⁸, A.E. Kiryunin ¹¹³, S. Kita ¹⁶¹, C. Kitsaki ¹⁰, O. Kivernyk ²⁵, M. Klassen ¹⁶², C. Klein ³⁵, L. Klein ¹⁷¹, M.H. Klein ⁴⁶, S.B. Klein ⁵⁸, U. Klein ⁹⁵, A. Klimentov ³⁰, T. Klioutchnikova ³⁷, P. Kluit ¹¹⁸, S. Kluth ¹¹³, E. Kneringer ⁸¹, T.M. Knight ¹⁵⁹, A. Knue ⁵¹, M. Kobel ⁵², D. Kobylanskii ¹⁷⁴, S.F. Koch ¹³⁰, M. Kocian ¹⁴⁸, P. Kodyš ¹³⁷, D.M. Koeck ¹²⁷, P.T. Koenig ²⁵, T. Koffas ³⁵, O. Kolay ⁵², I. Koletsou ⁴, T. Komarek ⁸⁹, K. Köneke ⁵⁶, A.X.Y. Kong ¹, T. Kono ¹²², N. Konstantinidis ⁹⁹, P. Kontaxakis ⁵⁸, B. Konya ¹⁰¹, R. Kopeliansky ⁴³, S. Koperny ^{88a}, K. Korcyl ⁸⁹, K. Kordas ^{157,e}, A. Korn ⁹⁹, S. Korn ⁵⁷, I. Korolkov ¹³, N. Korotkova ³⁹, B. Kortman ¹¹⁸, O. Kortner ¹¹³, S. Kortner ¹¹³, W.H. Kostecka ¹¹⁹, V.V. Kostyukhin ¹⁴⁶, A. Kotsokechagia ³⁷, A. Kotwal ⁵³, A. Koulouris ³⁷, A. Kourkoumeli-Charalampidi ^{75a,75b}, C. Kourkoumelis ⁹, E. Kourlitis ¹¹³, O. Kovanda ¹²⁷, R. Kowalewski ¹⁷⁰, W. Kozanecki ¹²⁷, A.S. Kozhin ³⁹, V.A. Kramarenko ³⁹, G. Kramberger ⁹⁶, P. Kramer ²⁵, M.W. Krasny ¹³¹, A. Krasznahorkay ³⁷, A.C. Kraus ¹¹⁹, J.W. Kraus ¹⁷⁶, J.A. Kremer ⁵⁰, T. Kresse ⁵², L. Kretschmann ¹⁷⁶, J. Kretschmar ⁹⁵, K. Kreul ¹⁹, P. Krieger ¹⁵⁹, M. Krivos ¹³⁷, K. Krizka ²¹, K. Kroeninger ⁵¹, H. Kroha ¹¹³, J. Kroll ¹³⁵, J. Kroll ¹³², K.S. Krowpman ¹¹⁰, U. Kruchonak ⁴⁰, H. Krüger ²⁵, N. Krumnack ⁸³, M.C. Kruse ⁵³, O. Kuchinskaia ³⁹, S. Kuday ^{3a}, S. Kuehn ³⁷, R. Kuesters ⁵⁶, T. Kuhl ⁵⁰, V. Kukhtin ⁴⁰, Y. Kulchitsky ⁴⁰, S. Kuleshov ^{141d,141b}, M. Kumar ^{34g}, N. Kumari ⁵⁰, P. Kumari ^{160b}, A. Kupco ¹³⁵, T. Kupfer ⁵¹, A. Kupich ³⁹, O. Kuprash ⁵⁶, H. Kurashige ⁸⁷, L.L. Kurchaninov ^{160a}, O. Kurdysh ⁵⁸, Y.A. Kurochkin ³⁸, A. Kurova ³⁹, M. Kuze ¹⁴², A.K. Kvam ¹⁰⁶, J. Kvita ¹²⁶, T. Kwan ¹⁰⁷, N.G. Kyriacou ¹⁰⁹, L.A.O. Laatu ¹⁰⁵, C. Lacasta ¹⁶⁸, F. Lacava ^{77a,77b}, H. Lacker ¹⁹, D. Lacour ¹³¹, N.N. Lad ⁹⁹, E. Ladygin ⁴⁰, A. Lafarge ⁴², B. Laforge ¹³¹, T. Lagouri ¹⁷⁷, F.Z. Lahbabi ^{36a}, S. Lai ⁵⁷, J.E. Lambert ¹⁷⁰, S. Lammers ⁷⁰, W. Lampl ⁷, C. Lampoudis ^{157,e}, G. Lamprinoudis ¹⁰³, A.N. Lancaster ¹¹⁹, E. Lançon ³⁰, U. Landgraf ⁵⁶, M.P.J. Landon ⁹⁷, V.S. Lang ⁵⁶, O.K.B. Langrekken ¹²⁹, A.J. Lankford ¹⁶³, F. Lanni ³⁷, K. Lantzsch ²⁵, A. Lanza ^{75a}, M. Lanzac Berrocal ¹⁶⁸, J.F. Laporte ¹³⁹, T. Lari ^{73a}, F. Lasagni Manghi ^{24b}, M. Lassnig ³⁷, V. Latonova ¹³⁵, A. Laurier ¹⁵⁵, S.D. Lawlor ¹⁴⁴, Z. Lawrence ¹⁰⁴, R. Lazaridou ¹⁷², M. Lazzaroni ^{73a,73b}, B. Le ¹⁰⁴, H.D.M. Le ¹¹⁰, E.M. Le Boulicaut ¹⁷⁷, L.T. Le Pottier ^{18a}, B. Leban ^{24b,24a}, A. Lebedev ⁸³, M. LeBlanc ¹⁰⁴, F. Ledroit-Guillon ⁶², S.C. Lee ¹⁵³, S. Lee ^{49a,49b}, T.F. Lee ⁹⁵, L.L. Leeuw ^{34c}, H.P. Lefebvre ⁹⁸, M. Lefebvre ¹⁷⁰, C. Leggett ^{18a}, G. Lehmann Miotto ³⁷, M. Leigh ⁵⁸, W.A. Leight ¹⁰⁶, W. Leinonen ¹¹⁷, A. Leisos ^{157,s}, M.A.L. Leite ^{85c}, C.E. Leitgeb ¹⁹, R. Leitner ¹³⁷, K.J.C. Leney ⁴⁶, T. Lenz ²⁵, S. Leone ^{76a}, C. Leonidopoulos ⁵⁴, A. Leopold ¹⁴⁹, R. Les ¹¹⁰, C.G. Lester ³³, M. Levchenko ³⁹, J. Levêque ⁴, L.J. Levinson ¹⁷⁴, G. Levrimi ^{24b,24a}, M.P. Lewicki ⁸⁹, C. Lewis ¹⁴³, D.J. Lewis ⁴, L. Lewitt ¹⁴⁴, A. Li ³⁰, B. Li ^{64b}, C. Li ^{64a}, C-Q. Li ¹¹³, H. Li ^{64a}, H. Li ^{64b}, H. Li ^{115a}, H. Li ¹⁵, H. Li ^{64b}, J. Li ^{64c}, K. Li ¹⁴, L. Li ^{64c}, M. Li ^{14,115c}, S. Li ^{14,115c}, S. Li ^{64d,64c,d}, T. Li ⁵, X. Li ¹⁰⁷, Z. Li ¹⁵⁸, Z. Li ^{14,115c}, Z. Li ^{64a},

S. Liang ^{14,115c}, Z. Liang ¹⁴, M. Liberatore ¹³⁹, B. Liberti ^{78a}, K. Lie ^{66c}, J. Lieber Marin ^{85e}, H. Lien ⁷⁰, H. Lin ¹⁰⁹, K. Lin ¹¹⁰, L. Linden ¹¹², R.E. Lindley ⁷, J.H. Lindon ², J. Ling ⁶³, E. Lipeles ¹³², A. Lipniacka ¹⁷, A. Lister ¹⁶⁹, J.D. Little ⁷⁰, B. Liu ¹⁴, B.X. Liu ^{115b}, D. Liu ^{64d,64c}, E.H.L. Liu ²¹, J.B. Liu ^{64a}, J.K.K. Liu ³³, K. Liu ^{64d}, K. Liu ^{64d,64c}, M. Liu ^{64a}, M.Y. Liu ^{64a}, P. Liu ¹⁴, Q. Liu ^{64d,143,64c}, X. Liu ^{64a}, X. Liu ^{64b}, Y. Liu ^{115b,115c}, Y.L. Liu ^{64b}, Y.W. Liu ^{64a}, S.L. Lloyd ⁹⁷, E.M. Lobodzinska ⁵⁰, P. Loch ⁷, E. Lodhi ¹⁵⁹, T. Lohse ¹⁹, K. Lohwasser ¹⁴⁴, E. Loiacono ⁵⁰, J.D. Lomas ²¹, J.D. Long ⁴³, I. Longarini ¹⁶³, R. Longo ¹⁶⁷, I. Lopez Paz ⁶⁹, A. Lopez Solis ⁵⁰, N.A. Lopez-canelas ⁷, N. Lorenzo Martinez ⁴, A.M. Lory ¹¹², M. Losada ^{120a}, G. Löschecke Centeno ¹⁵¹, O. Loseva ³⁹, X. Lou ^{49a,49b}, X. Lou ^{14,115c}, A. Lounis ⁶⁸, P.A. Love ⁹⁴, G. Lu ^{14,115c}, M. Lu ⁶⁸, S. Lu ¹³², Y.J. Lu ⁶⁷, H.J. Lubatti ¹⁴³, C. Luci ^{77a,77b}, F.L. Lucio Alves ^{115a}, F. Luehring ⁷⁰, O. Lukianchuk ⁶⁸, B.S. Lunday ¹³², O. Lundberg ¹⁴⁹, B. Lund-Jensen ^{149,*}, N.A. Luongo ⁶, M.S. Lutz ³⁷, A.B. Lux ²⁶, D. Lynn ³⁰, R. Lysak ¹³⁵, E. Lytken ¹⁰¹, V. Lyubushkin ⁴⁰, T. Lyubushkina ⁴⁰, M.M. Lyukova ¹⁵⁰, M.Firdaus M. Soberi ⁵⁴, H. Ma ³⁰, K. Ma ^{64a}, L.L. Ma ^{64b}, W. Ma ^{64a}, Y. Ma ¹²⁵, J.C. MacDonald ¹⁰³, P.C. Machado De Abreu Farias ^{85e}, R. Madar ⁴², T. Madula ⁹⁹, J. Maeda ⁸⁷, T. Maeno ³⁰, H. Maguire ¹⁴⁴, V. Maiboroda ¹³⁹, A. Maio ^{134a,134b,134d}, K. Maj ^{88a}, O. Majersky ⁵⁰, S. Majewski ¹²⁷, N. Makovec ⁶⁸, V. Maksimovic ¹⁶, B. Malaescu ¹³¹, Pa. Malecki ⁸⁹, V.P. Maleev ³⁹, F. Malek ^{62,n}, M. Mali ⁹⁶, D. Malito ⁹⁸, U. Mallik ^{82,*}, S. Maltezos ¹⁰, S. Malyukov ⁴⁰, J. Mamuzic ¹³, G. Mancini ⁵⁵, M.N. Mancini ²⁷, G. Manco ^{75a,75b}, J.P. Mandalia ⁹⁷, S.S. Mandarray ¹⁵¹, I. Mandić ⁹⁶, L. Manhaes de Andrade Filho ^{85a}, I.M. Maniatis ¹⁷⁴, J. Manjarres Ramos ⁹², D.C. Mankad ¹⁷⁴, A. Mann ¹¹², S. Manzoni ³⁷, L. Mao ^{64c}, X. Mapekula ^{34c}, A. Marantis ^{157,s}, G. Marchiori ⁵, M. Marcisovsky ¹³⁵, C. Marcon ^{73a}, M. Marinescu ²¹, S. Marium ⁵⁰, M. Marjanovic ¹²⁴, A. Markhoos ⁵⁶, M. Markovitch ⁶⁸, M.K. Maroun ¹⁰⁶, E.J. Marshall ⁹⁴, Z. Marshall ^{18a}, S. Marti-Garcia ¹⁶⁸, J. Martin ⁹⁹, T.A. Martin ¹³⁸, V.J. Martin ⁵⁴, B. Martin dit Latour ¹⁷, L. Martinelli ^{77a,77b}, M. Martinez ^{13,u}, P. Martinez Agullo ¹⁶⁸, V.I. Martinez Outschoorn ¹⁰⁶, P. Martinez Suarez ¹³, S. Martin-Haugh ¹³⁸, G. Martinovicova ¹³⁷, V.S. Martoiu ^{28b}, A.C. Martyniuk ⁹⁹, A. Marzin ³⁷, D. Mascione ^{80a,80b}, L. Masetti ¹⁰³, J. Masik ¹⁰⁴, A.L. Maslennikov ³⁹, S.L. Mason ⁴³, P. Massarotti ^{74a,74b}, P. Mastrandrea ^{76a,76b}, A. Mastroberardino ^{45b,45a}, T. Masubuchi ¹²⁸, T.T. Mathew ¹²⁷, T. Mathisen ¹⁶⁶, J. Matousek ¹³⁷, D.M. Mattern ⁵¹, J. Maurer ^{28b}, T. Maurin ⁶¹, A.J. Maury ⁶⁸, B. Maček ⁹⁶, D.A. Maximov ³⁹, A.E. May ¹⁰⁴, R. Mazini ^{34g}, I. Maznas ¹¹⁹, M. Mazza ¹¹⁰, S.M. Mazza ¹⁴⁰, E. Mazzeo ^{73a,73b}, C. Mc Ginn ³⁰, J.P. Mc Gowan ¹⁷⁰, S.P. Mc Kee ¹⁰⁹, C.A. Mc Lean ⁶, C.C. McCracken ¹⁶⁹, E.F. McDonald ¹⁰⁸, A.E. McDougall ¹¹⁸, J.A. Mcfayden ¹⁵¹, R.P. McGovern ¹³², R.P. Mckenzie ^{34g}, T.C. McLachlan ⁵⁰, D.J. McLaughlin ⁹⁹, S.J. McMahon ¹³⁸, C.M. Mcpartland ⁹⁵, R.A. McPherson ^{170,y}, S. Mehlhase ¹¹², A. Mehta ⁹⁵, D. Melini ¹⁶⁸, B.R. Mellado Garcia ^{34g}, A.H. Melo ⁵⁷, F. Meloni ⁵⁰, A.M. Mendes Jacques Da Costa ¹⁰⁴, H.Y. Meng ¹⁵⁹, L. Meng ⁹⁴, S. Menke ¹¹³, M. Mentink ³⁷, E. Meoni ^{45b,45a}, G. Mercado ¹¹⁹, S. Merianos ¹⁵⁷, C. Merlassino ^{71a,71c}, L. Merola ^{74a,74b}, C. Meroni ^{73a,73b}, J. Metcalfe ⁶, A.S. Mete ⁶, E. Meuser ¹⁰³, C. Meyer ⁷⁰, J-P. Meyer ¹³⁹, R.P. Middleton ¹³⁸, L. Mijović ⁵⁴, G. Mikenberg ¹⁷⁴, M. Mikestikova ¹³⁵, M. Mikuž ⁹⁶, H. Mildner ¹⁰³, A. Milic ³⁷, D.W. Miller ⁴¹, E.H. Miller ¹⁴⁸, L.S. Miller ³⁵, A. Milov ¹⁷⁴, D.A. Milstead ^{49a,49b}, T. Min ^{115a}, A.A. Minaenko ³⁹, I.A. Minashvili ^{154b}, L. Mince ⁶¹, A.I. Mincer ¹²¹, B. Mindur ^{88a}, M. Mineev ⁴⁰, Y. Mino ⁹⁰, L.M. Mir ¹³, M. Miralles Lopez ⁶¹, M. Mironova ^{18a}, M.C. Missio ¹¹⁷, A. Mitra ¹⁷², V.A. Mitsou ¹⁶⁸, Y. Mitsumori ¹¹⁴, O. Miu ¹⁵⁹, P.S. Miyagawa ⁹⁷, T. Mkrtchyan ^{65a}, M. Mlinarevic ⁹⁹, T. Mlinarevic ⁹⁹, M. Mlynarikova ³⁷, S. Mobius ²⁰, P. Mogg ¹¹², M.H. Mohamed Farook ¹¹⁶, A.F. Mohammed ^{14,115c}, S. Mohapatra ⁴³, G. Mokgatitwane ^{34g}, L. Moleri ¹⁷⁴, B. Mondal ¹⁴⁶, S. Mondal ¹³⁶, K. Mönig ⁵⁰,

E. Monnier ¹⁰⁵, L. Monsonis Romero ¹⁶⁸, J. Montejo Berlingen ¹³, A. Montella ^{49a,49b},
M. Montella ¹²³, F. Montereali ^{79a,79b}, F. Monticelli ⁹³, S. Monzani ^{71a,71c}, A. Morancho Tarda ⁴⁴,
N. Morange ⁶⁸, A.L. Moreira De Carvalho ⁵⁰, M. Moreno Llácer ¹⁶⁸, C. Moreno Martinez ⁵⁸,
J.M. Moreno Perez ^{23b}, P. Morettini ^{59b}, S. Morgenstern ³⁷, M. Morii ⁶³, M. Morinaga ¹⁵⁸,
M. Moritsu ⁹¹, F. Morodei ^{77a,77b}, P. Moschovakos ³⁷, B. Moser ¹³⁰, M. Mosidze ^{154b},
T. Moskalets ⁴⁶, P. Moskvitina ¹¹⁷, J. Moss ^{32,k}, P. Moszkowicz ^{88a}, A. Moussa ^{36d},
Y. Moyal ¹⁷⁴, E.J.W. Moyse ¹⁰⁶, O. Mtintsilana ^{34g}, S. Muanza ¹⁰⁵, J. Mueller ¹³³,
D. Muenstermann ⁹⁴, R. Müller ³⁷, G.A. Mullier ¹⁶⁶, A.J. Mullin ³³, J.J. Mullin ¹³², A.E. Mulski ⁶³,
D.P. Mungo ¹⁵⁹, D. Munoz Perez ¹⁶⁸, F.J. Munoz Sanchez ¹⁰⁴, M. Murin ¹⁰⁴, W.J. Murray ^{172,138},
M. Muškinja ⁹⁶, C. Mwewa ³⁰, A.G. Myagkov ^{39,a}, A.J. Myers ⁸, G. Myers ¹⁰⁹, M. Myska ¹³⁶,
B.P. Nachman ^{18a}, O. Nackenhorst ⁵¹, K. Nagai ¹³⁰, K. Nagano ⁸⁶, R. Nagasaka ¹⁵⁸,
J.L. Nagle ^{30,ag}, E. Nagy ¹⁰⁵, A.M. Nairz ³⁷, Y. Nakahama ⁸⁶, K. Nakamura ⁸⁶, K. Nakkalil ⁵,
H. Nanjo ¹²⁸, E.A. Narayanan ⁴⁶, I. Naryshkin ³⁹, L. Nasella ^{73a,73b}, M. Naseri ³⁵, S. Nasri ^{120b},
C. Nass ²⁵, G. Navarro ^{23a}, J. Navarro-Gonzalez ¹⁶⁸, R. Nayak ¹⁵⁶, A. Nayaz ¹⁹,
P.Y. Nechaeva ³⁹, S. Nechaeva ^{24b,24a}, F. Nechansky ¹³⁵, L. Nedic ¹³⁰, T.J. Neep ²¹,
A. Negri ^{75a,75b}, M. Negrini ^{24b}, C. Nellist ¹¹⁸, C. Nelson ¹⁰⁷, K. Nelson ¹⁰⁹, S. Nemecek ¹³⁵,
M. Nessi ^{37,h}, M.S. Neubauer ¹⁶⁷, F. Neuhaus ¹⁰³, J. Neundorff ⁵⁰, J. Newell ⁹⁵, P.R. Newman ²¹,
C.W. Ng ¹³³, Y.W.Y. Ng ⁵⁰, B. Ngair ^{120a}, H.D.N. Nguyen ¹¹¹, R.B. Nickerson ¹³⁰,
R. Nicolaidou ¹³⁹, J. Nielsen ¹⁴⁰, M. Niemeyer ⁵⁷, J. Niermann ⁵⁷, N. Nikiforou ³⁷,
V. Nikolaenko ^{39,a}, I. Nikolic-Audit ¹³¹, K. Nikolopoulos ²¹, P. Nilsson ³⁰, I. Ninca ⁵⁰,
G. Ninio ¹⁵⁶, A. Nisati ^{77a}, N. Nishu ², R. Nisius ¹¹³, N. Nitika ^{71a,71c}, J-E. Nitschke ⁵²,
E.K. Nkadimeng ^{34g}, T. Nobe ¹⁵⁸, T. Nommensen ¹⁵², M.B. Norfolk ¹⁴⁴, B.J. Norman ³⁵,
M. Noury ^{36a}, J. Novak ⁹⁶, T. Novak ⁹⁶, L. Novotny ¹³⁶, R. Novotny ¹¹⁶, L. Nozka ¹²⁶,
K. Ntekas ¹⁶³, N.M.J. Nunes De Moura Junior ^{85b}, J. Ocariz ¹³¹, A. Ochi ⁸⁷, I. Ochoa ^{134a},
S. Oerdek ^{50,v}, J.T. Offermann ⁴¹, A. Ogrodnik ¹³⁷, A. Oh ¹⁰⁴, C.C. Ohm ¹⁴⁹, H. Oide ⁸⁶,
R. Oishi ¹⁵⁸, M.L. Ojeda ³⁷, Y. Okumura ¹⁵⁸, L.F. Oleiro Seabra ^{134a}, I. Oleksiyuk ⁵⁸,
S.A. Olivares Pino ^{141d}, G. Oliveira Correa ¹³, D. Oliveira Damazio ³⁰, J.L. Oliver ¹⁶³,
Ö.O. Öncel ⁵⁶, A.P. O'Neill ²⁰, A. Onofre ^{134a,134e}, P.U.E. Onyisi ¹¹, M.J. Oreglia ⁴¹,
G.E. Orellana ⁹³, D. Orestano ^{79a,79b}, N. Orlando ¹³, R.S. Orr ¹⁵⁹, L.M. Osojnak ¹³²,
R. Ospanov ^{64a}, Y. Osumi ¹¹⁴, G. Otero y Garzon ³¹, H. Otono ⁹¹, P.S. Ott ^{65a}, G.J. Ottino ^{18a},
M. Ouchrif ^{36d}, F. Ould-Saada ¹²⁹, T. Ovsiannikova ¹⁴³, M. Owen ⁶¹, R.E. Owen ¹³⁸,
V.E. Ozcan ^{22a}, F. Ozturk ⁸⁹, N. Ozturk ⁸, S. Ozturk ⁸⁴, H.A. Pacey ¹³⁰, A. Pacheco Pages ¹³,
C. Padilla Aranda ¹³, G. Padovano ^{77a,77b}, S. Pagan Griso ^{18a}, G. Palacino ⁷⁰, A. Palazzo ^{72a,72b},
J. Pampel ²⁵, J. Pan ¹⁷⁷, T. Pan ^{66a}, D.K. Panchal ¹¹, C.E. Pandini ¹¹⁸, J.G. Panduro Vazquez ¹³⁸,
H.D. Pandya ¹, H. Pang ¹⁵, P. Pani ⁵⁰, G. Panizzo ^{71a,71c}, L. Panwar ¹³¹, L. Paolozzi ⁵⁸,
S. Parajuli ¹⁶⁷, A. Paramonov ⁶, C. Paraskevopoulos ⁵⁵, D. Paredes Hernandez ^{66b},
A. Pareti ^{75a,75b}, K.R. Park ⁴³, T.H. Park ¹⁵⁹, M.A. Parker ³³, F. Parodi ^{59b,59a}, E.W. Parrish ¹¹⁹,
V.A. Parrish ⁵⁴, J.A. Parsons ⁴³, U. Parzefall ⁵⁶, B. Pascual Dias ¹¹¹, L. Pascual Dominguez ¹⁰²,
E. Pasqualucci ^{77a}, S. Passaggio ^{59b}, F. Pastore ⁹⁸, P. Patel ⁸⁹, U.M. Patel ⁵³, J.R. Pater ¹⁰⁴,
T. Pauly ³⁷, F. Pauwels ¹³⁷, C.I. Pazos ¹⁶², M. Pedersen ¹²⁹, R. Pedro ^{134a}, S.V. Peleganchuk ³⁹,
O. Penc ³⁷, E.A. Pender ⁵⁴, S. Peng ¹⁵, G.D. Penn ¹⁷⁷, K.E. Penski ¹¹², M. Penzin ³⁹,
B.S. Peralva ^{85d}, A.P. Pereira Peixoto ¹⁴³, L. Pereira Sanchez ¹⁴⁸, D.V. Perepelitsa ^{30,ag},
G. Perera ¹⁰⁶, E. Perez Codina ^{160a}, M. Perganti ¹⁰, H. Pernegger ³⁷, S. Perrella ^{77a,77b},
O. Perrin ⁴², K. Peters ⁵⁰, R.F.Y. Peters ¹⁰⁴, B.A. Petersen ³⁷, T.C. Petersen ⁴⁴, E. Petit ¹⁰⁵,
V. Petousis ¹³⁶, C. Petridou ^{157,e}, T. Petru ¹³⁷, A. Petrukhin ¹⁴⁶, M. Pettee ^{18a}, A. Petukhov ³⁹,
K. Petukhova ³⁷, R. Pezoa ^{141f}, L. Pezzotti ³⁷, G. Pezzullo ¹⁷⁷, A.J. Pfleger ³⁷, T.M. Pham ¹⁷⁵,
T. Pham ¹⁰⁸, P.W. Phillips ¹³⁸, G. Piacquadio ¹⁵⁰, E. Pianori ^{18a}, F. Piazza ¹²⁷, R. Piegai ³¹,

D. Pietreanu ^{id28b}, A.D. Pilkington ^{id104}, M. Pinamonti ^{id71a,71c}, J.L. Pinfeld ^{id2},
B.C. Pinheiro Pereira ^{id134a}, J. Pinol Bel ^{id13}, A.E. Pinto Pinoargote ^{id139,139}, L. Pintucci ^{id71a,71c},
K.M. Piper ^{id151}, A. Pirttikoski ^{id58}, D.A. Pizzi ^{id35}, L. Pizzimento ^{id66b}, A. Pizzini ^{id118},
M.-A. Pleier ^{id30}, V. Pleskot ^{id137}, E. Plotnikova ^{id40}, G. Poddar ^{id97}, R. Poettgen ^{id101}, L. Poggioli ^{id131},
I. Pokharel ^{id57}, S. Polacek ^{id137}, G. Polesello ^{id75a}, A. Poley ^{id147,160a}, A. Polini ^{id24b}, C.S. Pollard ^{id172},
Z.B. Pollock ^{id123}, E. Pompa Pacchi ^{id77a,77b}, N.I. Pond ^{id99}, D. Ponomarenko ^{id70}, L. Pontecorvo ^{id37},
S. Popa ^{id28a}, G.A. Popeneciu ^{id28d}, A. Poreba ^{id37}, D.M. Portillo Quintero ^{id160a}, S. Pospisil ^{id136},
M.A. Postill ^{id144}, P. Postolache ^{id28c}, K. Potamianos ^{id172}, P.A. Potepa ^{id88a}, I.N. Potrap ^{id40},
C.J. Potter ^{id33}, H. Potti ^{id152}, J. Poveda ^{id168}, M.E. Pozo Astigarraga ^{id37}, A. Prades Ibanez ^{id78a,78b},
J. Pretel ^{id170}, D. Price ^{id104}, M. Primavera ^{id72a}, L. Primomo ^{id71a,71c}, M.A. Principe Martin ^{id102},
R. Privara ^{id126}, T. Procter ^{id61}, M.L. Proffitt ^{id143}, N. Proklova ^{id132}, K. Prokofiev ^{id66c}, G. Proto ^{id113},
J. Proudfoot ^{id6}, M. Przybycien ^{id88a}, W.W. Przygoda ^{id88b}, A. Psallidas ^{id48}, J.E. Puddefoot ^{id144},
D. Pudzha ^{id56}, D. Pyatiizbyantseva ^{id39}, J. Qian ^{id109}, R. Qian ^{id110}, D. Qichen ^{id104}, Y. Qin ^{id13},
T. Qiu ^{id54}, A. Quadt ^{id57}, M. Queitsch-Maitland ^{id104}, G. Quetant ^{id58}, R.P. Quinn ^{id169},
G. Rabanal Bolanos ^{id63}, D. Rafanoharana ^{id56}, F. Raffaeli ^{id78a,78b}, F. Ragusa ^{id73a,73b}, J.L. Rainbolt ^{id41},
J.A. Raine ^{id58}, S. Rajagopalan ^{id30}, E. Ramakoti ^{id39}, L. Rambelli ^{id59b,59a}, I.A. Ramirez-Berend ^{id35},
K. Ran ^{id50,115c}, D.S. Rankin ^{id132}, N.P. Rapheeha ^{id34g}, H. Rasheed ^{id28b}, V. Raskina ^{id131},
D.F. Rassloff ^{id65a}, A. Rastogi ^{id18a}, S. Rave ^{id103}, S. Ravera ^{id59b,59a}, B. Ravina ^{id57}, I. Ravinovich ^{id174},
M. Raymond ^{id37}, A.L. Read ^{id129}, N.P. Readioff ^{id144}, D.M. Rebuzzi ^{id75a,75b}, G. Redlinger ^{id30},
A.S. Reed ^{id113}, K. Reeves ^{id27}, J.A. Reidelsturz ^{id176}, D. Reikher ^{id127}, A. Rej ^{id51}, C. Rembser ^{id37},
M. Renda ^{id28b}, F. Renner ^{id50}, A.G. Rennie ^{id163}, A.L. Rescia ^{id50}, S. Resconi ^{id73a},
M. Ressegotti ^{id59b,59a}, S. Rettie ^{id37}, J.G. Reyes Rivera ^{id110}, E. Reynolds ^{id18a}, O.L. Rezanova ^{id39},
P. Reznicek ^{id137}, H. Riani ^{id36d}, N. Ribaric ^{id53}, E. Ricci ^{id80a,80b}, R. Richter ^{id113}, S. Richter ^{id49a,49b},
E. Richter-Was ^{id88b}, M. Ridel ^{id131}, S. Ridouani ^{id36d}, P. Rieck ^{id121}, P. Riedler ^{id37}, E.M. Riefel ^{id49a,49b},
J.O. Rieger ^{id118}, M. Rijssenbeek ^{id150}, M. Rimoldi ^{id37}, L. Rinaldi ^{id24b,24a}, P. Rincke ^{id57},
T.T. Rinn ^{id30}, M.P. Rinnagel ^{id112}, G. Ripellino ^{id166}, I. Riu ^{id13}, J.C. Rivera Vergara ^{id170},
F. Rizatdinova ^{id125}, E. Rizvi ^{id97}, B.R. Roberts ^{id18a}, S.S. Roberts ^{id140}, S.H. Robertson ^{id107,y},
D. Robinson ^{id33}, M. Robles Manzano ^{id103}, A. Robson ^{id61}, A. Rocchi ^{id78a,78b}, C. Roda ^{id76a,76b},
S. Rodriguez Bosca ^{id37}, Y. Rodriguez Garcia ^{id23a}, A. Rodriguez Rodriguez ^{id56},
A.M. Rodríguez Vera ^{id119}, S. Roe ^{id37}, J.T. Roemer ^{id37}, A.R. Roepe-Gier ^{id140}, O. Røhne ^{id129},
R.A. Rojas ^{id37}, C.P.A. Roland ^{id131}, J. Roloff ^{id30}, A. Romanouk ^{id81}, E. Romano ^{id75a,75b},
M. Romano ^{id24b}, A.C. Romero Hernandez ^{id167}, N. Rompotis ^{id95}, L. Roos ^{id131}, S. Rosati ^{id77a},
B.J. Rosser ^{id41}, E. Rossi ^{id130}, E. Rossi ^{id74a,74b}, L.P. Rossi ^{id63}, L. Rossini ^{id56}, R. Rosten ^{id123},
M. Rotaru ^{id28b}, B. Rottler ^{id56}, C. Rougier ^{id92}, D. Rousseau ^{id68}, D. Rousso ^{id50}, A. Roy ^{id167},
S. Roy-Garand ^{id159}, A. Rozanov ^{id105}, Z.M.A. Rozario ^{id61}, Y. Rozen ^{id155}, A. Rubio Jimenez ^{id168},
A.J. Ruby ^{id95}, V.H. Ruelas Rivera ^{id19}, T.A. Ruggeri ^{id1}, A. Ruggiero ^{id130}, A. Ruiz-Martinez ^{id168},
A. Rummler ^{id37}, Z. Rurikova ^{id56}, N.A. Rusakovich ^{id40}, H.L. Russell ^{id170}, G. Russo ^{id77a,77b},
J.P. Rutherford ^{id7}, S. Rutherford Colmenares ^{id33}, M. Rybar ^{id137}, E.B. Rye ^{id129}, A. Ryzhov ^{id46},
J.A. Sabater Iglesias ^{id58}, H.F.W. Sadrozinski ^{id140}, F. Safai Tehrani ^{id77a}, B. Safarzadeh Samani ^{id138},
S. Saha ^{id1}, M. Sahinsoy ^{id84}, A. Saibel ^{id168}, M. Saimpert ^{id139}, M. Saito ^{id158}, T. Saito ^{id158},
A. Sala ^{id73a,73b}, D. Salamani ^{id37}, A. Salnikov ^{id148}, J. Salt ^{id168}, A. Salvador Salas ^{id156},
D. Salvatore ^{id45b,45a}, F. Salvatore ^{id151}, A. Salzburger ^{id37}, D. Sammel ^{id56}, E. Sampson ^{id94},
D. Sampsonidis ^{id157,e}, D. Sampsonidou ^{id127}, J. Sánchez ^{id168}, V. Sanchez Sebastian ^{id168},
H. Sandaker ^{id129}, C.O. Sander ^{id50}, J.A. Sandesara ^{id106}, M. Sandhoff ^{id176}, C. Sandoval ^{id23b},
L. Sanfilippo ^{id65a}, D.P.C. Sankey ^{id138}, T. Sano ^{id90}, A. Sansoni ^{id55}, L. Santi ^{id37,77b}, C. Santoni ^{id42},
H. Santos ^{id134a,134b}, A. Santra ^{id174}, E. Sanzani ^{id24b,24a}, K.A. Saoucha ^{id165}, J.G. Saraiva ^{id134a,134d},
J. Sardain ^{id7}, O. Sasaki ^{id86}, K. Sato ^{id161}, C. Sauer ^{id37}, E. Sauvan ^{id4}, P. Savard ^{id159,ae}, R. Sawada ^{id158},

C. Sawyer ¹³⁸, L. Sawyer ¹⁰⁰, C. Sbarra ^{24b}, A. Sbrizzi ^{24b,24a}, T. Scanlon ⁹⁹,
 J. Schaarschmidt ¹⁴³, U. Schäfer ¹⁰³, A.C. Schaffer ^{68,46}, D. Schaile ¹¹², R.D. Schamberger ¹⁵⁰,
 C. Scharf ¹⁹, M.M. Schefer ²⁰, V.A. Schegelsky ³⁹, D. Scheirich ¹³⁷, M. Schernau ^{141e},
 C. Scheulen ⁵⁷, C. Schiavi ^{59b,59a}, M. Schioppa ^{45b,45a}, B. Schlag ¹⁴⁸, S. Schlenker ³⁷,
 J. Schmeing ¹⁷⁶, M.A. Schmidt ¹⁷⁶, K. Schmieden ¹⁰³, C. Schmitt ¹⁰³, N. Schmitt ¹⁰³,
 S. Schmitt ⁵⁰, L. Schoeffel ¹³⁹, A. Schoening ^{65b}, P.G. Scholer ³⁵, E. Schopf ¹³⁰, M. Schott ²⁵,
 J. Schovancova ³⁷, S. Schramm ⁵⁸, T. Schroer ⁵⁸, H-C. Schultz-Coulon ^{65a}, M. Schumacher ⁵⁶,
 B.A. Schumm ¹⁴⁰, Ph. Schune ¹³⁹, A.J. Schuy ¹⁴³, H.R. Schwartz ¹⁴⁰, A. Schwartzman ¹⁴⁸,
 T.A. Schwarz ¹⁰⁹, Ph. Schwemling ¹³⁹, R. Schwienhorst ¹¹⁰, F.G. Sciaccia ²⁰, A. Sciandra ³⁰,
 G. Sciolla ²⁷, F. Scuri ^{76a}, C.D. Sebastiani ⁹⁵, K. Sedlaczek ¹¹⁹, S.C. Seidel ¹¹⁶, A. Seiden ¹⁴⁰,
 B.D. Seidlitz ⁴³, C. Seitz ⁵⁰, J.M. Seixas ^{85b}, G. Sekhniaidze ^{74a}, L. Selem ⁶²,
 N. Semprini-Cesari ^{24b,24a}, D. Sengupta ⁵⁸, V. Senthilkumar ¹⁶⁸, L. Serin ⁶⁸, M. Sessa ^{78a,78b},
 H. Severini ¹²⁴, F. Sforza ^{59b,59a}, A. Sfyrta ⁵⁸, Q. Sha ¹⁴, E. Shabalina ⁵⁷, A.H. Shah ³³,
 R. Shaheen ¹⁴⁹, J.D. Shahinian ¹³², D. Shaked Renous ¹⁷⁴, L.Y. Shan ¹⁴, M. Shapiro ^{18a},
 A. Sharma ³⁷, A.S. Sharma ¹⁶⁹, P. Sharma ⁸², P.B. Shatalov ³⁹, K. Shaw ¹⁵¹, S.M. Shaw ¹⁰⁴,
 Q. Shen ^{64c}, D.J. Sheppard ¹⁴⁷, P. Sherwood ⁹⁹, L. Shi ⁹⁹, X. Shi ¹⁴, S. Shimizu ⁸⁶,
 C.O. Shimmin ¹⁷⁷, J.D. Shinner ⁹⁸, I.P.J. Shipsey ^{130,*}, S. Shirabe ⁹¹, M. Shiyakova ^{40,w},
 M.J. Shochet ⁴¹, D.R. Shope ¹²⁹, B. Shrestha ¹²⁴, S. Shrestha ^{123,ah}, I. Shreyber ³⁹,
 M.J. Shroff ¹⁷⁰, P. Sicho ¹³⁵, A.M. Sickles ¹⁶⁷, E. Sideras Haddad ^{34g,164}, A.C. Sidley ¹¹⁸,
 A. Sidoti ^{24b}, F. Siegert ⁵², Dj. Sijacki ¹⁶, F. Sili ⁹³, J.M. Silva ⁵⁴, I. Silva Ferreira ^{85b},
 M.V. Silva Oliveira ³⁰, S.B. Silverstein ^{49a}, S. Simion ⁶⁸, R. Simoniello ³⁷, E.L. Simpson ¹⁰⁴,
 H. Simpson ¹⁵¹, L.R. Simpson ¹⁰⁹, S. Simsek ⁸⁴, S. Sindhu ⁵⁷, P. Sinervo ¹⁵⁹, S. Singh ³⁰,
 S. Sinha ⁵⁰, S. Sinha ¹⁰⁴, M. Sioli ^{24b,24a}, I. Siral ³⁷, E. Sitnikova ⁵⁰, J. Sjölin ^{49a,49b},
 A. Skaf ⁵⁷, E. Skorda ²¹, P. Skubic ¹²⁴, M. Slawinska ⁸⁹, V. Smakhtin ¹⁷⁴, B.H. Smart ¹³⁸,
 S.Yu. Smirnov ³⁹, Y. Smirnov ³⁹, L.N. Smirnova ^{39,a}, O. Smirnova ¹⁰¹, A.C. Smith ⁴³,
 D.R. Smith ¹⁶³, E.A. Smith ⁴¹, J.L. Smith ¹⁰⁴, R. Smith ¹⁴⁸, H. Smitmanns ¹⁰³, M. Smizanska ⁹⁴,
 K. Smolek ¹³⁶, A.A. Snesarev ³⁹, H.L. Snoek ¹¹⁸, S. Snyder ³⁰, R. Sobie ^{170,y}, A. Soffer ¹⁵⁶,
 C.A. Solans Sanchez ³⁷, E.Yu. Soldatov ³⁹, U. Soldevila ¹⁶⁸, A.A. Solodkov ³⁹, S. Solomon ²⁷,
 A. Soloshenko ⁴⁰, K. Solovieva ⁵⁶, O.V. Solovyanov ⁴², P. Sommer ⁵², A. Sonay ¹³,
 W.Y. Song ^{160b}, A. Sopczak ¹³⁶, A.L. Sopio ⁵⁴, F. Sopkova ^{29b}, J.D. Sorenson ¹¹⁶,
 I.R. Sotarriva Alvarez ¹⁴², V. Sothilingam ^{65a}, O.J. Soto Sandoval ^{141c,141b}, S. Sottocornola ⁷⁰,
 R. Soualah ¹⁶⁵, Z. Soumami ^{36e}, D. South ⁵⁰, N. Soybelman ¹⁷⁴, S. Spagnolo ^{72a,72b},
 M. Spalla ¹¹³, D. Sperlich ⁵⁶, G. Spigo ³⁷, B. Spisso ^{74a,74b}, D.P. Spiteri ⁶¹, M. Spousta ¹³⁷,
 E.J. Staats ³⁵, R. Stamen ^{65a}, A. Stampekis ²¹, E. Stanecka ⁸⁹, W. Stanek-Maslouska ⁵⁰,
 M.V. Stange ⁵², B. Stanislaus ^{18a}, M.M. Stanitzki ⁵⁰, B. Stapf ⁵⁰, E.A. Starchenko ³⁹,
 G.H. Stark ¹⁴⁰, J. Stark ⁹², P. Staroba ¹³⁵, P. Starovoitov ^{65a}, S. Stärz ¹⁰⁷, R. Staszewski ⁸⁹,
 G. Stavropoulos ⁴⁸, A. Stefl ³⁷, P. Steinberg ³⁰, B. Stelzer ^{147,160a}, H.J. Stelzer ¹³³,
 O. Stelzer-Chilton ^{160a}, H. Stenzel ⁶⁰, T.J. Stevenson ¹⁵¹, G.A. Stewart ³⁷, J.R. Stewart ¹²⁵,
 M.C. Stockton ³⁷, G. Stoicea ^{28b}, M. Stolarski ^{134a}, S. Stonjek ¹¹³, A. Straessner ⁵²,
 J. Strandberg ¹⁴⁹, S. Strandberg ^{49a,49b}, M. Stratmann ¹⁷⁶, M. Strauss ¹²⁴, T. Strebler ¹⁰⁵,
 P. Strizenec ^{29b}, R. Ströhmer ¹⁷¹, D.M. Strom ¹²⁷, R. Stroynowski ⁴⁶, A. Strubig ^{49a,49b},
 S.A. Stucci ³⁰, B. Stugu ¹⁷, J. Stupak ¹²⁴, N.A. Styles ⁵⁰, D. Su ¹⁴⁸, S. Su ^{64a}, W. Su ^{64d},
 X. Su ^{64a}, D. Suchy ^{29a}, K. Sugizaki ¹⁵⁸, V.V. Sulin ³⁹, M.J. Sullivan ⁹⁵, D.M.S. Sultan ¹³⁰,
 L. Sultanaliyeva ³⁹, S. Sultansoy ^{3b}, T. Sumida ⁹⁰, S. Sun ¹⁷⁵, O. Sunneborn Gudnadottir ¹⁶⁶,
 N. Sur ¹⁰⁵, M.R. Sutton ¹⁵¹, H. Suzuki ¹⁶¹, M. Svatos ¹³⁵, M. Swiatlowski ^{160a}, T. Swirski ¹⁷¹,
 I. Sykora ^{29a}, M. Sykora ¹³⁷, T. Sykora ¹³⁷, D. Ta ¹⁰³, K. Tackmann ^{50,v}, A. Taffard ¹⁶³,
 R. Tafirout ^{160a}, J.S. Tafoya Vargas ⁶⁸, Y. Takubo ⁸⁶, M. Talby ¹⁰⁵, A.A. Talyshev ³⁹,

K.C. Tam ^{66b}, N.M. Tamir ¹⁵⁶, A. Tanaka ¹⁵⁸, J. Tanaka ¹⁵⁸, R. Tanaka ⁶⁸, M. Tanasini ¹⁵⁰, Z. Tao ¹⁶⁹, S. Tapia Araya ^{141f}, S. Tapprogge ¹⁰³, A. Tarek Abouelfadl Mohamed ¹¹⁰, S. Tarem ¹⁵⁵, K. Tariq ¹⁴, G. Tarna ^{28b}, G.F. Tartarelli ^{73a}, M.J. Tartarin ⁹², P. Tas ¹³⁷, M. Tasevsky ¹³⁵, E. Tassi ^{45b,45a}, A.C. Tate ¹⁶⁷, G. Tateno ¹⁵⁸, Y. Tayalati ^{36e,x}, G.N. Taylor ¹⁰⁸, W. Taylor ^{160b}, R. Teixeira De Lima ¹⁴⁸, P. Teixeira-Dias ⁹⁸, J.J. Teoh ¹⁵⁹, K. Terashi ¹⁵⁸, J. Terron ¹⁰², S. Terzo ¹³, M. Testa ⁵⁵, R.J. Teuscher ^{159,y}, A. Thaler ⁸¹, O. Theiner ⁵⁸, T. Theveneaux-Pelzer ¹⁰⁵, O. Thielmann ¹⁷⁶, D.W. Thomas ⁹⁸, J.P. Thomas ²¹, E.A. Thompson ^{18a}, P.D. Thompson ²¹, E. Thomson ¹³², R.E. Thornberry ⁴⁶, C. Tian ^{64a}, Y. Tian ⁵⁸, V. Tikhomirov ^{39,a}, Yu.A. Tikhonov ³⁹, S. Timoshenko ³⁹, D. Timoshyn ¹³⁷, E.X.L. Ting ¹, P. Tipton ¹⁷⁷, A. Tishelman-Charny ³⁰, S.H. Tlou ^{34g}, K. Todome ¹⁴², S. Todorova-Nova ¹³⁷, S. Todt ⁵², L. Toffolin ^{71a,71c}, M. Togawa ⁸⁶, J. Tojo ⁹¹, S. Tokár ^{29a}, K. Tokushuku ⁸⁶, O. Toldaiev ⁷⁰, M. Tomoto ^{86,114}, L. Tompkins ^{148,m}, K.W. Topolnicki ^{88b}, E. Torrence ¹²⁷, H. Torres ⁹², E. Torró Pastor ¹⁶⁸, M. Toscani ³¹, C. Toscirci ⁴¹, M. Tost ¹¹, D.R. Tovey ¹⁴⁴, I.S. Trandafir ^{28b}, T. Trefzger ¹⁷¹, A. Tricoli ³⁰, I.M. Trigger ^{160a}, S. Trincas-Duvoid ¹³¹, D.A. Trischuk ²⁷, B. Trocmé ⁶², A. Tropina ⁴⁰, L. Truong ^{34c}, M. Trzebinski ⁸⁹, A. Trzupiek ⁸⁹, F. Tsai ¹⁵⁰, M. Tsai ¹⁰⁹, A. Tsiamis ¹⁵⁷, P.V. Tsiareshka ⁴⁰, S. Tsigaridas ^{160a}, A. Tsigiriotis ^{157,s}, V. Tsiskaridze ¹⁵⁹, E.G. Tskhadadze ^{154a}, M. Tsopoulou ¹⁵⁷, Y. Tsujikawa ⁹⁰, I.I. Tsukerman ³⁹, V. Tsulaia ^{18a}, S. Tsuno ⁸⁶, K. Tsuru ¹²², D. Tsybychev ¹⁵⁰, Y. Tu ^{66b}, A. Tudorache ^{28b}, V. Tudorache ^{28b}, A.N. Tuna ⁶³, S. Turchikhin ^{59b,59a}, I. Turk Cakir ^{3a}, R. Turra ^{73a}, T. Turtuvshin ^{40,z}, P.M. Tuts ⁴³, S. Tzamarias ^{157,e}, E. Tzovara ¹⁰³, F. Ukegawa ¹⁶¹, P.A. Ulloa Poblete ^{141c,141b}, E.N. Umaka ³⁰, G. Unal ³⁷, A. Undrus ³⁰, G. Unel ¹⁶³, J. Urban ^{29b}, P. Urrejola ^{141a}, G. Usai ⁸, R. Ushioda ¹⁴², M. Usman ¹¹¹, F. Ustuner ⁵⁴, Z. Uysal ⁸⁴, V. Vacek ¹³⁶, B. Vachon ¹⁰⁷, T. Vafeiadis ³⁷, A. Vaitkus ⁹⁹, C. Valderanis ¹¹², E. Valdes Santurio ^{49a,49b}, M. Valente ^{160a}, S. Valentinetti ^{24b,24a}, A. Valero ¹⁶⁸, E. Valiente Moreno ¹⁶⁸, A. Vallier ⁹², J.A. Valls Ferrer ¹⁶⁸, D.R. Van Arneman ¹¹⁸, T.R. Van Daalen ¹⁴³, A. Van Der Graaf ⁵¹, P. Van Gemmeren ⁶, M. Van Rijnbach ³⁷, S. Van Stroud ⁹⁹, I. Van Vulpen ¹¹⁸, P. Vana ¹³⁷, M. Vanadia ^{78a,78b}, U.M. Vande Voorde ¹⁴⁹, W. Vandelli ³⁷, E.R. Vandewall ¹²⁵, D. Vannicola ¹⁵⁶, L. Vannoli ⁵⁵, R. Vari ^{77a}, E.W. Varnes ⁷, C. Varni ^{18b}, T. Varol ¹⁵³, D. Varouchas ⁶⁸, L. Varriale ¹⁶⁸, K.E. Varvell ¹⁵², M.E. Vasile ^{28b}, L. Vaslin ⁸⁶, G.A. Vasquez ¹⁷⁰, A. Vasyukov ⁴⁰, L.M. Vaughan ¹²⁵, R. Vavricka ¹⁰³, T. Vazquez Schroeder ³⁷, J. Veatch ³², V. Vecchio ¹⁰⁴, M.J. Veen ¹⁰⁶, I. Veliscek ³⁰, L.M. Veloce ¹⁵⁹, F. Veloso ^{134a,134c}, S. Veneziano ^{77a}, A. Ventura ^{72a,72b}, S. Ventura Gonzalez ¹³⁹, A. Verbitskyi ¹¹³, M. Verducci ^{76a,76b}, C. Vergis ⁹⁷, M. Verissimo De Araujo ^{85b}, W. Verkerke ¹¹⁸, J.C. Vermeulen ¹¹⁸, C. Vernieri ¹⁴⁸, M. Vessella ¹⁰⁶, M.C. Vetterli ^{147,ae}, A. Vgenopoulos ¹⁰³, N. Viaux Maira ^{141f}, T. Vickey ¹⁴⁴, O.E. Vickey Boeriu ¹⁴⁴, G.H.A. Viehhauser ¹³⁰, L. Vigani ^{65b}, M. Vigil ¹¹³, M. Villa ^{24b,24a}, M. Villaplana Perez ¹⁶⁸, E.M. Villhauer ⁵⁴, E. Vilucchi ⁵⁵, M.G. Vincter ³⁵, A. Visibile ¹¹⁸, C. Vittori ³⁷, I. Vivarelli ^{24b,24a}, E. Voevodina ¹¹³, F. Vogel ¹¹², J.C. Voigt ⁵², P. Vokac ¹³⁶, Yu. Volkotrub ^{88b}, E. Von Toerne ²⁵, B. Vormwald ³⁷, V. Vorobel ¹³⁷, K. Vorobev ³⁹, M. Vos ¹⁶⁸, K. Voss ¹⁴⁶, M. Vozak ¹¹⁸, L. Vozdecky ¹²⁴, N. Vranjes ¹⁶, M. Vranjes Milosavljevic ¹⁶, M. Vreeswijk ¹¹⁸, N.K. Vu ^{64d,64c}, R. Vuillermet ³⁷, O. Vujinovic ¹⁰³, I. Vukotic ⁴¹, I.K. Vyas ³⁵, S. Wada ¹⁶¹, C. Wagner ¹⁴⁸, J.M. Wagner ^{18a}, W. Wagner ¹⁷⁶, S. Wahdan ¹⁷⁶, H. Wahlberg ⁹³, C.H. Waits ¹²⁴, J. Walder ¹³⁸, R. Walker ¹¹², W. Walkowiak ¹⁴⁶, A. Wall ¹³², E.J. Wallin ¹⁰¹, T. Wamorkar ⁶, A.Z. Wang ¹⁴⁰, C. Wang ¹⁰³, C. Wang ¹¹, H. Wang ^{18a}, J. Wang ^{66c}, P. Wang ⁹⁹, R. Wang ⁶³, R. Wang ⁶, S.M. Wang ¹⁵³, S. Wang ^{64b}, S. Wang ¹⁴, T. Wang ^{64a}, W.T. Wang ⁸², W. Wang ¹⁴, X. Wang ^{115a}, X. Wang ¹⁶⁷, X. Wang ^{64c}, Y. Wang ^{64d}, Y. Wang ^{115a}, Y. Wang ^{64a}, Z. Wang ¹⁰⁹, Z. Wang ^{64d,53,64c}, Z. Wang ¹⁰⁹, A. Warburton ¹⁰⁷, R.J. Ward ²¹, N. Warrack ⁶¹,

S. Waterhouse ¹⁰⁹⁸, A.T. Watson ¹⁰²¹, H. Watson ¹⁰⁵⁴, M.F. Watson ¹⁰²¹, E. Watton ^{1061,138}, G. Watts ¹⁰¹⁴³, B.M. Waugh ¹⁰⁹⁹, J.M. Webb ¹⁰⁵⁶, C. Weber ¹⁰³⁰, H.A. Weber ¹⁰¹⁹, M.S. Weber ¹⁰²⁰, S.M. Weber ^{1065a}, C. Wei ^{1064a}, Y. Wei ¹⁰⁵⁶, A.R. Weidberg ¹⁰¹³⁰, E.J. Weik ¹⁰¹²¹, J. Weingarten ¹⁰⁵¹, C. Weiser ¹⁰⁵⁶, C.J. Wells ¹⁰⁵⁰, T. Wenaus ¹⁰³⁰, B. Wendland ¹⁰⁵¹, T. Wengler ¹⁰³⁷, N.S. Wenke ¹⁰¹¹³, N. Vermes ¹⁰²⁵, M. Wessels ^{1065a}, A.M. Wharton ¹⁰⁹⁴, A.S. White ¹⁰⁶³, A. White ¹⁰⁸, M.J. White ¹⁰¹, D. Whiteson ¹⁰¹⁶³, L. Wickremasinghe ¹⁰¹²⁸, W. Wiedenmann ¹⁰¹⁷⁵, M. Wielers ¹⁰¹³⁸, C. Wiglesworth ¹⁰⁴⁴, D.J. Wilbern ¹⁰¹²⁴, H.G. Wilkens ¹⁰³⁷, J.J.H. Wilkinson ¹⁰³³, D.M. Williams ¹⁰⁴³, H.H. Williams ¹⁰¹³², S. Williams ¹⁰³³, S. Willocq ¹⁰¹⁰⁶, B.J. Wilson ¹⁰¹⁰⁴, P.J. Windischhofer ¹⁰⁴¹, F.I. Winkel ¹⁰³¹, F. Winklmeier ¹⁰¹²⁷, B.T. Winter ¹⁰⁵⁶, J.K. Winter ¹⁰¹⁰⁴, M. Wittgen ¹⁰¹⁴⁸, M. Wobisch ¹⁰¹⁰⁰, T. Wojtkowski ¹⁰⁶², Z. Wolffs ¹⁰¹¹⁸, J. Wollrath ¹⁰³⁷, M.W. Wolter ¹⁰⁸⁹, H. Wolters ^{10134a,134c}, M.C. Wong ¹⁰¹⁴⁰, E.L. Woodward ¹⁰⁴³, S.D. Worm ¹⁰⁵⁰, B.K. Wosiek ¹⁰⁸⁹, K.W. Woźniak ¹⁰⁸⁹, S. Wozniowski ¹⁰⁵⁷, K. Wraight ¹⁰⁶¹, C. Wu ¹⁰²¹, M. Wu ^{10115b}, M. Wu ¹⁰¹¹⁷, S.L. Wu ¹⁰¹⁷⁵, X. Wu ¹⁰⁵⁸, Y. Wu ^{1064a}, Z. Wu ¹⁰⁴, J. Wuerzinger ^{10113,ac}, T.R. Wyatt ¹⁰¹⁰⁴, B.M. Wynne ¹⁰⁵⁴, S. Xella ¹⁰⁴⁴, L. Xia ^{10115a}, M. Xia ¹⁰¹⁵, M. Xie ^{1064a}, S. Xin ^{1014,115c}, A. Xiong ¹⁰¹²⁷, J. Xiong ^{1018a}, D. Xu ¹⁰¹⁴, H. Xu ^{1064a}, L. Xu ^{1064a}, R. Xu ¹⁰¹³², T. Xu ¹⁰¹⁰⁹, Y. Xu ¹⁰¹⁴³, Z. Xu ¹⁰⁵⁴, Z. Xu ^{10115a}, B. Yabsley ¹⁰¹⁵², S. Yacoob ^{1034a}, Y. Yamaguchi ¹⁰⁸⁶, E. Yamashita ¹⁰¹⁵⁸, H. Yamauchi ¹⁰¹⁶¹, T. Yamazaki ^{1018a}, Y. Yamazaki ¹⁰⁸⁷, S. Yan ¹⁰⁶¹, Z. Yan ¹⁰¹⁰⁶, H.J. Yang ^{1064c,64d}, H.T. Yang ^{1064a}, S. Yang ^{1064a}, T. Yang ^{1066c}, X. Yang ¹⁰³⁷, X. Yang ¹⁰¹⁴, Y. Yang ¹⁰⁴⁶, Y. Yang ^{1064a}, Z. Yang ^{1064a}, W.-M. Yao ^{1018a}, H. Ye ^{10115a}, H. Ye ¹⁰⁵⁷, J. Ye ¹⁰¹⁴, S. Ye ¹⁰³⁰, X. Ye ^{1064a}, Y. Yeh ¹⁰⁹⁹, I. Yeletsikh ¹⁰⁴⁰, B. Yeo ^{1018b}, M.R. Yexley ¹⁰⁹⁹, T.P. Yildirim ¹⁰¹³⁰, P. Yin ¹⁰⁴³, K. Yorita ¹⁰¹⁷³, S. Younas ^{1028b}, C.J.S. Young ¹⁰³⁷, C. Young ¹⁰¹⁴⁸, C. Yu ^{1014,115c}, Y. Yu ^{1064a}, J. Yuan ^{1014,115c}, M. Yuan ¹⁰¹⁰⁹, R. Yuan ^{1064d,64c}, L. Yue ¹⁰⁹⁹, M. Zaazoua ^{1064a}, B. Zabinski ¹⁰⁸⁹, E. Zaid ¹⁰⁵⁴, Z.K. Zak ¹⁰⁸⁹, T. Zakareishvili ¹⁰¹⁶⁸, S. Zambito ¹⁰⁵⁸, J.A. Zamora Saa ^{10141d,141b}, J. Zang ¹⁰¹⁵⁸, D. Zanzi ¹⁰⁵⁶, O. Zaplatilek ¹⁰¹³⁶, C. Zeitnitz ¹⁰¹⁷⁶, H. Zeng ¹⁰¹⁴, J.C. Zeng ¹⁰¹⁶⁷, D.T. Zenger Jr ¹⁰²⁷, O. Zenin ¹⁰³⁹, T. Ženiš ^{1029a}, S. Zenz ¹⁰⁹⁷, S. Zerradi ^{1036a}, D. Zerwas ¹⁰⁶⁸, M. Zhai ^{1014,115c}, D.F. Zhang ¹⁰¹⁴⁴, J. Zhang ^{1064b}, J. Zhang ¹⁰⁶, K. Zhang ^{1014,115c}, L. Zhang ^{1064a}, L. Zhang ^{10115a}, P. Zhang ^{1014,115c}, R. Zhang ¹⁰¹⁷⁵, S. Zhang ¹⁰¹⁰⁹, S. Zhang ¹⁰⁹², T. Zhang ¹⁰¹⁵⁸, X. Zhang ^{1064c}, Y. Zhang ¹⁰¹⁴³, Y. Zhang ¹⁰⁹⁹, Y. Zhang ^{10115a}, Z. Zhang ^{1018a}, Z. Zhang ^{1064b}, Z. Zhang ¹⁰⁶⁸, H. Zhao ¹⁰¹⁴³, T. Zhao ^{1064b}, Y. Zhao ¹⁰¹⁴⁰, Z. Zhao ^{1064a}, Z. Zhao ^{1064a}, A. Zhemchugov ¹⁰⁴⁰, J. Zheng ^{10115a}, K. Zheng ¹⁰¹⁶⁷, X. Zheng ^{1064a}, Z. Zheng ¹⁰¹⁴⁸, D. Zhong ¹⁰¹⁶⁷, B. Zhou ¹⁰¹⁰⁹, H. Zhou ¹⁰⁷, N. Zhou ^{1064c}, Y. Zhou ¹⁰¹⁵, Y. Zhou ^{10115a}, Y. Zhou ¹⁰⁷, C.G. Zhu ^{1064b}, J. Zhu ¹⁰¹⁰⁹, X. Zhu ^{1064d}, Y. Zhu ^{1064c}, Y. Zhu ^{1064a}, X. Zhuang ¹⁰¹⁴, K. Zhukov ¹⁰⁷⁰, N.I. Zimine ¹⁰⁴⁰, J. Zinsser ^{1065b}, M. Ziolkowski ¹⁰¹⁴⁶, L. Živković ¹⁰¹⁶, A. Zoccoli ^{1024b,24a}, K. Zoch ¹⁰⁶³, T.G. Zorbas ¹⁰¹⁴⁴, O. Zormpa ¹⁰⁴⁸, W. Zou ¹⁰⁴³, L. Zwalinski ¹⁰³⁷.

¹Department of Physics, University of Adelaide, Adelaide; Australia.

²Department of Physics, University of Alberta, Edmonton AB; Canada.

^{3(a)}Department of Physics, Ankara University, Ankara; ^(b)Division of Physics, TOBB University of Economics and Technology, Ankara; Türkiye.

⁴LAPP, Université Savoie Mont Blanc, CNRS/IN2P3, Annecy; France.

⁵APC, Université Paris Cité, CNRS/IN2P3, Paris; France.

⁶High Energy Physics Division, Argonne National Laboratory, Argonne IL; United States of America.

⁷Department of Physics, University of Arizona, Tucson AZ; United States of America.

⁸Department of Physics, University of Texas at Arlington, Arlington TX; United States of America.

⁹Physics Department, National and Kapodistrian University of Athens, Athens; Greece.

¹⁰Physics Department, National Technical University of Athens, Zografou; Greece.

¹¹Department of Physics, University of Texas at Austin, Austin TX; United States of America.

¹²Institute of Physics, Azerbaijan Academy of Sciences, Baku; Azerbaijan.

¹³Institut de Física d'Altes Energies (IFAE), Barcelona Institute of Science and Technology, Barcelona;

Spain.

¹⁴Institute of High Energy Physics, Chinese Academy of Sciences, Beijing; China.

¹⁵Physics Department, Tsinghua University, Beijing; China.

¹⁶Institute of Physics, University of Belgrade, Belgrade; Serbia.

¹⁷Department for Physics and Technology, University of Bergen, Bergen; Norway.

^{18(a)}Physics Division, Lawrence Berkeley National Laboratory, Berkeley CA; ^(b)University of California, Berkeley CA; United States of America.

¹⁹Institut für Physik, Humboldt Universität zu Berlin, Berlin; Germany.

²⁰Albert Einstein Center for Fundamental Physics and Laboratory for High Energy Physics, University of Bern, Bern; Switzerland.

²¹School of Physics and Astronomy, University of Birmingham, Birmingham; United Kingdom.

^{22(a)}Department of Physics, Bogazici University, Istanbul; ^(b)Department of Physics Engineering, Gaziantep University, Gaziantep; ^(c)Department of Physics, Istanbul University, Istanbul; Türkiye.

^{23(a)}Facultad de Ciencias y Centro de Investigaciones, Universidad Antonio Nariño, Bogotá; ^(b)Departamento de Física, Universidad Nacional de Colombia, Bogotá; Colombia.

^{24(a)}Dipartimento di Fisica e Astronomia A. Righi, Università di Bologna, Bologna; ^(b)INFN Sezione di Bologna; Italy.

²⁵Physikalisches Institut, Universität Bonn, Bonn; Germany.

²⁶Department of Physics, Boston University, Boston MA; United States of America.

²⁷Department of Physics, Brandeis University, Waltham MA; United States of America.

^{28(a)}Transilvania University of Brasov, Brasov; ^(b)Horia Hulubei National Institute of Physics and Nuclear Engineering, Bucharest; ^(c)Department of Physics, Alexandru Ioan Cuza University of Iasi, Iasi; ^(d)National Institute for Research and Development of Isotopic and Molecular Technologies, Physics Department, Cluj-Napoca; ^(e)National University of Science and Technology Politehnica, Bucharest; ^(f)West University in Timisoara, Timisoara; ^(g)Faculty of Physics, University of Bucharest, Bucharest; Romania.

^{29(a)}Faculty of Mathematics, Physics and Informatics, Comenius University, Bratislava; ^(b)Department of Subnuclear Physics, Institute of Experimental Physics of the Slovak Academy of Sciences, Kosice; Slovak Republic.

³⁰Physics Department, Brookhaven National Laboratory, Upton NY; United States of America.

³¹Universidad de Buenos Aires, Facultad de Ciencias Exactas y Naturales, Departamento de Física, y CONICET, Instituto de Física de Buenos Aires (IFIBA), Buenos Aires; Argentina.

³²California State University, CA; United States of America.

³³Cavendish Laboratory, University of Cambridge, Cambridge; United Kingdom.

^{34(a)}Department of Physics, University of Cape Town, Cape Town; ^(b)iThemba Labs, Western Cape; ^(c)Department of Mechanical Engineering Science, University of Johannesburg, Johannesburg; ^(d)National Institute of Physics, University of the Philippines Diliman (Philippines); ^(e)University of South Africa, Department of Physics, Pretoria; ^(f)University of Zululand, KwaDlangezwa; ^(g)School of Physics, University of the Witwatersrand, Johannesburg; South Africa.

³⁵Department of Physics, Carleton University, Ottawa ON; Canada.

^{36(a)}Faculté des Sciences Ain Chock, Université Hassan II de Casablanca; ^(b)Faculté des Sciences, Université Ibn-Tofail, Kénitra; ^(c)Faculté des Sciences Semailia, Université Cadi Ayyad, LPHEA-Marrakech; ^(d)LPMR, Faculté des Sciences, Université Mohamed Premier, Oujda; ^(e)Faculté des sciences, Université Mohammed V, Rabat; ^(f)Institute of Applied Physics, Mohammed VI Polytechnic University, Ben Guerir; Morocco.

³⁷CERN, Geneva; Switzerland.

³⁸Affiliated with an institute formerly covered by a cooperation agreement with CERN.

³⁹Affiliated with an institute covered by a cooperation agreement with CERN.

- ⁴⁰Affiliated with an international laboratory covered by a cooperation agreement with CERN.
- ⁴¹Enrico Fermi Institute, University of Chicago, Chicago IL; United States of America.
- ⁴²LPC, Université Clermont Auvergne, CNRS/IN2P3, Clermont-Ferrand; France.
- ⁴³Nevis Laboratory, Columbia University, Irvington NY; United States of America.
- ⁴⁴Niels Bohr Institute, University of Copenhagen, Copenhagen; Denmark.
- ⁴⁵(^a)Dipartimento di Fisica, Università della Calabria, Rende;(^b)INFN Gruppo Collegato di Cosenza, Laboratori Nazionali di Frascati; Italy.
- ⁴⁶Physics Department, Southern Methodist University, Dallas TX; United States of America.
- ⁴⁷Physics Department, University of Texas at Dallas, Richardson TX; United States of America.
- ⁴⁸National Centre for Scientific Research "Demokritos", Agia Paraskevi; Greece.
- ⁴⁹(^a)Department of Physics, Stockholm University;(^b)Oskar Klein Centre, Stockholm; Sweden.
- ⁵⁰Deutsches Elektronen-Synchrotron DESY, Hamburg and Zeuthen; Germany.
- ⁵¹Fakultät Physik , Technische Universität Dortmund, Dortmund; Germany.
- ⁵²Institut für Kern- und Teilchenphysik, Technische Universität Dresden, Dresden; Germany.
- ⁵³Department of Physics, Duke University, Durham NC; United States of America.
- ⁵⁴SUPA - School of Physics and Astronomy, University of Edinburgh, Edinburgh; United Kingdom.
- ⁵⁵INFN e Laboratori Nazionali di Frascati, Frascati; Italy.
- ⁵⁶Physikalisches Institut, Albert-Ludwigs-Universität Freiburg, Freiburg; Germany.
- ⁵⁷II. Physikalisches Institut, Georg-August-Universität Göttingen, Göttingen; Germany.
- ⁵⁸Département de Physique Nucléaire et Corpusculaire, Université de Genève, Genève; Switzerland.
- ⁵⁹(^a)Dipartimento di Fisica, Università di Genova, Genova;(^b)INFN Sezione di Genova; Italy.
- ⁶⁰II. Physikalisches Institut, Justus-Liebig-Universität Giessen, Giessen; Germany.
- ⁶¹SUPA - School of Physics and Astronomy, University of Glasgow, Glasgow; United Kingdom.
- ⁶²LPSC, Université Grenoble Alpes, CNRS/IN2P3, Grenoble INP, Grenoble; France.
- ⁶³Laboratory for Particle Physics and Cosmology, Harvard University, Cambridge MA; United States of America.
- ⁶⁴(^a)Department of Modern Physics and State Key Laboratory of Particle Detection and Electronics, University of Science and Technology of China, Hefei;(^b)Institute of Frontier and Interdisciplinary Science and Key Laboratory of Particle Physics and Particle Irradiation (MOE), Shandong University, Qingdao;(^c)State Key Laboratory of Dark Matter Physics, School of Physics and Astronomy, Shanghai Jiao Tong University, Key Laboratory for Particle Astrophysics and Cosmology (MOE), SKLPPC, Shanghai;(^d)State Key Laboratory of Dark Matter Physics, Tsung-Dao Lee Institute, Shanghai Jiao Tong University, Shanghai;(^e)School of Physics, Zhengzhou University; China.
- ⁶⁵(^a)Kirchhoff-Institut für Physik, Ruprecht-Karls-Universität Heidelberg, Heidelberg;(^b)Physikalisches Institut, Ruprecht-Karls-Universität Heidelberg, Heidelberg; Germany.
- ⁶⁶(^a)Department of Physics, Chinese University of Hong Kong, Shatin, N.T., Hong Kong;(^b)Department of Physics, University of Hong Kong, Hong Kong;(^c)Department of Physics and Institute for Advanced Study, Hong Kong University of Science and Technology, Clear Water Bay, Kowloon, Hong Kong; China.
- ⁶⁷Department of Physics, National Tsing Hua University, Hsinchu; Taiwan.
- ⁶⁸IJCLab, Université Paris-Saclay, CNRS/IN2P3, 91405, Orsay; France.
- ⁶⁹Centro Nacional de Microelectrónica (IMB-CNM-CSIC), Barcelona; Spain.
- ⁷⁰Department of Physics, Indiana University, Bloomington IN; United States of America.
- ⁷¹(^a)INFN Gruppo Collegato di Udine, Sezione di Trieste, Udine;(^b)ICTP, Trieste;(^c)Dipartimento Politecnico di Ingegneria e Architettura, Università di Udine, Udine; Italy.
- ⁷²(^a)INFN Sezione di Lecce;(^b)Dipartimento di Matematica e Fisica, Università del Salento, Lecce; Italy.
- ⁷³(^a)INFN Sezione di Milano;(^b)Dipartimento di Fisica, Università di Milano, Milano; Italy.
- ⁷⁴(^a)INFN Sezione di Napoli;(^b)Dipartimento di Fisica, Università di Napoli, Napoli; Italy.

- 75^(a) INFN Sezione di Pavia;^(b) Dipartimento di Fisica, Università di Pavia, Pavia; Italy.
- 76^(a) INFN Sezione di Pisa;^(b) Dipartimento di Fisica E. Fermi, Università di Pisa, Pisa; Italy.
- 77^(a) INFN Sezione di Roma;^(b) Dipartimento di Fisica, Sapienza Università di Roma, Roma; Italy.
- 78^(a) INFN Sezione di Roma Tor Vergata;^(b) Dipartimento di Fisica, Università di Roma Tor Vergata, Roma; Italy.
- 79^(a) INFN Sezione di Roma Tre;^(b) Dipartimento di Matematica e Fisica, Università Roma Tre, Roma; Italy.
- 80^(a) INFN-TIFPA;^(b) Università degli Studi di Trento, Trento; Italy.
- 81 Universität Innsbruck, Department of Astro and Particle Physics, Innsbruck; Austria.
- 82 University of Iowa, Iowa City IA; United States of America.
- 83 Department of Physics and Astronomy, Iowa State University, Ames IA; United States of America.
- 84 İstinye University, Sarıyer, İstanbul; Türkiye.
- 85^(a) Departamento de Engenharia Elétrica, Universidade Federal de Juiz de Fora (UFJF), Juiz de Fora;^(b) Universidade Federal do Rio De Janeiro COPPE/EE/IF, Rio de Janeiro;^(c) Instituto de Física, Universidade de São Paulo, São Paulo;^(d) Rio de Janeiro State University, Rio de Janeiro;^(e) Federal University of Bahia, Bahia; Brazil.
- 86 KEK, High Energy Accelerator Research Organization, Tsukuba; Japan.
- 87 Graduate School of Science, Kobe University, Kobe; Japan.
- 88^(a) AGH University of Krakow, Faculty of Physics and Applied Computer Science, Krakow;^(b) Marian Smoluchowski Institute of Physics, Jagiellonian University, Krakow; Poland.
- 89 Institute of Nuclear Physics Polish Academy of Sciences, Krakow; Poland.
- 90 Faculty of Science, Kyoto University, Kyoto; Japan.
- 91 Research Center for Advanced Particle Physics and Department of Physics, Kyushu University, Fukuoka ; Japan.
- 92 L2IT, Université de Toulouse, CNRS/IN2P3, UPS, Toulouse; France.
- 93 Instituto de Física La Plata, Universidad Nacional de La Plata and CONICET, La Plata; Argentina.
- 94 Physics Department, Lancaster University, Lancaster; United Kingdom.
- 95 Oliver Lodge Laboratory, University of Liverpool, Liverpool; United Kingdom.
- 96 Department of Experimental Particle Physics, Jožef Stefan Institute and Department of Physics, University of Ljubljana, Ljubljana; Slovenia.
- 97 Department of Physics and Astronomy, Queen Mary University of London, London; United Kingdom.
- 98 Department of Physics, Royal Holloway University of London, Egham; United Kingdom.
- 99 Department of Physics and Astronomy, University College London, London; United Kingdom.
- 100 Louisiana Tech University, Ruston LA; United States of America.
- 101 Fysiska institutionen, Lunds universitet, Lund; Sweden.
- 102 Departamento de Física Teórica C-15 and CIAFF, Universidad Autónoma de Madrid, Madrid; Spain.
- 103 Institut für Physik, Universität Mainz, Mainz; Germany.
- 104 School of Physics and Astronomy, University of Manchester, Manchester; United Kingdom.
- 105 CPPM, Aix-Marseille Université, CNRS/IN2P3, Marseille; France.
- 106 Department of Physics, University of Massachusetts, Amherst MA; United States of America.
- 107 Department of Physics, McGill University, Montreal QC; Canada.
- 108 School of Physics, University of Melbourne, Victoria; Australia.
- 109 Department of Physics, University of Michigan, Ann Arbor MI; United States of America.
- 110 Department of Physics and Astronomy, Michigan State University, East Lansing MI; United States of America.
- 111 Group of Particle Physics, University of Montreal, Montreal QC; Canada.
- 112 Fakultät für Physik, Ludwig-Maximilians-Universität München, München; Germany.

- ¹¹³Max-Planck-Institut für Physik (Werner-Heisenberg-Institut), München; Germany.
- ¹¹⁴Graduate School of Science and Kobayashi-Maskawa Institute, Nagoya University, Nagoya; Japan.
- ¹¹⁵(^a) Department of Physics, Nanjing University, Nanjing; (^b) School of Science, Shenzhen Campus of Sun Yat-sen University; (^c) University of Chinese Academy of Science (UCAS), Beijing; China.
- ¹¹⁶Department of Physics and Astronomy, University of New Mexico, Albuquerque NM; United States of America.
- ¹¹⁷Institute for Mathematics, Astrophysics and Particle Physics, Radboud University/Nikhef, Nijmegen; Netherlands.
- ¹¹⁸Nikhef National Institute for Subatomic Physics and University of Amsterdam, Amsterdam; Netherlands.
- ¹¹⁹Department of Physics, Northern Illinois University, DeKalb IL; United States of America.
- ¹²⁰(^a) New York University Abu Dhabi, Abu Dhabi; (^b) United Arab Emirates University, Al Ain; United Arab Emirates.
- ¹²¹Department of Physics, New York University, New York NY; United States of America.
- ¹²²Ochanomizu University, Otsuka, Bunkyo-ku, Tokyo; Japan.
- ¹²³Ohio State University, Columbus OH; United States of America.
- ¹²⁴Homer L. Dodge Department of Physics and Astronomy, University of Oklahoma, Norman OK; United States of America.
- ¹²⁵Department of Physics, Oklahoma State University, Stillwater OK; United States of America.
- ¹²⁶Palacký University, Joint Laboratory of Optics, Olomouc; Czech Republic.
- ¹²⁷Institute for Fundamental Science, University of Oregon, Eugene, OR; United States of America.
- ¹²⁸Graduate School of Science, Osaka University, Osaka; Japan.
- ¹²⁹Department of Physics, University of Oslo, Oslo; Norway.
- ¹³⁰Department of Physics, Oxford University, Oxford; United Kingdom.
- ¹³¹LPNHE, Sorbonne Université, Université Paris Cité, CNRS/IN2P3, Paris; France.
- ¹³²Department of Physics, University of Pennsylvania, Philadelphia PA; United States of America.
- ¹³³Department of Physics and Astronomy, University of Pittsburgh, Pittsburgh PA; United States of America.
- ¹³⁴(^a) Laboratório de Instrumentação e Física Experimental de Partículas - LIP, Lisboa; (^b) Departamento de Física, Faculdade de Ciências, Universidade de Lisboa, Lisboa; (^c) Departamento de Física, Universidade de Coimbra, Coimbra; (^d) Centro de Física Nuclear da Universidade de Lisboa, Lisboa; (^e) Departamento de Física, Escola de Ciências, Universidade do Minho, Braga; (^f) Departamento de Física Teórica y del Cosmos, Universidad de Granada, Granada (Spain); (^g) Departamento de Física, Instituto Superior Técnico, Universidade de Lisboa, Lisboa; Portugal.
- ¹³⁵Institute of Physics of the Czech Academy of Sciences, Prague; Czech Republic.
- ¹³⁶Czech Technical University in Prague, Prague; Czech Republic.
- ¹³⁷Charles University, Faculty of Mathematics and Physics, Prague; Czech Republic.
- ¹³⁸Particle Physics Department, Rutherford Appleton Laboratory, Didcot; United Kingdom.
- ¹³⁹IRFU, CEA, Université Paris-Saclay, Gif-sur-Yvette; France.
- ¹⁴⁰Santa Cruz Institute for Particle Physics, University of California Santa Cruz, Santa Cruz CA; United States of America.
- ¹⁴¹(^a) Departamento de Física, Pontificia Universidad Católica de Chile, Santiago; (^b) Millennium Institute for Subatomic physics at high energy frontier (SAPHIR), Santiago; (^c) Instituto de Investigación Multidisciplinario en Ciencia y Tecnología, y Departamento de Física, Universidad de La Serena; (^d) Universidad Andres Bello, Department of Physics, Santiago; (^e) Instituto de Alta Investigación, Universidad de Tarapacá, Arica; (^f) Departamento de Física, Universidad Técnica Federico Santa María, Valparaíso; Chile.

- ¹⁴²Department of Physics, Institute of Science, Tokyo; Japan.
- ¹⁴³Department of Physics, University of Washington, Seattle WA; United States of America.
- ¹⁴⁴Department of Physics and Astronomy, University of Sheffield, Sheffield; United Kingdom.
- ¹⁴⁵Department of Physics, Shinshu University, Nagano; Japan.
- ¹⁴⁶Department Physik, Universität Siegen, Siegen; Germany.
- ¹⁴⁷Department of Physics, Simon Fraser University, Burnaby BC; Canada.
- ¹⁴⁸SLAC National Accelerator Laboratory, Stanford CA; United States of America.
- ¹⁴⁹Department of Physics, Royal Institute of Technology, Stockholm; Sweden.
- ¹⁵⁰Departments of Physics and Astronomy, Stony Brook University, Stony Brook NY; United States of America.
- ¹⁵¹Department of Physics and Astronomy, University of Sussex, Brighton; United Kingdom.
- ¹⁵²School of Physics, University of Sydney, Sydney; Australia.
- ¹⁵³Institute of Physics, Academia Sinica, Taipei; Taiwan.
- ¹⁵⁴(^a) E. Andronikashvili Institute of Physics, Iv. Javakhishvili Tbilisi State University, Tbilisi; (^b) High Energy Physics Institute, Tbilisi State University, Tbilisi; (^c) University of Georgia, Tbilisi; Georgia.
- ¹⁵⁵Department of Physics, Technion, Israel Institute of Technology, Haifa; Israel.
- ¹⁵⁶Raymond and Beverly Sackler School of Physics and Astronomy, Tel Aviv University, Tel Aviv; Israel.
- ¹⁵⁷Department of Physics, Aristotle University of Thessaloniki, Thessaloniki; Greece.
- ¹⁵⁸International Center for Elementary Particle Physics and Department of Physics, University of Tokyo, Tokyo; Japan.
- ¹⁵⁹Department of Physics, University of Toronto, Toronto ON; Canada.
- ¹⁶⁰(^a) TRIUMF, Vancouver BC; (^b) Department of Physics and Astronomy, York University, Toronto ON; Canada.
- ¹⁶¹Division of Physics and Tomonaga Center for the History of the Universe, Faculty of Pure and Applied Sciences, University of Tsukuba, Tsukuba; Japan.
- ¹⁶²Department of Physics and Astronomy, Tufts University, Medford MA; United States of America.
- ¹⁶³Department of Physics and Astronomy, University of California Irvine, Irvine CA; United States of America.
- ¹⁶⁴University of West Attica, Athens; Greece.
- ¹⁶⁵University of Sharjah, Sharjah; United Arab Emirates.
- ¹⁶⁶Department of Physics and Astronomy, University of Uppsala, Uppsala; Sweden.
- ¹⁶⁷Department of Physics, University of Illinois, Urbana IL; United States of America.
- ¹⁶⁸Instituto de Física Corpuscular (IFIC), Centro Mixto Universidad de Valencia - CSIC, Valencia; Spain.
- ¹⁶⁹Department of Physics, University of British Columbia, Vancouver BC; Canada.
- ¹⁷⁰Department of Physics and Astronomy, University of Victoria, Victoria BC; Canada.
- ¹⁷¹Fakultät für Physik und Astronomie, Julius-Maximilians-Universität Würzburg, Würzburg; Germany.
- ¹⁷²Department of Physics, University of Warwick, Coventry; United Kingdom.
- ¹⁷³Waseda University, Tokyo; Japan.
- ¹⁷⁴Department of Particle Physics and Astrophysics, Weizmann Institute of Science, Rehovot; Israel.
- ¹⁷⁵Department of Physics, University of Wisconsin, Madison WI; United States of America.
- ¹⁷⁶Fakultät für Mathematik und Naturwissenschaften, Fachgruppe Physik, Bergische Universität Wuppertal, Wuppertal; Germany.
- ¹⁷⁷Department of Physics, Yale University, New Haven CT; United States of America.
- ¹⁷⁸Yerevan Physics Institute, Yerevan; Armenia.
- ^a Also Affiliated with an institute covered by a cooperation agreement with CERN.
- ^b Also at An-Najah National University, Nablus; Palestine.
- ^c Also at Borough of Manhattan Community College, City University of New York, New York NY; United

States of America.

^d Also at Center for High Energy Physics, Peking University; China.

^e Also at Center for Interdisciplinary Research and Innovation (CIRI-AUTH), Thessaloniki; Greece.

^f Also at CERN, Geneva; Switzerland.

^g Also at CMD-AC UNEC Research Center, Azerbaijan State University of Economics (UNEC); Azerbaijan.

^h Also at Département de Physique Nucléaire et Corpusculaire, Université de Genève, Genève; Switzerland.

ⁱ Also at Departament de Física de la Universitat Autònoma de Barcelona, Barcelona; Spain.

^j Also at Department of Financial and Management Engineering, University of the Aegean, Chios; Greece.

^k Also at Department of Physics, California State University, Sacramento; United States of America.

^l Also at Department of Physics, King's College London, London; United Kingdom.

^m Also at Department of Physics, Stanford University, Stanford CA; United States of America.

ⁿ Also at Department of Physics, Stellenbosch University; South Africa.

^o Also at Department of Physics, University of Fribourg, Fribourg; Switzerland.

^p Also at Department of Physics, University of Thessaly; Greece.

^q Also at Department of Physics, Westmont College, Santa Barbara; United States of America.

^r Also at Faculty of Physics, Sofia University, 'St. Kliment Ohridski', Sofia; Bulgaria.

^s Also at Hellenic Open University, Patras; Greece.

^t Also at Imam Mohammad Ibn Saud Islamic University; Saudi Arabia.

^u Also at Institutio Catalana de Recerca i Estudis Avancats, ICREA, Barcelona; Spain.

^v Also at Institut für Experimentalphysik, Universität Hamburg, Hamburg; Germany.

^w Also at Institute for Nuclear Research and Nuclear Energy (INRNE) of the Bulgarian Academy of Sciences, Sofia; Bulgaria.

^x Also at Institute of Applied Physics, Mohammed VI Polytechnic University, Ben Guerir; Morocco.

^y Also at Institute of Particle Physics (IPP); Canada.

^z Also at Institute of Physics and Technology, Mongolian Academy of Sciences, Ulaanbaatar; Mongolia.

^{aa} Also at Institute of Physics, Azerbaijan Academy of Sciences, Baku; Azerbaijan.

^{ab} Also at National Institute of Physics, University of the Philippines Diliman (Philippines); Philippines.

^{ac} Also at Technical University of Munich, Munich; Germany.

^{ad} Also at The Collaborative Innovation Center of Quantum Matter (CICQM), Beijing; China.

^{ae} Also at TRIUMF, Vancouver BC; Canada.

^{af} Also at Università di Napoli Parthenope, Napoli; Italy.

^{ag} Also at University of Colorado Boulder, Department of Physics, Colorado; United States of America.

^{ah} Also at Washington College, Chestertown, MD; United States of America.

^{ai} Also at Yeditepe University, Physics Department, Istanbul; Türkiye.

* Deceased